POLITECNICO DI TORINO

Ph.D in Electronics and Telecommunications Engineering
XXVII Cycle

Ph.D Thesis

**The EGN Model of Nonlinear Propagation in Coherent
Optical Transmission Systems and Its Applications**

Supervisor:

Prof. Pierluigi Poggiolini

Candidate:

Yanchao Jiang

December 2014

Abstract

Modeling of nonlinear interference (NLI) generated by the fiber Kerr effect is a hot topic in coherent optical transmission systems. Four years ago, the Gaussian-noise (GN) model was proposed as an approximate tool for predicting the system maximum reach performance, in realistic optical coherent transmission scenarios, over lumped-amplification dispersion uncompensated links. For this specific use, the GN model has enjoyed substantial validation, both simulative and experimental.

The original GN model reference formula (GNRF) only described the simple second-order fiber dispersion. In this thesis, we first extend that formula to take the general dispersive propagation constant into account. We then make a comparison with the results of the GNRF over various types of fibers with quite different dispersions. It turns out that third-order dispersion has a very substantial effect on nonlinearity, especially near a fiber dispersion-zero.

It should be mentioned that the GN model may lose accuracy for fundamental reasons when approaching a dispersion zero. These can be overcome by the enhanced-GN (EGN) model, introduced below. On the other hand, the EGN model has two contributions, one of which is the GN model, so the extension of the GN model that was the first part of this thesis provides useful results for the EGN model too.

The GN model predictions, when used to obtain a detailed picture of NLI accumulation along a link rather than an estimate of the system maximum reach, may be affected by a substantial overestimation error, especially in the first few spans of the link. The error is larger for low-cardinality formats and systems with very short spans, or that use nearly-ideal distributed amplification. In this thesis, we analyze in detail the GN model errors. We discuss recently proposed formulas for correcting such errors and show that they neglect several contributions to NLI, so that they may substantially underestimate NLI in specific situations, especially over low-dispersion fibers. We derive a complete set of formulas accounting for all single-, cross-, and multi-channel effects. This set of formulas constitutes what we have called the EGN model. We extensively validate the EGN model by comparison with accurate simulations in several

different system scenarios. The overall EGN model accuracy is found to be very good when assessing detailed span-by-span NLI accumulation and excellent when estimating realistic system maximum reach. The computational complexity vs. accuracy trade-offs of the various versions of the GN and EGN models, and the presence and relevance of phase noise within NLI are discussed.

However, although the EGN model is theoretically rigorous, the complexity is substantially larger than that of the GN model, which makes its use difficult for real-time applications. Fortunately, we are able to derive a simple closed-form GN model correction formula based on the EGN model. The GN model, together with the correction formula, provides a low-complexity approximation to the EGN model. Such approximation has limitations, but already in its present form it effectively and rather accurately corrects for the GN model tendency to overestimate NLI, which is carefully validated over a wide range of system scenarios. The correction formula also allows to clearly identify the correction dependence on key system parameter, such as span length and loss.

As a reliable model, the EGN model is then employed to evaluate NLI generation in some study-cases:

1. Dispersion pre-compensation over mixed-fiber links: The dispersion pre-compensation impact both on homogeneous links (single fiber type) and inhomogeneous links (links using a mixture of high and low dispersion fibers) is analyzed. All results demonstrate that the EGN model is capable of dealing with the dispersion pre-compensation in mixed-fiber links.

2. Determining the optimum system symbol rate: The system symbol rate impact on NLI generation is studied in detail. The EGN model is found to be quite accurate in identifying the optimum symbol rate, as well as in predicting the related performance improvement. We also derived a simple closed-form formula that very reliably predicts the optimum symbol rate for quasi-Nyquist systems with lumped amplification.

3. NLI modeling for dynamically reconfigurable networks: the variability of NLI accumulation in dynamically reconfigurable networks with re-routing, different formats and accumulated dispersion is investigated. The EGN model can take the

propagation history of all channels into account, and correctly assess NLI generation with different link features.

Finally, an experiment is carried out to validate the EGN model for the first time. Using a PM-QPSK Nyquist WDM transmission, we confirm the enhanced accuracy of the EGN model comparing maximum reach predictions with those of the GN model.

Acknowledgement

When I registered for the Ph.D program in optical communication three years ago, I only took my interest and enthusiasm with me, but not a good major background. During the past three years, I obtained many helpful advises and supports from lots of colleagues and friends. Hereby I would like to express my deepest appreciation to them.

First and foremost, I would like to show my gratitude to all professors from OptCom Group in Politecnico di Torino: Prof. Pierluigi Poggiolini, Prof. Andrea Carena, Prof. Gabriella Bosco, Prof. Vittorio Curri and Prof. Roberto Gaudino. They are quite patient and responsible to bring me into the world of optical communication. Particularly, I owe a big debt of thanks to my supervisor, Prof. Poggiolini., a respectful and resourceful scholar. He provided me with valuable guidance and innovative ideas in every stage of my research. Without his impressive kindness and patience, I could not have done so much meaningful work and have completed this thesis.

Then, I would like to appreciate all researchers from ISMB, where I spent my first year. They are quite friendly and energetic to teach me many skills for experiment.

I also would like to thank Fabrizio Forghieri from CISCO, who gave me much useful suggestion for my research.

I would like to extend my appreciation to China Scholarship Council (CSC), which provided me the opportunity to study abroad and funded me in the past three years.

Last but not least, I would like to thank all my friends who care me and help me both here and home, all my families who love me and support me, and especially my dear husband, who takes care of me everywhere and all the time.

Contents

Chapter 1 Introduction

1.1 Background and motivation

The research in optical transmission systems started in earnest in the 1970s, based essentially on the intensity modulation direct detection (IMDD) scheme. It is a simple on-off power modulation, where the receiver is insensitive to either the carrier phase or the state of polarization.

In the 1980s, coherent optical transmission systems were studied. However, their development was interrupted for nearly 20 years due to the fast progress in IMDD optical systems, and especially the invention of optical amplifiers [1].

In the 1990s, wavelength division multiplexing (WDM), similar to frequency division multiplexing (FDM) of radio systems, was developed, enabling transmission of more than one channel per fiber. As shown in Fig. 1-1, multiple channels are allocated on the same fiber, on separate frequency bands.
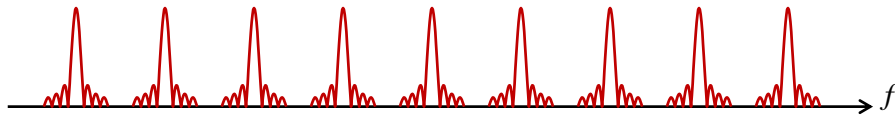
Fig. 1-1: One WDM system with 9 channels.

After 2005, the advent of digital signal processing (DSP) brought coherent optical transmission systems back to meet the ever-increasing bandwidth demand. DSP made it possible to perform carrier phase and polarization recovery and tracking. It also permitted electronic fiber chromatic dispersion (CD) compensation, so that optical dispersion management (DM) could be avoided, thus allowing the exploitation of the so-called "uncompensated" transmission (UT) technique.

1.1.1 Coherent optical transmission systems

In a modern coherent optical transmission system, as shown in Fig. 1-2, the signal is propagating from transmitter (Tx) to receiver (Rx), passing through many spans of optical fiber. At the end of each span, an erbium-doped fiber amplifier (EDFA) is employed to recover the loss of the fiber. At the same time, the EDFA produces

amplified spontaneous emission (ASE) noise. The coherent receiver is sensitive to the phase and polarization of the incoming signal, therefore we can encode information both on the in-phase and quadrature components and on the two orthogonal polarizations. In-line optical dispersion compensation is not present.
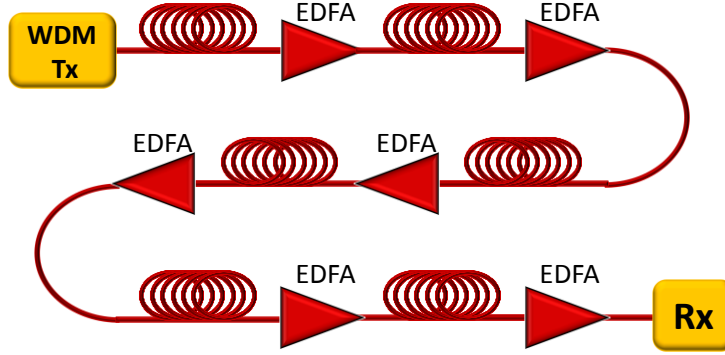
Fig. 1-2: The coherent optical transmission systems.

The system performance in coherent optical transmission systems is mainly limited by ASE noise and the nonlinear interference (NLI) disturbance generated by the fiber Kerr effect. In order to assess the system performance, the optical signal-to-noise ratio (OSNR) is widely used. In the linear regime, OSNR is defined as,

$$\text{OSNR}_{\text{ASE}} = \frac{P_{\text{ch}}}{P_{\text{ASE}}} \tag{1-1}$$

where P_{ch} is the signal power in each channel, P_{ASE} is the power of ASE noise. Since ASE noise is accumulated span by span, we have to increase the power per channel to reach a longer distance, as shown by the green solid line in Fig. 1-3.

In the nonlinear regime, OSNR is defined as,

$$\text{OSNR}_{\text{NLI}} = \frac{P_{\text{ch}}}{P_{\text{NLI}}} \tag{1-2}$$

where P_{NLI} is the power of NLI noise. This formula assumes that NLI can be dealt with as additive Gaussian noise. This is the case in most optical coherent transmission systems. We will discuss this assumption in Sect. 3.3.2.

Contrary to the case of ASE noise, we have to decrease the power per channel to get to longer distances, as shown by the red solid line in Fig. 1-3. At a certain distance, the red and green lines meet, and the cross-point provides a rough estimate of the system

maximum reach and optimal power.

To obtain a better estimate, one has to actually consider both sources of disturbance together. When putting both ASE and NLI noise together, OSNR is expressed as,

$$\text{OSNR} = \frac{P_{\text{ch}}}{P_{\text{ASE}} + P_{\text{NLI}}} \tag{1-3}$$

and the system behavior is shown as the blue solid curve in Fig. 1-3, which indicates that the realistic system maximum reach is somewhat shorter than the cross-point.
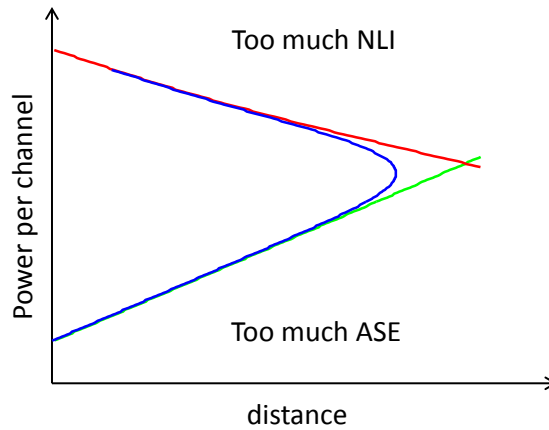
Fig. 1-3: Contour plot of the points characterized by a given fixed OSNR at the end of the link. The plane co-ordinates are launch power per channel and distance. The green solid line assumes Eq. (1-1) and considers ASE noise only; the red solid line assumes Eq. (1-2) and considers NLI noise only; the blue solid line assumes Eq. (1-3) and considers both ASE and NLI noise.

In Fig. 1-3, there is too much ASE noise in the lower region, under the green solid line. It can be reduced using special amplifiers (such as Raman) or low-loss fibers, but it cannot be eliminated. In the upper region, above the red solid line, there is too much NLI, which can be reduced using for instance new fibers with low nonlinearity coefficient. However, fundamental limits are being reached in fiber development as well. So, even considering recent and foreseeable progress, optical systems will always conceivably be limited by a combination of ASE and NLI noise, similar to what is shown in Fig. 1-3. The problem of system analysis and design is then strictly related to that of characterizing P_{ASE} and P_{NLI} in Eq. (1-3).

1.1.2 Characterizing ASE and NLI

ASE noise accumulation has been well understood for a long time. Assuming lumped

amplification through an EDFA, its power spectral density (PSD), after N_s identical spans, is expressed as,

$$G_{\mathrm{ASE}} = N_s \frac{hf}{2}(G-1)n_{\mathrm{sp}} \qquad (1\text{-}4)$$

where h is the Planck's constant, $h = 6.62559 \times 10^{-34}$ J·s. f is optical frequency. G is the gain of the EDFA at the end of each span, assumed to fully compensate for the span loss. n_{sp} is the spontaneous emission factor and is always greater than 1. Then the power of the ASE noise can be calculated through an integration of its PSD over a given bandwidth,

$$P_{\mathrm{ASE}} = \int_{f \in B_{\mathrm{OSNR}}} G_{\mathrm{ASE}} df \qquad (1\text{-}5)$$

where B_{OSNR} is the bandwidth for calculating OSNR.

As for NLI, a similar formula to Eq. (1-5) can be tentatively written as:

$$P_{\mathrm{NLI}} = \int_{f \in B_{\mathrm{OSNR}}} G_{\mathrm{NLI}}(f) df \qquad (1\text{-}6)$$

We will discuss later such formula in more detail and provide a more rigorous definition and derivation. However, the point that we want to make is that the key quantity that needs to be characterized, as far as NLI is concerned, is its PSD $G_{\mathrm{NLI}}(f)$. To derive $G_{\mathrm{NLI}}(f)$, an analytical fiber nonlinear propagation model is needed.

Many approximate fiber nonlinear propagation models have been proposed and studied over the years, addressing very different link and system scenarios as technology evolved. In the next section we provide a brief overview of some of such models.

1.1.3 An overview of some perturbative models

1.1.3.1 Most common modeling assumptions

The majority of nonlinear propagation models make the assumption that nonlinearity is relatively small, i.e., that it is a perturbation as compared to the useful signal. Thanks to this assumption, model derivation can exploit perturbation techniques, which allow to find approximate analytical solutions to the nonlinear Schrödinger equation (NLSE) or the Manakov equation (ME) [2-4]. Clearly, the perturbation assumption breaks down at highly nonlinear regimes. However, both simulations and experiments have shown it to

be sufficiently well verified within the range of optimal system launch powers. All models mentioned in the following are perturbation analysis models, although the specific perturbation technique may differ.

A second possible assumption is that the transmitted signal statistically behaves as stationary Gaussian noise. We call this the "signal-Gaussianity" assumption. This assumption is certainly not verified at the Tx output. However, it can be argued that, as the signal propagates along a UT link and gets thoroughly dispersed, it tends to take on an approximately Gaussian-like distribution. Recently, it has been shown that this is true for the first-order distribution of the signal. However, multiple time-samples of the transmitted signal do not readily take on a joint-Gaussian distribution [30]. Nonetheless, the signal Gaussianity assumption is often a reasonably viable one, producing acceptably accurate results. It is at the basis of the Gaussian-noise (GN) model. The enhanced GN model (or EGN model, see below), the main focus of this thesis, overcomes it.

Another common assumption is that the signal disturbance generated by NLI, manifests itself as additive circular Gaussian noise (AGN). This assumption too is just an approximation. Under certain special conditions, and especially over idealized single-polarization lossless fibers, a substantial phase-noise component may develop, so that the NLI "circularity" is notably lost. Also, such phase noise may present a prolonged internal correlation (tens to hundreds of symbols) [27]. On the other hand, in typical systems, the AGN assumption for NLI has been repeatedly shown to work well. Phase noise will be discussed in Sect. 3.3.2. The GN and EGN models use this assumption as well.

Another assumption is that only certain NLI components are prevalent. The most popular of this class of assumptions is that of retaining only the "cross phase modulation" (XPM) component of inter-channel nonlinearity, while neglecting all other components. Depending on system parameters, this assumption may or may not produce reliable results.

These assumptions, and yet others, are just tentative approximations that have been used to derive models that typically do not aim at being exact solutions of the nonlinear propagation problem. They generally aim at being practical tools, sufficiently accurate to be used for system analysis and design.

1.1.3.2   A few model examples

The earliest model that we mention dates back to 1993 [5]. It was based on directly postulating that all nonlinearity was produced by four-wave mixing (FWM) acting among the overall WDM signal spectral components, assumed "incoherent". Remarkably, though limited to single-polarization and to a rectangular overall WDM spectrum, the results of this early effort essentially agree with those obtained through the GN model under such limitations. In 2003, [6] showed that, based on a perturbation approach outlined in [7], similar results to those found in [5] could be re-derived.

A 1997 paper [8] found an approximate solution to the NLSE in terms of a truncated Volterra series (VS) in frequency-domain. These results were later used (in 2002) to derive a PSD of NLI [9] and to discuss fiber capacity in [10], in a single-polarization scenario. The found model equations are very similar to the GN model for single-polarization.

More recently, another approach was proposed, based on ideally slicing up the signal spectrum into discrete spectral components, whose nonlinear beating during propagation is then analytically assessed. We call it the spectral slicing (SpS) approach. Spectral slicing is naturally found in orthogonal FDM (OFDM) systems, so SpS was first used to model nonlinearity limited to these systems (2008-2011) [11-13]. These papers obtained what could be viewed as a specialized version of the GN model for OFDM. The SpS approach was also taken up aiming at general WDM systems (including OFDM as a special case). In this approach, spectral slicing is introduced early in the derivation but then it is removed through a suitable transition to continuous spectra. This effort (2011 to now [14-17]) led to the first appearance of the GN model in its current form. The GN model is the starting point for the modeling effort dealt with in this thesis.

Two further papers, devoted specifically to detailed re-derivations of the GN model, were also recently published (2011-2013) [18, 19]. Both independently confirm the GN model main equations and provide further generalizations. Specifically, [18] is based on a modified version of the first-order regular-perturbation method (RP1), which had been shown in [20] to be equivalent to the VS method. Paper [19] uses a variation on the SpS approach.

An interesting question is why the earlier instances of these models did not enjoy

widespread attention when originally published many years ago. The answer appears to be that they did not work well for the DM systems of the time. Specifically, it appears that both the signal-Gaussianity and, to some extent, the NLI circular-Gaussianity assumptions, do not hold up well, or not at all, in DM systems where, contrary to UT, dispersion is not allowed to accumulate.

A separate class of proposed models employs a time-domain (TD) perturbation approach, which was introduced in 2000 [21, 22]. In 2012, this approach was substantially re-visited and extended [23]. The interesting feature of the TD models is that they do not need to rely on the signal-Gaussianity assumption, ideally making it possible for them to overcome the GN model limitations induced by it. However, without the signal Gaussianity assumption, rather complex equations are found. In order to achieve simpler results, further assumptions and approximations are typically necessary. For instance, the XPM approximation is typically invoked for inter-channel nonlinear effects [30-32].

In the recent past, various other models have been proposed. These include a mixed time-and-frequency domain approach, for systems dominated by intra-channel FWM [24] and a discrete-time single-channel model based on deriving analytical results from the split-step algorithm [25]. Another proposal makes use of a more conventional perturbative approach: however, instead of seeking a result in terms of an additive NLI disturbance, it looks at phase disturbance, akin to self- and cross-phase modulation [26]. This modeling approach has been further developed into [27]. These models too use the XPM approximation.

Neither the GN, nor its follow-up model (the EGN model), use the XPM approximation.

1.2 Current developments on nonlinear propagation modeling

The GN model permits to readily estimate the PSD of NLI $G_{\mathrm{NLI}}(f)$ which in turn delivers P_{NLI} through Eq. (1-6). It is then possible to compute the nonlinear OSNR of Eq. (1-3) and hence predict system performance, such as its maximum reach. For this use, the GN model has been subjected to rather extensive validation. Most of the validation effort focused on lumped-amplification systems with relatively long spans (terrestrial-

type, 80-120 km) and non-zero fiber dispersion (D>3.5 ps/nm/km). In this context, the predictive power of the GN model has been found to be rather good [15, 17]

Recently, however, it has been pointed out that when the GN model is used to look at the detailed span-by-span characterization of NLI accumulation along a link, its predictions may be affected by a substantial error [28-33]. In particular [28], the first peer-reviewed published paper on the subject (simultaneously with [29]), presented for the first time a detailed picture of the predicted and actual NLI noise variance accumulated along realistic links based on PM-QPSK (polarization-multiplexed quadrature phase shift keying) and PM-16QAM (polarization-multiplexed 16 quadrature amplitude modulation). The paper showed that the GN model overestimates the variance of NLI, most notably in the first spans of the link, where this error may amount to several dB's, depending on system parameters and modulation format. The error then abates considerably along the link, but it does not vanish. This error is related to the "signal Gaussianity" assumption. Especially in the first spans of the link, this approximation is far away accurate and generates substantial error.

Independently of [28], another paper [30] later focused on the issue of the GN model accuracy. Remarkably, [30] succeeded in analytically removing the signal Gaussianity assumption. A "correction term" to the GN model, limited to XPM, was found. The results of [30] constitute major progress, also because it was shown that removing the signal Gaussianity assumption does not lead to unmanageably complex calculations, as previously believed.

In chapter 3, we adopt a similar approach to that indicated in [30] to provide a complete model, which includes correction terms for all NLI components, including single-channel and all inter-channel. We called this new model "enhanced GN model", or EGN model, and constitutes the main topic dealt with in this thesis.

1.3 Thesis contents and my contributions

In this thesis, in chapter 2 I first extended the GN reference formula (GNRF) so that it can take into account any fiber dispersion profile. I followed the same procedure as for deriving the GN model, but with the replacement of the simple second-order dispersion parameter β_2 used in the GNRF by a generic $\beta(f)$. After obtaining the general formula

with $\beta(f)$, I substituted β_2 and β_3 into it to get an explicit formula as a function of such parameters. Then I made a comparison of the new formula (including β_2 and β_3) with the old GNRF (that had β_2 only) over various types of fibers with quite different dispersions, including very low values. It should be said that the GN model may not be accurate at very low dispersion. However, it is one of the contributions that make up the EGN model, whose validity may extend closer to zero-dispersion. So this first part of my work carries on to the GN model and is useful in that context too.

I then worked on the derivation of the EGN model, which is performed by extending the approach addressed in [30] to remove the signal Gaussianity approximation completely. This effort is reported in chapter 3. In detail, I worked on the derivation of the GN model "correction terms" for single-channel interference (SCI). I then focused on the formulas for the NLI noise due to cross-channel interference (XCI). In chapter 3, they are shown to contain more contributions than accounted for in the XPM formulas of [30]. I also discussed the impact of multi-channel interference, which was neglected in [30], and provided the formulas needed to account for MCI as well. Overall, I worked on the derivation of a complete set of equations that fully correct the GN model for the effect of signal non-Gaussianity. In chapter 3, I show a careful comparison of the EGN model predictions, for which I implemented the numerical integration code, with accurate simulations of span-by-span NLI accumulation (carried out by other OptCom Group members), and show the EGN model accuracy to be very good. The results also show that the XPM formulas proposed in [30] may in certain cases substantially underestimate NLI, especially over low-dispersion fibers and for narrow channel spacing. I applied the EGN model to various realistic system scenarios involving PM-QPSK and PM-16QAM. Specifically, I concentrated on a comparison of the estimate of system maximum reach obtained using either the GN model or the EGN model, vs. accurate simulation results (simulations performed by other OptCom Group members). The bottom-line findings are that, the GN model always underestimates the system maximum reach, by 5% to 20% depending on system parameters, while the EGN model provides much better accuracy, completely removing the underestimation incurred by the GN model. The resulting complexity of the EGN model is however rather large and I discuss the issue of computational effort for realistic system performance prediction. I

also discuss the presence and relevance of phase noise within NLI. The results indicate that, in the context of realistic PM-QPSK systems, phase noise appears to have small or negligible impact on system performance prediction. In other words, the assumption of NLI noise being circular, Gaussian and additive appears to be adequate for system performance predictions in most practical system scenarios.

In chapter 4, a compact closed-form correction to the GN model is presented. It can be viewed as a simple approximation to the EGN model from which it is derived. I carefully validated the low-complexity EGN model approximation over a wide range of system scenarios. It turns out that in its present form it effectively and rather accurately corrects for the GN model bias towards NLI overestimation. Additionally, I tested it in estimating the system maximum reach for the same system scenarios in chapter 3, vs. the GN model and simulations. This EGN model approximation is quite effective, especially for low frequency spacing. I finally discuss the main parameter dependencies of the closed-form correction.

In chapter 5, I investigated the application of the EGN model for evaluating NLI generation in three study-cases:

1. Dispersion pre-compensation over mixed-fiber links: I first analyzed homogeneous links (single fiber type). By modifying the function that describes the link features in the EGN model equations (the "link function"), I took chromatic dispersion pre-compensation (CDP) into the EGN model. I then calculated NLI generation of a link, with or without CDP using the EGN model. I compared the results with simulation (performed by other OptCom Group members). I then moved to inhomogeneous links, i.e., links using a mixture of high and low dispersion fibers. I derived a suitable link function to be used in the EGN model to analyze NLI accumulation along such mixed-fiber links. I carried out a performance comparison of the case with or without CDP. All results show that the EGN model is in good agreement with the simulations, and the EGN model is capable of dealing with CDP in mixed-fiber links.

2. Determining the optimum system symbol rate: This case-study focused on the following scenario: the total WDM bandwidth, spectral efficiency, spectrum roll-off and modulation format of a system are pre-determined, the only free parameter

is the number of channels that the overall WDM bandwidth is split into or, equivalently, the symbol rate per channel. I evaluated the NLI generation as a function of such symbol rate per channel, for several system scenarios. I used the GN, EGN, EGN approximation and XPM models, vs. simulations (performed by other OptCom Group members). The EGN model is the only one among these four models which can identify the optimum symbol rate and estimate the system performance accurately. I then verified that a simple closed-form formula (derived by other OptCom Group members) can predict the optimum symbol rate in quasi-Nyquist systems quite accurately, over a wide range of dispersions and span numbers.

3. NLI modeling for dynamically reconfigurable networks (DRNs): I employed the EGN model to assess a set of possible scenarios which can be representative of DRNs with re-routing. Channels can have different modulation formats and accumulated dispersion, and can change their neighbors repeatedly along their lightpath. I show that depending on the complex possible propagation histories of CUT and INTs, a "spread" of NLI results is generated, ranging between clearly identifiable approximate upper and lower bounds. I discuss the use of the very simple incoherent GN model in this context.

Chapter 6 reports on an experiment which was carried out to specifically validate the EGN model. The difference between the GN and EGN models is quite small when estimating the system maximum reach in typical long-haul transmission scenarios. Therefore, the link had to be specifically designed to produce a substantial prediction difference between these two models. This was done in order to be able to reliably distinguish between the two predictions even in the presence of measurement uncertainties. In the experiment, a very short span length (25 km) of ultra-low loss SMF was chosen. The CUT was PM-QPSK, while the INTs were all either PM-QPSK or Gaussian-constellation modulated. The results show that the EGN model and the experiments match well.

Finally, chapter 7 draws a conclusion.

Many of the above research results were obtained through team work, within the OptCom Group. My main contributions were:

1. Generalizing the GN model by taking a generic dispersion profile $\beta(f)$ into account, and making a comparison with the previous GNRF;

2. Deriving all formulas for self-, cross- and multi-channel interference, which constitute the EGN model. Moreover, I prepared an efficient numerical integration code for calculating the EGN model. When validating its accuracy, I prepared all curves related to the GN, EGN and XPM models;

3. Deriving all numerical results for testing the closed-form correction to the GN model;

4. Modifying the EGN model to apply it for dealing with dispersion conditions, mixed-fiber links, system symbol rates, and so on;

5. Regarding the experiment, I helped in the link design and performed the numerical calculations using the EGN model. I also carried out the comparison between the experimental results and the EGN model predictions and helped in the general conduction of the investigation.

Chapter 2   The inclusion of the dispersion profile into the GN model

The original GN model reference formula (GNRF) only included the simple second-order fiber dispersion. In this chapter, we extend that formula to take the general dispersive propagation constant into account.

2.1 The GN model with dispersion derivative

2.1.1 Analytical derivation for a single-polarization system

2.1.1.1 The signal model

The signal model is one of the key aspects enabling the derivation of the GN model. An overall WDM signal model should satisfy the following constraints:

- a zero-mean complex Gaussian random process with uncorrelated phase and quadrature components;
- periodic of period T_0, where T_0 is an integer multiple of the symbol duration T_s;
- its average PSD is shaped according to that of an actual WDM signal.

Therefore, the wanted signal model in frequency-domain is:

$$E(0,f) = E(f) = \sqrt{f_0 G_{\mathrm{Tx}}(f)} \sum_{n=-\infty}^{+\infty} \xi_n \delta(f - nf_0) \qquad (2\text{-}1)$$

where $G_{\mathrm{Tx}}(f)$ is the average PSD of the signal, ξ_n's are complex Gaussian random variables (RVs) of unit variance, independent of one another. Actually, this is an approximation. Physically speaking, ξ_n's are uncorrelated, and there is correlation between those spectral lines that are multiples of the symbol rate apart. More details can be found in [15, 16].

2.1.1.2 The NLSE

The NLSE is the fundamental equation of single-polarization fiber nonlinear dispersive propagation. It is well known that the NLSE in the frequency-domain is reduced to an ordinary differential equation rather than a partial differential equation.

Therefore, we chose to work in the frequency-domain. Taking the general propagation constant $\beta(f)$, which varies as a function of frequency, into account, the NLSE can be written as:

$$\frac{\partial}{\partial z}E(z,f)=-j\beta(f)E(z,f)-\alpha E(z,f)-j\gamma E(z,f)*E^*(z,-f)*E(z,f) \quad (2\text{-}2)$$

where $E(z,f)$ is the propagating signal, α is the optical field fiber loss, γ is the fiber nonlinearity coefficient, the last term is due to the Kerr effect in the fiber, the symbol "$*$" stands for "convolution product".

First, the nature of the Kerr term at the fiber input, that is at $z=0$, is investigated:

$$\begin{aligned}Q_{\mathrm{NLI}}(0,f)&=-j\gamma E(0,f)*E^*(0,-f)*E(0,f)\\ &=-j\gamma\int\limits_{-\infty}^{\infty}\int\limits_{-\infty}^{\infty}E(0,f_1)E^*(0,f_1-f_2)E(0,f-f_2)df_1df_2\end{aligned} \quad (2\text{-}3)$$

We then substitute Eq. (2-1) into Eq. (2-3):

$$\begin{aligned}Q_{\mathrm{NLI}}(0,f)&=-j\gamma f_0^{\frac{3}{2}}\sum_{m=-\infty}^{\infty}\sum_{n=-\infty}^{\infty}\sum_{k=-\infty}^{\infty}\xi_m\xi_n^*\xi_k\\ &\quad \int\limits_{-\infty}^{\infty}\int\limits_{-\infty}^{\infty}\sqrt{G_{\mathrm{Tx}}(f_1)G_{\mathrm{Tx}}(f_1-f_2)G_{\mathrm{Tx}}(f-f_2)}\\ &\quad \delta(f_1-mf_0)\delta(f_1-f_2-nf_0)\delta(f-f_2-kf_0)df_2df_1\\ &=-j\gamma f_0^{\frac{3}{2}}\sum_{m=-\infty}^{\infty}\sum_{n=-\infty}^{\infty}\sum_{k=-\infty}^{\infty}\xi_m\xi_n^*\xi_k\\ &\quad \sqrt{G_{\mathrm{Tx}}(mf_0)G_{\mathrm{Tx}}(nf_0)G_{\mathrm{Tx}}(kf_0)}\delta\big(f-[m-n+k]f_0\big)\\ &=-j\gamma f_0^{\frac{3}{2}}\sum_{i=-\infty}^{\infty}\delta(f-if_0)\cdot\\ &\quad \sum_{m,n,k\in A_i}\xi_m\xi_n^*\xi_k\sqrt{G_{\mathrm{Tx}}(mf_0)G_{\mathrm{Tx}}(nf_0)G_{\mathrm{Tx}}(kf_0)}\end{aligned} \quad (2\text{-}4)$$

where A_i is the set of all triples (m,n,k) such that $m-n+k=i$, that is:

$$A_i\equiv\big\{(m,n,k):m-n+k=i\big\} \quad (2\text{-}5)$$

Among all the possible triples (m,n,k) in A_i we identify a subset X_i for which $[m=n \text{ or } k=n]$, that is:

$$X_i\equiv\big\{(m,n,k):[m-n+k=i]\text{ and }[m=n\text{ or }k=n]\big\} \quad (2\text{-}6)$$

We then define the coset $\tilde{A}_i$ as:

$$\tilde{A}_i = A_i - X_i \tag{2-7}$$

We can consequently decompose $Q_{NLI}(0,f)$ into two separate contributions:

$$Q_{NLI}(0,f) = Q_{NLI,\tilde{A}_i}(0,f) + Q_{NLI,X_i}(0,f) \tag{2-8}$$

where,

$$Q_{NLI,\tilde{A}_i}(0,f) = -j\gamma f_0^{\frac{3}{2}} \sum_{i=-\infty}^{\infty} \delta(f-if_0)\cdot \sum_{m,n,k\in\tilde{A}_i} \xi_m\xi_n^*\xi_k \sqrt{G_{Tx}(mf_0)G_{Tx}(nf_0)G_{Tx}(kf_0)} \tag{2-9}$$

$$Q_{NLI,X_i}(0,f) = -j\gamma f_0^{\frac{3}{2}} \sum_{i=-\infty}^{\infty} \delta(f-if_0)\cdot \sum_{m,n,k\in X_i} \xi_m\xi_n^*\xi_k \sqrt{G_{Tx}(mf_0)G_{Tx}(nf_0)G_{Tx}(kf_0)} \tag{2-10}$$

By using Eq. (2-6) we can rewrite $Q_{NLI,X_i}(0,f)$, finding:

$$\begin{aligned} Q_{NLI,X_i}(0,f) &= -j2\gamma f_0^{\frac{3}{2}} \sum_{i=-\infty}^{\infty} \delta(f-if_0)\sqrt{G_{Tx}(if_0)}\,\xi_i \cdot \sum_n G_{Tx}(nf_0)|\xi_n|^2 \\ &= -j2\gamma\sqrt{f_0}P_{Tx} \sum_{i=-\infty}^{\infty} \sqrt{G_{Tx}(if_0)}\,\xi_i\delta(f-if_0) \\ &= -j2\gamma P_{Tx}E(0,f) \end{aligned} \tag{2-11}$$

This result shows that the effect of $Q_{NLI,X_i}(0,f)$ on the NLSE is that of adding a constant-coefficient multiplying the unknown $E(0,f)$. At a generic distance $z>0$, it remains very similar to Eq. (2-11), namely:

$$Q_{NLI,X_i}(z,f) = -j2\gamma P_{Tx}e^{-2\alpha z}\cdot E(z,f) \tag{2-12}$$

As commented in [16], they only give rise to a frequency-independent phase-shift which turns out to be completely irrelevant to the final PSD of NLI. Consequently, we can neglect this term. Throughout this thesis, this term is not considered.

Therefore, the NLSE at any distance z can be rewritten as:

$$\frac{\partial}{\partial z}E(z,f) = \left[-j\beta(f)-\alpha\right]E(z,f) + Q_{NLI,\tilde{A}_i}(z,f) \tag{2-13}$$

We now introduce a fundamental assumption on which the model is based: we assume that the Kerr term $Q_{NLI,\tilde{A}_i}(z,f)$ acts as a pure source term in Eq. (2-13), i.e., it acts as if it

was independent of the equation unknown $E(z,f)$. If so, according to standard results, a fully analytical solution to Eq. (2-13) can be written as:

$$E(z,f) = e^{\Gamma(z,f)} \cdot \int_0^z e^{-\Gamma(z',f)} Q_{\mathrm{NLI},\tilde{A}_i}(z',f) \, dz' + e^{\Gamma(z,f)} E(0,f) \tag{2-14}$$

where:

$$\Gamma(z,f) = \int_0^z \left[-j\beta(f) - \alpha \right] d\zeta = -j\beta(f)z - \alpha z \tag{2-15}$$

From Eq. (2-14), we can write:

$$E(z,f) \approx E_{\mathrm{LIN}}(z,f) + E_{\mathrm{NLI}}(z,f) \tag{2-16}$$

where:

$$E_{\mathrm{LIN}}(z,f) = e^{\Gamma(z,f)} E(0,f) \tag{2-17}$$

is the "linear" solution, i.e., what one gets in the absence of nonlinearity, and:

$$E_{\mathrm{NLI}}(z,f) = e^{\Gamma(z,f)} \cdot \int_0^z e^{-\Gamma(z',f)} Q_{\mathrm{NLI},\tilde{A}_i}(z',f) \, dz' \tag{2-18}$$

is the NLI. Finding the PSD of $E_{\mathrm{NLI}}(z,f)$ is the main goal and therefore Eq. (2-18) is a key result. The assumption of the independence of $Q_{\mathrm{NLI},\tilde{A}_i}(z,f)$ on $E(z,f)$, which makes it possible to write Eq. (2-18), is clearly an approximation.

Moreover, we assume that the regime of interest for communication systems is one of low-to-moderate nonlinearity. In other words, the linear solution $E_{\mathrm{LIN}}(z,f)$ is not too different from $E(z,f)$. This assumption amounts to a perturbative approach to the solution of the NLSE, which can only be accurate as long as the perturbation remains "small". The validity of such assumption has been verified a posteriori by the successful model validations in [14] and [15]. It can also be justified by formally showing that the optimum operating regime of optical systems is one where nonlinearity disturbance is always less than ASE noise induced disturbance. This finding has been confirmed both simulatively [34] and experimentally [35]. This clearly means that the signal constellation is not completely disrupted, but only perturbed by NLI, so that a perturbative approach appears reasonable.

According to all the previous assumptions, we can then write:

$$Q_{\mathrm{NLI},\tilde{A}_i}\left(z,f\right) \approx -j\gamma E_{\mathrm{LNI}}\left(z,f\right) * E_{\mathrm{LNI}}^{*}\left(z,-f\right) * E_{\mathrm{LNI}}\left(z,f\right) \tag{2-19}$$

Substituting Eq. (2-17) into Eq. (2-19):

$$
\begin{aligned}
Q_{\mathrm{NLI},\tilde{A}_i}\left(z,f\right) = -j\gamma e^{-3\alpha z} \int_{-\infty}^{\infty} \int_{-\infty}^{\infty} e^{-j\left[\beta(f_1)-\beta(f_1-f_2)+\beta(f-f_2)\right]z} \cdot \\
\cdot E\left(0,f_1\right)E^{*}\left(0,f_1-f_2\right)E\left(0,f-f_2\right)df_1 df_2
\end{aligned}
\tag{2-20}
$$

We then substitute the signal model of Eq. (2-1) into Eq. (2-20):

$$
\begin{aligned}
Q_{\mathrm{NLI},\tilde{A}_i}\left(z,f\right) = &-j\gamma f_0^{\frac{3}{2}} e^{-3\alpha z} \sum_{m=-\infty}^{\infty}\sum_{n=-\infty}^{\infty}\sum_{k=-\infty}^{\infty} \\
& \xi_m \xi_n^{*} \xi_k \int_{-\infty}^{\infty}\int_{-\infty}^{\infty} e^{-j\left[\beta(f_1)-\beta(f_1-f_2)+\beta(f-f_2)\right]z} \\
& \overline{\sqrt{G_{\mathrm{Tx}}\left(f_1\right)G_{\mathrm{Tx}}\left(f_1-f_2\right)G_{\mathrm{Tx}}\left(f-f_2\right)}} \\
& \delta\left(f_1-mf_0\right)\delta\left(f_1-f_2-nf_0\right)\delta\left(f-f_2-kf_0\right)df_2 df_1 \\
= &-j\gamma f_0^{\frac{3}{2}} e^{-3\alpha z} \sum_{i=-\infty}^{\infty} \delta\left(f-if_0\right) \sum_{m,n,k\in\tilde{A}_i} \xi_m \xi_n^{*} \xi_k \\
& e^{-j\left[\beta(mf_0)-\beta(nf_0)+\beta(kf_0)\right]z} \overline{\sqrt{G_{\mathrm{Tx}}\left(mf_0\right)G_{\mathrm{Tx}}\left(nf_0\right)G_{\mathrm{Tx}}\left(kf_0\right)}}
\end{aligned}
\tag{2-21}
$$

Therefore, we have obtained the proper source term that, substituted into Eq. (2-18), makes it possible to compute an approximate expression of $E_{\mathrm{NLI}}\left(z,f\right)$.

2.1.1.3 The NLI Field

We first compute the NLI field for one span, and then derive the solution after any number of spans. Inserting Eq. (2-21) into Eq. (2-18), we get:

$$
\begin{aligned}
E_{\mathrm{NLI}}\left(z,f\right) = &-j\gamma f_0^{\frac{3}{2}} e^{-j\beta(f)z} e^{-\alpha z} \\
& \sum_{i=-\infty}^{\infty} \delta\left(f-if_0\right) \sum_{m,n,k\in\tilde{A}_i} \overline{\sqrt{G_{\mathrm{Tx}}\left(mf_0\right)G_{\mathrm{Tx}}\left(nf_0\right)G_{\mathrm{Tx}}\left(kf_0\right)}} \\
& \xi_m \xi_n^{*} \xi_k \cdot \int_{0}^{z} e^{-2\alpha z'} e^{j\left\{\beta\left(\left[m-n+k\right]f_0\right)-\beta(mf_0)+\beta(nf_0)-\beta(kf_0)\right\}z'} dz'
\end{aligned}
\tag{2-22}
$$

The last integral is a well-known one, akin to the FWM efficiency. Solving for it, we get:

$$
\begin{aligned}
E_{\mathrm{NLI}}(z,f) &= \sum_{i=-\infty}^{\infty} \delta(f-if_0) \cdot \Bigg[-j\gamma f_0^{\frac{3}{2}} e^{-j\beta(if_0)z} e^{-\alpha z} \\
&\quad \sum_{m,n,k\in\tilde{A}_i} \xi_m \xi_n^* \xi_k \sqrt{G_{\mathrm{Tx}}(mf_0) G_{\mathrm{Tx}}(nf_0) G_{\mathrm{Tx}}(kf_0)} \\
&\quad \frac{1-e^{-2\alpha z} e^{j\{\beta([m-n+k]f_0)-\beta(mf_0)+\beta(nf_0)-\beta(kf_0)\}z}}{2\alpha - j\{\beta([m-n+k]f_0)-\beta(mf_0)+\beta(nf_0)-\beta(kf_0)\}} \Bigg] \\
&= \sum_{i=-\infty}^{\infty} \mu_i \delta(f-if_0)
\end{aligned}
\tag{2-23}
$$

that is the NLI disturbance Fourier transform is a set of deltas. This means that $E_{\mathrm{NLI}}(z,f)$ is still a periodic signal of period $T_0 = 1/f_0$. According to the theory of periodic signals, the PSD of a given instance of such process would be:

$$
\Theta_{E_{\mathrm{NLI}}}(f) = \sum_i |\mu_i|^2 \delta(f-if_0)
\tag{2-24}
$$

The overall random process average PSD is then simply:

$$
G_{E_{\mathrm{NLI}}}(f) = \mathbf{E}\{\Theta_{E_{\mathrm{NLI}}}(f)\} = \sum_i \mathbf{E}\{|\mu_i|^2\} \delta(f-if_0)
\tag{2-25}
$$

where $\mathbf{E}$ is the statistical expectation operator. In other words, the average NLI power carried by a spectral line at frequency if_0 is found as $\mathbf{E}\{|\mu_i|^2\}$. Since the NLI power is the quantity of interest for performance evaluation, we now concentrate on the assessment of $\mathbf{E}\{|\mu_i|^2\}$.

2.1.1.4 The NLI Power

To evaluate $\mathbf{E}\{|\mu_i|^2\}$ we need to focus on each specific frequency component if_0. We can then write:

$$
\begin{aligned}
\mathbf{E}\{|\mu_i|^2\} &= \gamma^2 f_0^3 e^{-2\alpha z} \sum_{m,n,k\in\tilde{A}_i} \sum_{m',n',k'\in\tilde{A}_i} \mathrm{E}\{\xi_m \xi_n^* \xi_k \xi_{m'} \xi_{n'}^* \xi_{k'}\} \\
&\quad \sqrt{G_{\mathrm{Tx}}(mf_0) G_{\mathrm{Tx}}(nf_0) G_{\mathrm{Tx}}(kf_0)} \sqrt{G_{\mathrm{Tx}}(m'f_0) G_{\mathrm{Tx}}(n'f_0) G_{\mathrm{Tx}}(k'f_0)} \\
&\quad \frac{1-e^{-2\alpha z} e^{j\{\beta([m-n+k]f_0)-\beta(mf_0)+\beta(nf_0)-\beta(kf_0)\}z}}{2\alpha - j\{\beta([m-n+k]f_0)-\beta(mf_0)+\beta(nf_0)-\beta(kf_0)\}} \\
&\quad \frac{1-e^{-2\alpha z} e^{-j\{\beta([m'-n'+k']f_0)-\beta(m'f_0)+\beta(n'f_0)-\beta(k'f_0)\}z}}{2\alpha + j\{\beta([m'-n'+k']f_0)-\beta(m'f_0)+\beta(n'f_0)-\beta(k'f_0)\}}
\end{aligned}
\tag{2-26}
$$

The double summation within Eq. (2-26) gives rise to various classes of products. Most of such products, however, average to zero. Specifically, every time in the average

$\mathbf{E}\left\{\xi_m\xi_n^*\xi_k\xi_{m'}^*\xi_{n'}\xi_{k'}^*\right\}$, one index appears only once, then the overall average goes to zero. This is because, as discussed, all the ξ_n's in Eq. (2-1) are zero-mean and independent of one another. A thorough discussion of the various classes of terms is supplied in Appendix A of [16]. It turns out that the only classes of terms that are significant are those whereby:

$$m = m', \quad n = n', \quad k = k', \quad m \neq n, n \neq k, m \neq k$$
$$m = k', \quad n = n', \quad k = m', \quad m \neq n, n \neq k, m \neq k \tag{2-27}$$

for which it is:

$$\mathbf{E}\left\{\xi_m\xi_n^*\xi_k\xi_{m'}^*\xi_{n'}\xi_{k'}^*\right\} = \mathbf{E}\left\{|\xi_m|^2\right\}\mathbf{E}\left\{|\xi_n|^2\right\}\mathbf{E}\left\{|\xi_k|^2\right\} = 1 \tag{2-28}$$

As a result, $\mathbf{E}\left\{|\mu_i|^2\right\}$ becomes:

$$\mathbf{E}\left\{|\mu_i|^2\right\} \approx 2\gamma^2 f_0^3 e^{-2\alpha z} \sum_m \sum_k G_{\text{Tx}}\left(mf_0\right) G_{\text{Tx}}\left(kf_0\right) G_{\text{Tx}}\left([m+k-i]f_0\right)$$

$$\left|\frac{1-e^{-2\alpha z}e^{j\left\{\beta(if_0)-\beta(mf_0)+\beta([m+k-i]f_0)-\beta(kf_0)\right\}z}}{2\alpha - j\left\{\beta(if_0)-\beta(mf_0)+\beta([m+k-i]f_0)-\beta(kf_0)\right\}}\right|^2 \tag{2-29}$$

After averaging, the double summation over the set of triples A_i simplifies to a double summation over two independent scalar indices. By substituting Eq. (2-29) into Eq. (2-25) we obtain the PSD characterization of NLI noise, for a single polarization and a single span:

$$G_{E_{\text{NLI}}}(f) = 2\gamma^2 f_0^3 e^{-2\alpha z} \sum_i \delta(f-if_0)$$

$$\sum_m \sum_k G_{\text{Tx}}\left(mf_0\right) G_{\text{Tx}}\left(kf_0\right) G_{\text{Tx}}\left([m+k-i]f_0\right) \tag{2-30}$$

$$\left|\frac{1-e^{-2\alpha z}e^{j\left\{\beta(if_0)-\beta(mf_0)+\beta([m+k-i]f_0)-\beta(kf_0)\right\}z}}{2\alpha - j\left\{\beta(if_0)-\beta(mf_0)+\beta([m+k-i]f_0)-\beta(kf_0)\right\}}\right|^2$$

2.1.2 Analytical derivation for a dual-polarization system

To account for dual-polarization, we first need to suitably rewrite the Tx signal model. In this thesis we assume PM transmission, with independent modulation on the two polarizations. We also assume that the Tx PSD is the same over either polarization. Such formats as PM-QPSK or PM-16QAM comply with these assumptions. Then, the transmitted signal is simply the juxtaposition of two single-polarization signals:

$$\vec{E}(0,f) = E_x(0,f)\hat{x} + E_y(0,f)\hat{y}$$

$$E_x(0,f) = \sqrt{f_0 \frac{G_{\mathrm{Tx}}(f)}{2}} \sum_{n=-\infty}^{+\infty} \xi_{x,n} \delta(f - nf_0) \qquad (2\text{-}31)$$

$$E_y(0,f) = \sqrt{f_0 \frac{G_{\mathrm{Tx}}(f)}{2}} \sum_{n=-\infty}^{+\infty} \xi_{y,n} \delta(f - nf_0)$$

where the overhanging arrow indicates that the electric field is now a vector quantity. Note the factor 1/2 multiplying $G_{\mathrm{Tx}}(f)$. The reason for its presence is that this way we can still write the overall transmitted power through Eq. (21), simply by defining:

$$G_{\mathrm{Tx}}(f) = G_{\mathrm{Tx},x}(f) + G_{\mathrm{Tx},y}(f) \qquad (2\text{-}32)$$

where $G_{\mathrm{Tx},x}(f)$ and $G_{\mathrm{Tx},y}(f)$ are the PSDs of the signal on the x and y polarizations, respectively. We then use the ME to model dual-polarization nonlinear propagation. In frequency-domain we have:

$$\frac{\partial}{\partial z} E_x(z,f) = -j\beta(f) E_x(z,f) - \alpha E_x(z,f)$$

$$- j\gamma \frac{8}{9}\left[E_x(z,f) * E_x^*(z,-f) + E_y(z,f) * E_y^*(z,-f) \right] * E_x(z,f)$$

$$\frac{\partial}{\partial z} E_y(z,f) = -j\beta(f) E_y(z,f) - \alpha E_y(z,f) \qquad (2\text{-}33)$$

$$- j\gamma \frac{8}{9}\left[E_x(z,f) * E_x^*(z,-f) + E_y(z,f) * E_y^*(z,-f) \right] * E_y(z,f)$$

Note that the two polarizations are coupled through the Kerr term. As it was done for the NLSE, we assume the Kerr term to be a source term, calculated assuming linear propagation:

$$\frac{\partial}{\partial z} E_x(z,f) = -j\beta(f) E_x(z,f) - \alpha E_x(z,f) + Q_{\mathrm{NLI},x}(z,f)$$

$$\frac{\partial}{\partial z} E_y(z,f) = -j\beta(f) E_y(z,f) - \alpha E_y(z,f) + Q_{\mathrm{NLI},y}(z,f) \qquad (2\text{-}34)$$

where:

$$Q_{\mathrm{NLI},x}(z,f) = -j\gamma \frac{8}{9} E_{\mathrm{LIN},x}(z,f) * E_{\mathrm{LIN},x}^*(z,-f) * E_{\mathrm{LIN},x}(z,f)$$

$$- j\gamma \frac{8}{9} E_{\mathrm{LIN},y}(z,f) * E_{\mathrm{LIN},y}^*(z,-f) * E_{\mathrm{LIN},x}(z,f) \qquad (2\text{-}35)$$

$$Q_{\mathrm{NLI},y}(z,f) = -j\gamma \frac{8}{9} E_{\mathrm{LIN},y}(z,f) * E^*_{\mathrm{LIN},y}(z,-f) * E_{\mathrm{LIN},y}(z,f)$$

$$-j\gamma \frac{8}{9} E_{\mathrm{LIN},x}(z,f) * E^*_{\mathrm{LIN},x}(z,-f) * E_{\mathrm{LIN},y}(z,f)$$

(2-36)

The linear solutions for the field polarization components are completely independent and are of course similar to Eq. (2-17):

$$E_{\mathrm{LIN},x}(z,f) = E_x(0,f) e^{-j\beta(f)z - \alpha z}$$

$$E_{\mathrm{LIN},y}(z,f) = E_y(0,f) e^{-j\beta(f)z - \alpha z}$$

(2-37)

Then, we exploit the same procedure outlined in Eq. (2-18)-(2-21) to derive the source terms. Their final expressions are very similar to Eq. (2-21). Specifically, for $Q_{\mathrm{NLI},x}(z,f)$ we have:

$$Q_{\mathrm{NLI},x}(z,f) = -j\gamma 2^{-\frac{3}{2}} \frac{8}{9} f_0^{\frac{3}{2}} e^{-3\alpha z} \sum_{m=-\infty}^{\infty} \sum_{n=-\infty}^{\infty} \sum_{k=-\infty}^{\infty}$$

$$\left(\xi_{x,m} \xi^*_{x,n} \xi_{x,k} + \xi_{y,m} \xi^*_{y,n} \xi_{x,k} \right) e^{-j[\beta(mf_0) - \beta(nf_0) + \beta(kf_0)]z} \cdot$$

$$\sqrt{G_{\mathrm{Tx}}(mf_0) G_{\mathrm{Tx}}(nf_0) G_{\mathrm{Tx}}(kf_0)} \delta\left(f - [m - n + k] f_0 \right)$$

(2-38)

The differences between Eq. (2-38) and Eq. (2-21) are: the presence in the former of a factor $2^{-3/2}$ arising from the cube of the factor $2^{-1/2}$ inserted into Eq. (2-31); the factor 8/9 that multiplies the Kerr term in the ME; two products of three RVs rather than just one product, which represent same-polarization and cross-polarization beatings. The expression for the other source term $Q_{\mathrm{NLI},x}(z,f)$ is immediately found by swapping the subscripts x, y in Eq. (2-38).

We can then compute the NLI fields $E_{\mathrm{NLI},x}(z,f)$ and $E_{\mathrm{NLI},y}(z,f)$ following the same procedure as in Eq. (2-22) and Eq. (2-23). The result for $E_{\mathrm{NLI},x}(z,f)$ is:

$$E_{\mathrm{NLI},x}(z,f) = \sum_{i=-\infty}^{\infty} \delta(f - if_0) \cdot \left[-j\gamma 2^{-\frac{3}{2}} \frac{8}{9} f_0^{\frac{3}{2}} e^{-\alpha z} e^{-j\beta(if_0)z} \right.$$

$$\sum_{m,n,k \in \mathbb{A}_i} \left(\xi_{x,m} \xi^*_{x,n} \xi_{x,k} + \xi_{y,m} \xi^*_{y,n} \xi_{x,k} \right) \sqrt{G_{\mathrm{Tx}}(mf_0) G_{\mathrm{Tx}}(nf_0) G_{\mathrm{Tx}}(kf_0)}$$

$$\left. \frac{1 - e^{-2\alpha z} e^{j\{\beta([m-n+k]f_0) - \beta(mf_0) + \beta(nf_0) - \beta(kf_0)\}z}}{2\alpha - j\{\beta([m-n+k]f_0) - \beta(mf_0) + \beta(nf_0) - \beta(kf_0)\}} \right]$$

(2-39)

The result for $E_{\mathrm{NLI},y}(z,f)$ can be found again by swapping the subscripts x, y.

Note that $E_{\mathrm{NLI},x}(z,f)$ and $E_{\mathrm{NLI},y}(z,f)$ can be written as:

$$E_{\mathrm{NLI},x}(z,f)=\sum_{i}\mu_{x,i}\,\delta(f-if_0) \tag{2-40}$$

$$E_{\mathrm{NLI},y}(z,f)=\sum_{i}\mu_{y,i}\,\delta(f-if_0) \tag{2-41}$$

We now want to find the average PSD of the dual-polarization NLI field:

$$\begin{aligned}\vec{E}_{\mathrm{NLI}}(z,f)&=E_{\mathrm{NLI},x}(z,f)\,\hat{x}+E_{\mathrm{NLI},y}(z,f)\,\hat{y}\\&=\sum_{i}\left(\mu_{x,i}\hat{x}+\mu_{y,i}\hat{y}\right)\delta(f-if_0)\end{aligned} \tag{2-42}$$

Such PSD has a form similar to Eq. (2-25):

$$G_{\vec{E}_{\mathrm{NLI}}}(f)=\sum_{i}\left[\mathbf{E}\left\{\left|\mu_{x,i}\right|^2\right\}+\mathbf{E}\left\{\left|\mu_{y,i}\right|^2\right\}\right]\delta(f-if_0) \tag{2-43}$$

where,

$$\begin{aligned}E\left\{\left|\mu_{x,i}\right|^2\right\}=&\frac{8}{81}\gamma^2 f_0^3 e^{-2\alpha z}\sum_{m,n,k\in\tilde{A}_i}\ \sum_{m',n',k'\in\tilde{A}_i}\\&\left[\mathbf{E}\left\{\xi_{x,m}\xi_{x,n}^*\xi_{x,k}\xi_{x,m'}^*\xi_{x,n'}\xi_{x,k'}^*\right\}+\mathbf{E}\left\{\xi_{x,m}\xi_{x,n}^*\xi_{x,k}\xi_{y,m'}^*\xi_{y,n'}\xi_{x,k'}^*\right\}\right.\\&\left.+\mathbf{E}\left\{\xi_{y,m}\xi_{y,n}^*\xi_{x,k}\xi_{x,m'}^*\xi_{x,n'}\xi_{x,k'}^*\right\}+\mathbf{E}\left\{\xi_{y,m}\xi_{y,n}^*\xi_{x,k}\xi_{y,m'}^*\xi_{y,n'}\xi_{x,k'}^*\right\}\right]\\&\sqrt{G_{\mathrm{Tx}}(mf_0)G_{\mathrm{Tx}}(nf_0)G_{\mathrm{Tx}}(kf_0)}\sqrt{G_{\mathrm{Tx}}(m'f_0)G_{\mathrm{Tx}}(n'f_0)G_{\mathrm{Tx}}(k'f_0)}\\&\frac{1-e^{-2\alpha z}e^{j\left\{\beta([m-n+k]f_0)-\beta(mf_0)+\beta(nf_0)-\beta(kf_0)\right\}z}}{2\alpha-j\left\{\beta([m-n+k]f_0)-\beta(mf_0)+\beta(nf_0)-\beta(kf_0)\right\}}\\&\frac{1-e^{-2\alpha z}e^{-j\left\{\beta([m'-n'+k']f_0)-\beta(m'f_0)+\beta(n'f_0)-\beta(k'f_0)\right\}z}}{2\alpha+j\left\{\beta([m'-n'+k']f_0)-\beta(m'f_0)+\beta(n'f_0)-\beta(k'f_0)\right\}}\end{aligned} \tag{2-44}$$

The main difference with respect to Eq. (2-26), apart from the leading factor 8/81, is the rather complex sum of statistical averages. A thorough discussion of such averaging process is reported in Appendix A in [16]. Here we summarize its results.

The first average contains all x-polarization random variables and therefore it behaves exactly like the single average in Eq. (2-27). The second and third averages are always zero or are irrelevant. The fourth average is the one that accounts for cross-polarization NLI, where only the class of terms in Eq. (2-45) can make it evaluate to 1.

$$m=m',\quad n=n',\quad k=k',\quad m\neq n,n\neq k,m\neq k \tag{2-45}$$

After all averaging has been carried out, we can get:

$$\mathbf{E}\left\{\left|\mu_{x,i}\right|^2\right\} \approx \frac{8}{27}\gamma^2 f_0^3 e^{-2\alpha z} \sum_m \sum_k G_{\mathrm{Tx}}\left(mf_0\right)G_{\mathrm{Tx}}\left(kf_0\right)G_{\mathrm{Tx}}\left(\left[m+k-i\right]f_0\right)$$

$$\left|\frac{1-e^{-2\alpha z}e^{j\left\{\beta\left(if_0\right)-\beta\left(mf_0\right)+\beta\left(\left[m+k-i\right]f_0\right)-\beta\left(kf_0\right)\right\}z}}{2\alpha-j\left\{\beta\left(if_0\right)-\beta\left(mf_0\right)+\beta\left(\left[m+k-i\right]f_0\right)-\beta\left(kf_0\right)\right\}}\right|^2 \qquad (2\text{-}46)$$

Regarding the y-polarization term, its asymptotic approximation is identical to Eq. (2-46). Putting the two results together, we can finally get:

$$G_{\tilde{E}_{\mathrm{NLI}}}(f) = \frac{16}{27}\gamma^2 f_0^3 e^{-2\alpha z} \sum_m \sum_k G_{\mathrm{Tx}}\left(mf_0\right)G_{\mathrm{Tx}}\left(kf_0\right)G_{\mathrm{Tx}}\left(\left[m+k-i\right]f_0\right)$$

$$\left|\frac{1-e^{-2\alpha z}e^{j\left\{\beta\left(if_0\right)-\beta\left(mf_0\right)+\beta\left(\left[m+k-i\right]f_0\right)-\beta\left(kf_0\right)\right\}z}}{2\alpha-j\left\{\beta\left(if_0\right)-\beta\left(mf_0\right)+\beta\left(\left[m+k-i\right]f_0\right)-\beta\left(kf_0\right)\right\}}\right|^2 \qquad (2\text{-}47)$$

This equation provides an analytical expression for the PSD of two polarization NLI noise after one span of fiber.

2.1.3 Accounting for multiple identical spans

If identical spans of homogenous fibers are assumed, with lumped amplifiers exactly compensating for the loss of each span (including the last span), then the resulting NLI field at the end of the link $E_{\mathrm{NLI}}\left(N_s L_s, f\right)$, for dual-polarization, is given by:

$$\vec{E}_{\mathrm{NLI}}\left(N_s L_s, f\right) = E_{\mathrm{NLI}}^{(1)}\left(N_s L_s, f\right) + E_{\mathrm{NLI}}^{(2)}\left(N_s L_s, f\right) +$$

$$+ E_{\mathrm{NLI}}^{(3)}\left(N_s L_s, f\right) + \ldots + E_{\mathrm{NLI}}^{(N_s)}\left(N_s L_s, f\right)$$

$$= -j\gamma 2^{-\frac{3}{2}}\frac{8}{9}f_0^{\frac{3}{2}} \sum_{m,n,k\in\tilde{A}_i} \xi_m\xi_n^*\xi_k e^{-j\beta\left(\left[m-n+k\right]f_0\right)N_s L_s} \cdot$$

$$\sqrt{G_{\mathrm{Tx}}\left(mf_0\right)G_{\mathrm{Tx}}\left(nf_0\right)G_{\mathrm{Tx}}\left(kf_0\right)}\delta\left(f-\left[m-n+k\right]f_0\right)\cdot$$

$$\left[1+e^{j\left\{\beta\left(\left[m-n+k\right]f_0\right)-\beta\left(mf_0\right)+\beta\left(nf_0\right)-\beta\left(kf_0\right)\right\}\cdot L_s} +\right. \qquad (2\text{-}48)$$

$$+e^{j\left\{\beta\left(\left[m-n+k\right]f_0\right)-\beta\left(mf_0\right)+\beta\left(nf_0\right)-\beta\left(kf_0\right)\right\}\cdot 2L_s} +\ldots$$

$$\left.+e^{j\left\{\beta\left(\left[m-n+k\right]f_0\right)-\beta\left(mf_0\right)+\beta\left(nf_0\right)-\beta\left(kf_0\right)\right\}\cdot\left(N_s-1\right)L_s}\right]\cdot$$

$$\frac{1-e^{-2\alpha L_s}e^{j\left\{\beta\left(\left[m-n+k\right]f_0\right)-\beta\left(mf_0\right)+\beta\left(nf_0\right)-\beta\left(kf_0\right)\right\}L_s}}{2\alpha-j\left\{\beta\left(\left[m-n+k\right]f_0\right)-\beta\left(mf_0\right)+\beta\left(nf_0\right)-\beta\left(kf_0\right)\right\}} \cdot$$

where L_s is the span length, N_s is the number of spans, $E_{\mathrm{NLI}}^{(h)}\left(N_s L_s, f\right)$ is the NLI field

produced in the h-th span, propagated to the end of the link. It is interesting to see that all the contributions $E_{\text{NLI}}^{(h)}(N_s L_s, f)$ are formally identical, except for a phase factor, which gives rise to the factor:

$$
\begin{aligned}
&\left[1 + e^{j\{\beta([m-n+k]f_0)-\beta(mf_0)+\beta(nf_0)-\beta(kf_0)\}\cdot L_s} + \right. \\
&+ e^{j\{\beta([m-n+k]f_0)-\beta(mf_0)+\beta(nf_0)-\beta(kf_0)\}\cdot 2L_s} + \dots \\
&\left. + e^{j\{\beta([m-n+k]f_0)-\beta(mf_0)+\beta(nf_0)-\beta(kf_0)\}\cdot(N_s-1)L_s} \right]
\end{aligned}
\tag{2-49}
$$

This factor represents the coherent interference of NLI contributions, due to each span, at the end of the link. It is a truncated geometric series and can be summed up analytically:

$$
\begin{aligned}
&\vec{E}_{\text{NLI}}(N_s L_s, f) \\
&= -j\gamma 2^{-\frac{3}{2}} \frac{8}{9} f_0^{\frac{3}{2}} \sum_{m,n,k \in \tilde{A}_i} \xi_m \xi_n^* \xi_k e^{-j\beta([m-n+k]f_0)N_s L_s} \cdot \\
&\sqrt{G_{\text{Tx}}(mf_0) G_{\text{Tx}}(nf_0) G_{\text{Tx}}(kf_0)} \delta(f - [m-n+k]f_0) \cdot \\
&e^{j\{\beta([m-n+k]f_0)-\beta(mf_0)+\beta(nf_0)-\beta(kf_0)\}\cdot(N_s-1)L_s/2} \cdot \\
&\frac{\sin\left(\{\beta([m-n+k]f_0)-\beta(mf_0)+\beta(nf_0)-\beta(kf_0)\}\cdot N_s L_s / 2\right)}{\sin\left(\{\beta([m-n+k]f_0)-\beta(mf_0)+\beta(nf_0)-\beta(kf_0)\}\cdot L_s / 2\right)} \cdot \\
&\frac{1 - e^{-2\alpha L_s} e^{j\{\beta([m-n+k]f_0)-\beta(mf_0)+\beta(nf_0)-\beta(kf_0)\}L_s}}{2\alpha - j\{\beta([m-n+k]f_0)-\beta(mf_0)+\beta(nf_0)-\beta(kf_0)\}} \cdot
\end{aligned}
\tag{2-50}
$$

The $\sin(N_s \Phi/2)/\sin(\Phi/2)$ is sometimes called "phased array" factor because it formally looks like a phased-array antenna radiation diagram. Such interference effect, with similar analytical form, was first pointed out in the context of conventional FWM calculations [36, 37]. For a detailed discussion of the implications of the phased array factor on NLI noise accumulation see [17], Sect. XI-C.

The final result for the NLI PSD after N_s identical spans, with dual-polarization, is:

$$G_{\vec{E}_{\mathrm{NLI}}}(f) = \frac{16}{27}\gamma^2 f_0^3 \sum_i \delta(f - if_0)$$

$$\sum_m \sum_k G_{\mathrm{Tx}}(mf_0) G_{\mathrm{Tx}}(kf_0) G_{\mathrm{Tx}}([m+k-i]f_0)$$

$$\left| \frac{1 - e^{-2\alpha L_s} e^{j\{\beta(if_0) - \beta(mf_0) + \beta([m+k-i]f_0) - \beta(kf_0)\}L_s}}{2\alpha - j\{\beta(if_0) - \beta(mf_0) + \beta([m+k-i]f_0) - \beta(kf_0)\}} \right|^2 \tag{2-51}$$

$$\frac{\sin^2\left(\{\beta(if_0) - \beta(mf_0) + \beta([m+k-i]f_0) - \beta(kf_0)\} \cdot N_s L_s / 2\right)}{\sin^2\left(\{\beta(if_0) - \beta(mf_0) + \beta([m+k-i]f_0) - \beta(kf_0)\} \cdot L_s / 2\right)}$$

Then, we transit to a "continuous spectrum":

$$G_{\vec{E}_{\mathrm{NLI}}}(f) = \frac{16}{27}\gamma^2 \int_{-\infty}^{\infty}\int_{-\infty}^{\infty} G_{\mathrm{Tx}}(f_1) G_{\mathrm{Tx}}(f_2) G_{\mathrm{Tx}}(f_1 + f_2 - f)$$

$$\left| \frac{1 - e^{-2\alpha L_s} e^{j\{\beta(f_1+f_2-f) - \beta(f_1) + \beta(f) - \beta(f_2)\}L_s}}{2\alpha - j\{\beta(f_1+f_2-f) - \beta(f_1) + \beta(f) - \beta(f_2)\}} \right|^2 \tag{2-52}$$

$$\frac{\sin^2\left(\{\beta(f_1+f_2-f) - \beta(f_1) + \beta(f) - \beta(f_2)\} \cdot N_s L_s / 2\right)}{\sin^2\left(\{\beta(f_1+f_2-f) - \beta(f_1) + \beta(f) - \beta(f_2)\} \cdot L_s / 2\right)} df_1 df_2$$

If we only consider second-order fiber dispersion β_2 and third-order fiber dispersion β_3, the propagation constant $\beta(f)$ can be written as:

$$\beta(f) = \frac{\beta_2}{2}(2\pi f)^2 + \frac{\beta_3}{6}(2\pi f)^3 = 2\pi^2 \beta_2 f^2 + \frac{4}{3}\pi^3 \beta_3 f^3 \tag{2-53}$$

Then the term $\{\beta(f_1 + f_2 - f) - \beta(f_1) + \beta(f) - \beta(f_2)\}$ in Eq. (2-52) can be explicitly expressed as:

$$\{\beta(f_1 + f_2 - f) - \beta(f_1) + \beta(f) - \beta(f_2)\}$$

$$= \left(2\pi^2 \beta_2 (f_1 + f_2 - f)^2 + \frac{4}{3}\pi^3 \beta_3 (f_1 + f_2 - f)^3\right) +$$

$$- \left(2\pi^2 \beta_2 f_1^2 + \frac{4}{3}\pi^3 \beta_3 f_1^3\right) + \left(2\pi^2 \beta_2 f^2 + \frac{4}{3}\pi^3 \beta_3 f^3\right) + \tag{2-54}$$

$$- \left(2\pi^2 \beta_2 f_2^2 + \frac{4}{3}\pi^3 \beta_3 f_2^3\right)$$

$$= 4\pi^2 (f_1 - f)(f_2 - f)\left[\beta_2 + \pi\beta_3(f_1 + f_2)\right]$$

Substituting Eq. (2-54) into Eq. (2-52), we can obtain:

$$G_{\bar{E}_{\mathrm{NLI}}}(f) = \frac{16}{27}\gamma^2 \int\limits_{-\infty}^{\infty}\int\limits_{-\infty}^{\infty} G_{\mathrm{Tx}}(f_1)G_{\mathrm{Tx}}(f_2)G_{\mathrm{Tx}}(f_1+f_2-f)$$

$$\left| \frac{1-e^{-2\alpha L_s}e^{j4\pi^2(f_1-f)(f_2-f)\left[\beta_2+\pi\beta_3(f_1+f_2)\right]L_s}}{2\alpha-j4\pi^2(f_1-f)(f_2-f)\left[\beta_2+\pi\beta_3(f_1+f_2)\right]} \right|^2 \tag{2-55}$$

$$\frac{\sin^2\left(2\pi^2(f_1-f)(f_2-f)\left[\beta_2+\pi\beta_3(f_1+f_2)\right]N_sL_s\right)}{\sin^2\left(2\pi^2(f_1-f)(f_2-f)\left[\beta_2+\pi\beta_3(f_1+f_2)\right]L_s\right)} df_1 df_2$$

Obviously, by setting $\beta_3=0$, Eq. (2-55) can be expressed as a function of β_2:

$$G_{\bar{E}_{\mathrm{NLI}}}(f) = \frac{16}{27}\gamma^2 \int\limits_{-\infty}^{\infty}\int\limits_{-\infty}^{\infty} G_{\mathrm{Tx}}(f_1)G_{\mathrm{Tx}}(f_2)G_{\mathrm{Tx}}(f_1+f_2-f)$$

$$\left| \frac{1-e^{-2\alpha L_s}e^{j4\pi^2\beta_2(f_1-f)(f_2-f)L_s}}{2\alpha-j4\pi^2\beta_2(f_1-f)(f_2-f)} \right|^2 \tag{2-56}$$

$$\frac{\sin^2\left(2\pi^2\beta_2(f_1-f)(f_2-f)N_sL_s\right)}{\sin^2\left(2\pi^2\beta_2(f_1-f)(f_2-f)L_s\right)} df_1 df_2$$

which is the so-called GN model reference formula (GNRF), as reported in [17].

2.2 Comparison with GNRF

In this section, we compared Eq. (2-55) with the GNRF Eq. (2-56) to study the effect of β_3. we looked at the normalized PSD defined as:

$$\eta = \frac{G_{\bar{E}_{\mathrm{NLI}}}(f)}{P_{\mathrm{WDM}}^3} \tag{2-57}$$

This parameter reports the total NLI noise spectrally distributed over the total WDM bandwidth, normalized through the total power P_{WDM}^{-3}. Therefore, it does not depend on the launch power. The simulated system data are as follows:

- ideal Nyquist WDM Tx with rectangular power spectrum;
- bandwidth 1 THz, central frequency 193.41 THz (corresponding to 1550 nm);
- span length 100 km, 10 spans;
- 8 different fibers with parameters reported in Table 2-1, where S is the dispersion slope.

Table 2-1: Parameters of the fiber types

Fiber	α [dB/km]	γ [1/W/km]	β_2 [ps^2/km]	S [ps/nm^2/km]	β_3 [ps^3/km]
SMF	0.2	1.3	-21	0.057	0.12736
NZDSF1	0.2	1.3	-4	0.057	0.09931
NZDSF2	0.2	1.3	-1	0.057	0.09437
NZDSF3	0.2	1.3	-0.3	0.057	0.09322
NZDSF4	0.2	1.3	-0.1	0.057	0.09289
NZDSF5	0.2	1.3	-0.05	0.057	0.09281
NZDSF6	0.2	1.3	-0.01	0.057	0.09274
DSF	0.2	1.3	0	0.057	0.09273

In order to concentrate on the effect of β_3, we assume that all fiber types have the same attenuation, the same nonlinearity and the same dispersion slope. The last parameter β_3 can be calculated through β_3 and S. Knowing that:

$$D = -\frac{2\pi c}{\lambda^2} \cdot \beta_2 \qquad (2\text{-}58)$$

$$S = -\frac{2}{\lambda} \cdot D + \left(\frac{2\pi c}{\lambda^2}\right)^2 \cdot \beta_3 \qquad (2\text{-}59)$$

then, substituting Eq. (2-59) into Eq. (2-58), we can get:

$$\beta_3 = \frac{\lambda^4}{4\pi^2 c^2} S - \frac{\lambda}{\pi c} \beta_2 \qquad (2\text{-}60)$$

Looking at β_3 in Table 2-1, it gets more and more important from SMF to DSF. The plots in Fig. 2-1 show the comparison of these two versions for all fibers. For a high dispersion SMF, there is almost no difference between these two models, so that the effect of β_3 is negligible. As β_2 becomes smaller and smaller, η from Eq. (2-56) remains symmetric about the central frequency, and the value at the central frequency grows larger and larger until it reaches its maximum when $\beta_2 = 0$. However, η from Eq.

(2-55) does not follow the same trend. Going to NZDSF1, the maximum already shows up at a different frequency from the central one. Then the maximum goes to a higher and higher frequency and its value also keeps growing. From NZDSF5, the maximum starts to shift to the central frequency, but its value still grows. Until NZDSF6, the maximum value reaches to its maximum, but it keeps moving to the central frequency. In the end, $\beta_2 = 0$, η from Eq. (2-55) goes back to symmetric about the central frequency, and its difference from η from Eq. (2-56) is very large.

The results in Fig. 2-1 demonstrate that third-order dispersion has a very substantial effect on nonlinearity, especially near a fiber dispersion-zero. However, It should be mentioned that even taking β_3 into account, the GN model still cannot accurately evaluate NLI accumulation along a link. We have to remove the signal Gaussianity approximation. This will be discussed in detail in Chapter 3. However, the calculations of this chapter are still useful since they constitute on the two main terms appearing in the more accurate EGN model.
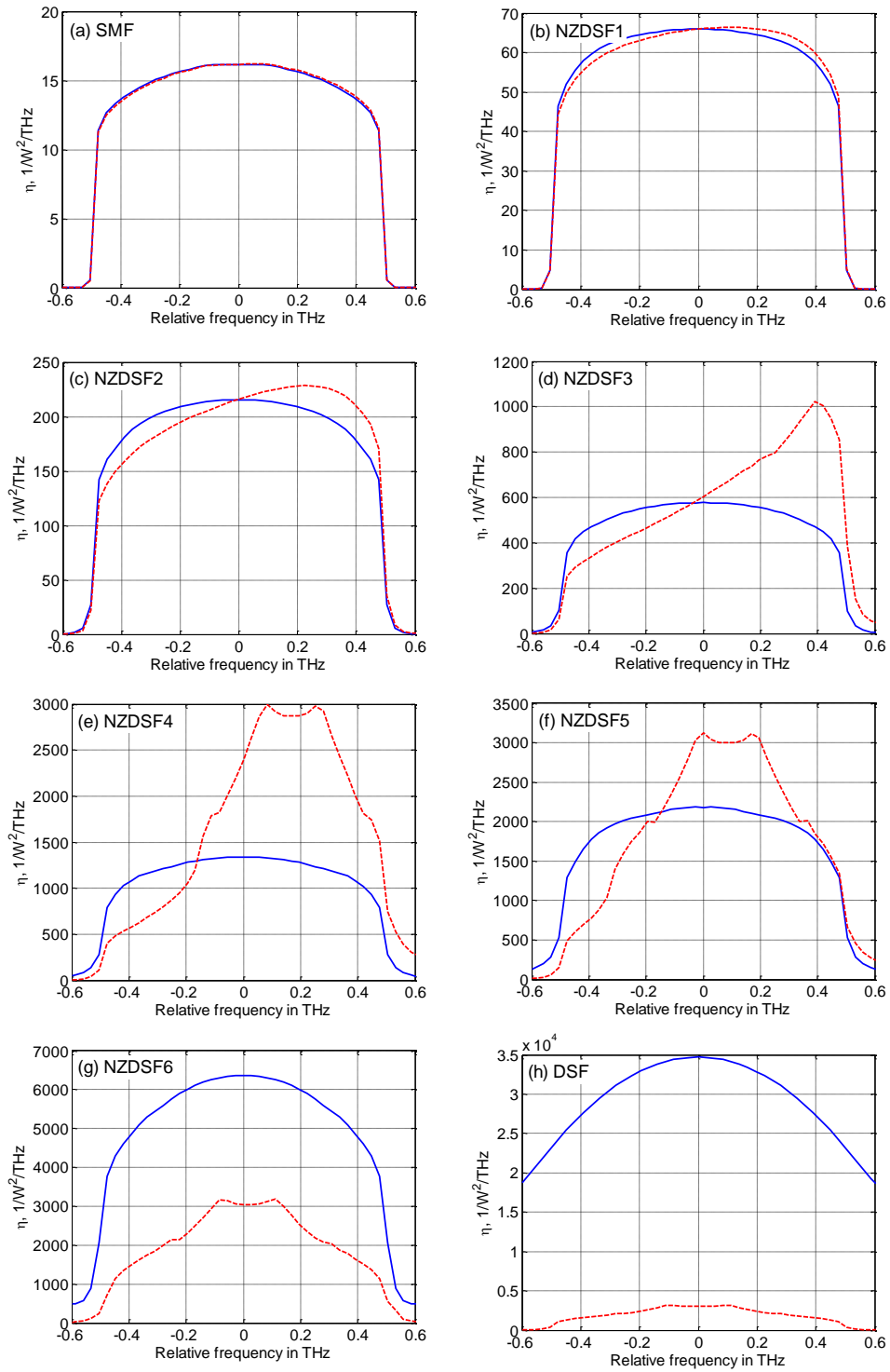
Fig. 2-1: Plot of normalized nonlinear PSD η at the 10th span, assuming Nyquist WDM system with 1 THz bandwidth. The frequencies on the horizontal axis represent the relative values to the central frequency 193.41 THz. From (a) to (h), the figures are mapping to the fiber types from the first SMF to the eighth DSF reported in Table 2-1. Blue solid curve: GNRF in Eq. (2-56). Red dashed curve: inclusion of β_3 as written in Eq. (2-55).

Chapter 3   The EGN model

The GN model is an approximate tool for predicting the system maximum reach performance, if it is used to evaluate the detailed span-by-span characterization of NLI accumulation along a link, its predictions may be affected by a substantial error.

In Fig. 3-1, we looked at NLI prediction of the GN model vs. simulation for a system:

- 9 PM-QPSK channels at 32 GBaud;
- raised-cosine power spectrum with roll-off parameter 0.05;
- SMF with D =16.7 ps/(nm km), γ =1.3 1/(W km), α_{dB} =0.22 dB/km;
- 50 spans with 100 or 60 km per span.

The parameter on the vertical axis is the normalized average power η_{NLI}, defined as follows:

$$\eta_{\mathrm{NLI}} = P_{\mathrm{ch}}^{-3} \int\limits_{-R_s/2}^{R_s/2} G_{\mathrm{NLI}}\left(f\right) df \tag{3-1}$$

It collects the total NLI noise spectrally located over the center channel, normalized through P_{ch}^{-3} so that η_{NLI} does not depend on launch power.

In Fig. 3-1(a), the span length is 100 km, which is widely used for terrestrial link studies. At the first span, the GN model is far away from the simulation, with a gap 5.84 dB. This is because the signal is not dispersed enough to be even approximately close to Gaussian noise, as assumed by the GN model. As propagating farther and farther, the GN model gets closer and closer to the simulation. But even at the 50th span, which is the approximate system maximum reach when assuming EDFA amplification with 5.5 dB noise figure, the GN model prediction is still 1.2 dB higher than the simulation. According to the "1/3 rule" in [17], i.e., the system maximum reach loses 1/3 dB per 1 dB of η_{NLI} increment, the system maximum reach will be underestimated 0.4 dB, about 10%.

When the span length is much shorter, like 60 km in Fig. 3-1(b), the GN model performance is worse. At the 50th span, the difference between GN model and simulation goes up to 2.0 dB, corresponding to 0.67 dB (17%) underestimation of the system maximum reach. Therefore, it is desirable to derive a better model for predicting NLI
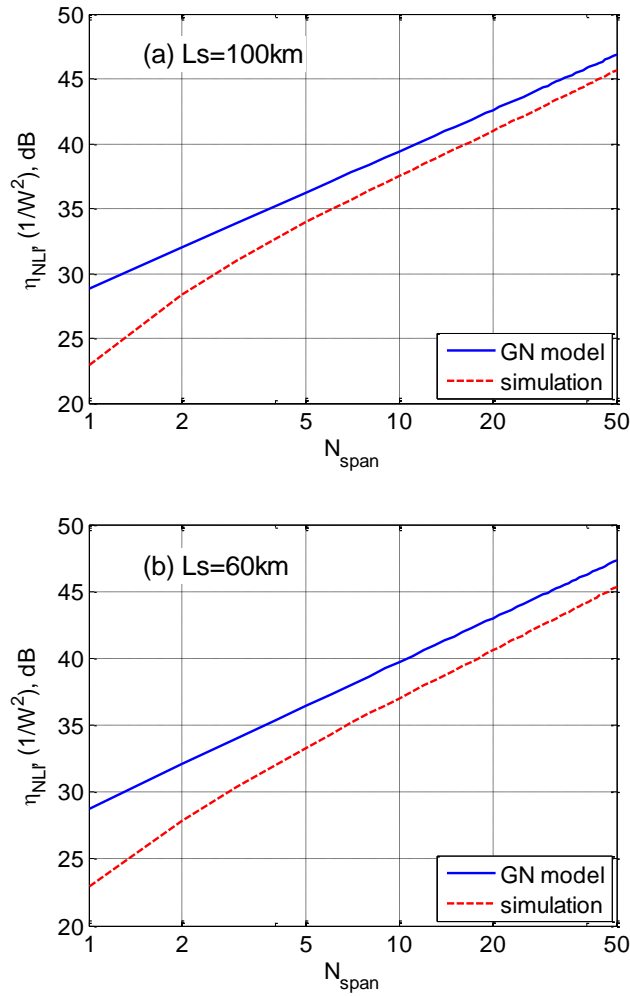
generation more accurately.

Fig. 3-1: Plot of normalized nonlinearity coefficient η_{NLI} vs. number of spans in the link, assuming 9 PM-QPSK channels over SMF, with span length 100 or 60 km. The CUT is the center channel. The symbol rate is 32 GBaud, and the channel spacing is 33.6 GHz. Red dashed line: simulation. Blue solid line: the GN model.

Remarkably, [30] succeeded in analytically removing the signal Gaussianity assumption. A "correction term" to the GN model, limited to XPM, was found. In this chapter we adopt a similar approach to that indicated in [30], and propose the EGN model to completely correct the GN model.

3.1 The EGN model components

The NLI impinging on the channel-under-test (CUT) of a WDM comb is the sum of three types of NLI contributions:

- Self-channel interference (SCI): it is NLI caused by the CUT on itself.

- Cross-channel interference (XCI): it is NLI affecting the CUT caused by the beating of the CUT with any single interfering (INT) channel.

- Multi-channel interference (MCI): it is NLI affecting the CUT, caused by the beating of the CUT with two INT channels simultaneously, or the beating of three INT channels simultaneously.

An equivalent but more formal set of definitions, based on the actual spectral position of the WDM signal components beating together, can be found in [17], Sect. VI. We will investigate these contributions one by one in this section.

In the following, we assume a multi-span link, with lumped amplification and all identical spans. We assume dual polarization from this section on. We also assume that channels have rectangular spectra with same bandwidth, equal to the symbol rate R_s. These limiting assumptions could be removed but they are kept here to avoid excessive complexity in the resulting formulas.

The CUT overall transmitted signal can be written as:

$$S_{CUT}(t) = \sum_n \left(a_{x,n}\hat{x} + a_{y,n}\hat{y} \right) s_{CUT}(t - nT_s)$$
(3-2)

where $s_{CUT}(t)$ is the pulse used by the CUT, a_x and a_y are RVs, representing the generic symbols transmitted in the CUT on x and y polarizations. And similarly for the INT channel, with "b" RV's in the formula. As a simplifying assumption, we assume all pulses to have rectangular Fourier transforms with bandwidth R_s. We set their flat-top value equal to $1/R_s$. Note that if so, then the channel power is given by:

$$P_{CUT} = E\left\{ |a_x|^2 + |a_y|^2 \right\} \quad , \quad P_{INT} = E\left\{ |b_x|^2 + |b_y|^2 \right\}$$
(3-3)

3.1.1 Self-channel interference

The NLI produced by a CUT onto itself is SCI. Its contribution can be rather substantial. In a densely packed, full C-band system, operating at 32 GBaud, it approximately ranges between 20% and 40% of the total NLI power perturbing the CUT, over a wide range of fiber parameters and link lengths.

In [30] SCI was not dealt with and all calculations/simulations assumed that SCI was removed. In theory, removing SCI may be possible using electronic nonlinear-

compensation (NLC). While NLC is a fervid field of investigation, so far it is unclear whether NLC can be effectively implemented in DSP. At present, there are no commercial products incorporating it. Therefore, it seems quite necessary to include SCI as well, in dealing with a GN model upgrade.

In frequency-domain, the signal model for a single channel, can be written as [15]:

$$\vec{E}(f) = E_x(f)\hat{x} + E_y(f)\hat{y} \tag{3-4}$$

where:

$$E_x(f) = \sqrt{f_0}\sum_{n=-\infty}^{+\infty} v_{x,n}\delta(f - nf_0) \quad , \quad E_y(f) = \sqrt{f_0}\sum_{n=-\infty}^{+\infty} v_{y,n}\delta(f - nf_0) \tag{3-5}$$

The RVs $v_{x,n}$ and $v_{y,n}$ are defined similar to [15], Appendix B, Eq. (36):

$$v_{x,n} = \sqrt{f_0}\, s_{\mathrm{CUT},x}(nf_0)\sum_{\omega=0}^{W-1} a_{x,\omega} e^{-j\frac{2\pi}{W}\omega n} \quad , \quad v_{y,n} = \sqrt{f_0}\, s_{\mathrm{CUT},y}(nf_0)\sum_{\omega=0}^{W-1} a_{y,\omega} e^{-j\frac{2\pi}{W}\omega n} \tag{3-6}$$

where W is an integer number that can be chosen to be arbitrarily large. $s_{\mathrm{CUT},x}(f)$ and $s_{\mathrm{CUT},y}(f)$ are the Fourier transforms of the pulses used by the CUT on x and y polarizations.

Using the ME, the Kerr term at the fiber input on the x polarization can be written as (see Sect. 2.1.2):

$$Q_{\mathrm{NLI},x}(0,f) = -j\gamma\frac{8}{9}f_0^{3/2}\sum_{i=-\infty}^{+\infty}\delta(f - if_0)\sum_{S_i}\left(v_{x,m}v_{x,n}^* v_{x,k} + v_{x,m}v_{y,n}^* v_{y,k}\right) \tag{3-7}$$

where:

$$S_i \equiv \{(m,n,k) : (m-n+k)f_0 = if_0\} \tag{3-8}$$

The SCI field on the x polarization after a homogenous span of length L_s, can be written as (From this section, we neglect the effect of β_3):

$$E_{\mathrm{SCI},x}(L_s,f) = f_0^{3/2}e^{-\alpha L_s}\sum_{i=-\infty}^{+\infty}\delta(f - if_0)\left[-j\frac{8}{9}e^{-j2\beta_2\pi^2 i^2 f_0^2 L_s}\right.$$
$$\left. \sum_{m,n,k\in S_i}\zeta(k,m,n)\cdot\left(v_{x,m}v_{x,n}^* v_{x,k} + v_{x,m}v_{y,n}^* v_{y,k}\right)\right] \tag{3-9}$$

where:

$$\zeta(k,m,n) = \gamma \frac{1 - e^{-2\alpha L_s} e^{j4\pi^2 \beta_2 f_0^2 (k-n)(m-n) L_s}}{2\alpha - j4\pi^2 \beta_2 f_0^2 (k-n)(m-n)} \tag{3-10}$$

By "homogeneous span" we mean that the fiber parameters are constant over L_s.

The SCI PSD on the *x* polarization at the output of the first span of length L_s is then:

$$G_{\text{SCI},x}(f) = \frac{64}{81} f_0^3 e^{-2\alpha L_s} \sum_{i=-\infty}^{+\infty} \delta(f - if_0) \sum_{m,n,k \in S_i} \sum_{m',n',k' \in S_i} \zeta(k,m,n)\zeta^*(k',m',n')$$

$$\left[\mathrm{E}\{v_{x,m} v_{x,n}^* v_{x,k} v_{x,m'}^* v_{x,n'} v_{x,k'}^*\} + \mathrm{E}\{v_{x,m} v_{x,n}^* v_{x,k} v_{x,m'}^*\} \mathrm{E}\{v_{y,n} v_{y,k'}^*\} \right. \tag{3-11}$$

$$\left. + \mathrm{E}\{v_{x,m} v_{x,m'}^* v_{x,n'} v_{x,k'}^*\} \mathrm{E}\{v_{y,n}^* v_{y,k}\} + \mathrm{E}\{v_{x,m} v_{x,m'}^*\} \mathrm{E}\{v_{y,n}^* v_{y,k} v_{y,n'} v_{y,k'}^*\} \right]$$

We calculate these expectations according to the formulas given in Appendix 3A, and rewrite the SCI PSD as:

$$G_{\text{SCI},x}(f) = \frac{64}{81} f_0^3 e^{-2\alpha L_s} \sum_{i=-\infty}^{+\infty} \delta(f - if_0) \sum_{m,n,k \in S_i}$$

$$\sum_{m',n',k' \in S_i} \zeta(k,m,n)\zeta^*(k',m',n')$$

$$\cdot \left\{ 2R_s^3 \mathrm{E}^3\{|a_x|^2\} \mathcal{P}_1 \delta_{m-m'} \delta_{n'-n} \delta_{k-k'} \right.$$

$$+ R_s^3 \mathrm{E}\{|a_x|^2\} \mathrm{E}^2\{|a_y|^2\} \mathcal{P}_2 \delta_{m-m'} \delta_{k-k'} \delta_{n'-n}$$

$$+ R_s^2 f_0 \mathrm{E}^3\{|a_x|^2\} \left[\mathrm{E}\{|a_x|^4\} \big/ \mathrm{E}^2\{|a_x|^2\} - 2 \right]$$

$$\cdot \mathcal{P}_1 \left(4\delta_{m-m'} \delta_{k-n+n'-k'} + \delta_{n'-n} \delta_{m+k-m'-k'} \right)$$

$$+ R_s f_0^2 \mathrm{E}^3\{|a_x|^2\} \mathcal{P}_1 \delta_{m-n+k-m'+n'-k'}$$

$$\cdot \left[\mathrm{E}\{|a_x|^6\} \big/ \mathrm{E}^3\{|a_x|^2\} - 9\mathrm{E}\{|a_x|^4\} \big/ \mathrm{E}^2\{|a_x|^2\} + 12 \right]$$

$$+ R_s^2 f_0 \mathrm{E}\{|a_x|^2\} \mathrm{E}^2\{|a_y|^2\} \mathcal{P}_2 \delta_{m-m'} \delta_{k-n+n'-k'}$$

$$\left. \cdot \left[\mathrm{E}\{|a_y|^4\} \big/ \mathrm{E}^2\{|a_y|^2\} - 2 \right] \right\} \tag{3-12}$$

where:

$$\mathcal{P}_1 = s_{\text{CUT},x}(mf_0) s_{\text{CUT},x}^*(nf_0) s_{\text{CUT},x}(kf_0) s_{\text{CUT},x}^*(m'f_0) s_{\text{CUT},x}(n'f_0) s_{\text{CUT},x}^*(k'f_0) \tag{3-13}$$

$$\mathcal{P}_2 = s_{\text{CUT},x}(mf_0) s_{\text{CUT},y}^*(nf_0) s_{\text{CUT},y}(kf_0) s_{\text{CUT},x}^*(m'f_0) s_{\text{CUT},y}(n'f_0) s_{\text{CUT},y}^*(k'f_0) \tag{3-14}$$

If we also assume that,

$$\mathrm{E}\left\{\left|a_x\right|^2\right\}=\mathrm{E}\left\{\left|a_y\right|^2\right\}=\frac{1}{2}\mathrm{E}\left\{\left|a\right|^2\right\} \quad , \quad s_{\mathrm{CUT},x}\left(f\right)=s_{\mathrm{CUT},y}\left(f\right)=s_{\mathrm{CUT}}\left(f\right) \tag{3-15}$$

then we get the simplified expression:

$$
\begin{aligned}
G_{\mathrm{SCI},x}\left(f\right)=&\frac{8}{81}f_0^3 e^{-2\alpha L_s}\mathrm{E}^3\left\{\left|a\right|^2\right\}\sum_{i=-\infty}^{+\infty}\delta\left(f-if_0\right)\\
&\sum_{m,n,k\in\mathrm{S}_i}\sum_{m',n',k'\in\mathrm{S}_i}\zeta\left(k,m,n\right)\zeta^*\left(k',m',n'\right)\\
&\cdot\left\{3R_s^3\mathcal{P}_{\mathrm{CUT}}\delta_{m-m'}\delta_{n'-n}\delta_{k-k'}+\left[\mathrm{E}\left\{\left|a\right|^4\right\}\Big/\mathrm{E}^2\left\{\left|a\right|^2\right\}-2\right]\right.\\
&\cdot R_s^2 f_0\mathcal{P}_{\mathrm{CUT}}\left(5\delta_{m-m'}\delta_{k-n+n'-k'}+\delta_{n'-n}\delta_{m+k-m'-k'}\right)\\
&+R_s f_0^2\mathcal{P}_{\mathrm{CUT}}\delta_{m-n+k-m'+n'-k'}\\
&\left.\cdot\left[\mathrm{E}\left\{\left|a\right|^6\right\}\Big/\mathrm{E}^3\left\{\left|a\right|^2\right\}-9\mathrm{E}\left\{\left|a\right|^4\right\}\Big/\mathrm{E}^2\left\{\left|a\right|^2\right\}+12\right]\right\}
\end{aligned}
\tag{3-16}
$$

where:

$$\mathcal{P}_{\mathrm{CUT}}=s_{\mathrm{CUT}}\left(mf_0\right)s_{\mathrm{CUT}}^*\left(nf_0\right)s_{\mathrm{CUT}}\left(kf_0\right)s_{\mathrm{CUT}}^*\left(m'f_0\right)s_{\mathrm{CUT}}\left(n'f_0\right)s_{\mathrm{CUT}}^*\left(k'f_0\right) \tag{3-17}$$

The contribution on the *y* polarization is identical. Therefore, the total EGN model SCI PSD is:

$$G_{\mathrm{SCI}}\left(f\right)=\mathrm{E}^3\left\{\left|a\right|^2\right\}\left[\chi_1\left(f\right)-\Phi_a\,\chi_2\left(f\right)-\Psi_a\,\chi_3\left(f\right)\right] \tag{3-18}$$

where:

$$\Phi_a=2-\frac{\mathrm{E}\left\{\left|a\right|^4\right\}}{\mathrm{E}^2\left\{\left|a\right|^2\right\}} \quad , \quad \Psi_a=-\frac{\mathrm{E}\left\{\left|a\right|^6\right\}}{\mathrm{E}^3\left\{\left|a\right|^2\right\}}+9\frac{\mathrm{E}\left\{\left|a\right|^4\right\}}{\mathrm{E}^2\left\{\left|a\right|^2\right\}}-12 \tag{3-19}$$

$$
\begin{aligned}
\chi_1\left(f\right)=&\frac{16}{81}f_0^3 e^{-2\alpha L_s}\sum_{i=-\infty}^{+\infty}\delta\left(f-if_0\right)\sum_{m,n,k\in\mathrm{S}_i}\sum_{m',n',k'\in\mathrm{S}_i}\\
&\zeta\left(k,m,n\right)\zeta^*\left(k',m',n'\right)\cdot3R_s^3\mathcal{P}_{\mathrm{CUT}}\delta_{m-m'}\delta_{n'-n}\delta_{k-k'}\\
=&\frac{16}{27}f_0^3 e^{-2\alpha L_s}R_s^3\sum_{i=-\infty}^{+\infty}\delta\left(f-if_0\right)\sum_m\sum_k\left|s_{\mathrm{CUT}}\left(mf_0\right)\right|^2\\
&\left|s_{\mathrm{CUT}}\left(kf_0\right)\right|^2\left|s_{\mathrm{CUT}}\left(\left[m+k-i\right]f_0\right)\right|^2\left|\zeta\left(m,k,i\right)\right|^2
\end{aligned}
\tag{3-20}
$$

$$\chi_2(f) = \frac{16}{81} f_0^3 e^{-2\alpha L_s} \sum_{i=-\infty}^{+\infty} \delta(f - if_0)$$

$$\sum_{m,n,k \in S_i} \sum_{m',n',k' \in S_i} \zeta(k,m,n)\zeta^*(k',m',n')$$

$$\cdot R_s^2 f_0 \mathcal{P}_{\text{CUT}} \left(5\delta_{m-m'}\delta_{k-n+n'-k'} + \delta_{n'-n}\delta_{m+k-m'-k'}\right)$$

$$= \frac{80}{81} f_0^4 e^{-2\alpha L_s} R_s^2 \sum_{i=-\infty}^{+\infty} \delta(f - if_0) \sum_m \sum_k$$

$$\sum_{k'} \left|s_{\text{CUT}}(mf_0)\right|^2 s_{\text{CUT}}(kf_0) s_{\text{CUT}}^*([m+k-i]f_0) \qquad (3\text{-}21)$$

$$s_{\text{CUT}}^*(k'f_0) s_{\text{CUT}}([m+k'-i]f_0) \zeta(m,k,i)\zeta^*(m,k',i)$$

$$+ \frac{16}{81} f_0^4 e^{-2\alpha L_s} R_s^2 \sum_{i=-\infty}^{+\infty} \delta(f - if_0) \sum_m \sum_k$$

$$\sum_{k'} \left|s_{\text{CUT}}([m+k-i]f_0)\right|^2 s_{\text{CUT}}(mf_0) s_{\text{CUT}}(kf_0)$$

$$s_{\text{CUT}}^*(k'f_0) s_{\text{CUT}}^*([m+k-k']f_0) \zeta(m,k,i)\zeta^*(m+k-k',k',i)$$

$$\chi_3(f) = \frac{16}{81} f_0^3 e^{-2\alpha L_s} \sum_{i=-\infty}^{+\infty} \delta(f - if_0) \sum_{m,n,k \in S_i} \sum_{m',n',k' \in S_i}$$

$$\zeta(k,m,n)\zeta^*(k',m',n') \cdot R_s f_0^2 \mathcal{P}_{\text{CUT}} \delta_{m-n+k-m'+n'-k'}$$

$$= \frac{16}{81} f_0^5 e^{-2\alpha L_s} R_s \sum_{i=-\infty}^{+\infty} \delta(f - if_0) \sum_m \sum_k \sum_{m'} \qquad (3\text{-}22)$$

$$\sum_{k'} s_{\text{CUT}}(mf_0) s_{\text{CUT}}^*([m+k-i]f_0) s_{\text{CUT}}(kf_0) s_{\text{CUT}}^*(m'f_0)$$

$$s_{\text{CUT}}([m'+k'-i]f_0) s_{\text{CUT}}^*(k'f_0) \zeta(m,k,i)\zeta^*(m',k',i)$$

If identical spans of same fiber type are assumed, with lumped amplifiers exactly compensating for the loss of each span, the SCI PSD is:

$$G_{\text{SCI}}^{\text{EGN}}(f) = \text{E}^3\left\{|a|^2\right\}\left[\kappa_1(f) - \Phi_a \, \kappa_2(f) - \Psi_a \, \kappa_3(f)\right] \qquad (3\text{-}23)$$

where:

$$\kappa_1(f) = \frac{16}{27} f_0^3 R_s^3 \sum_{i=-\infty}^{+\infty} \delta(f - if_0) \sum_m \sum_k$$

$$\left|s_{\text{CUT}}(mf_0)\right|^2 \left|s_{\text{CUT}}(kf_0)\right|^2 \left|s_{\text{CUT}}([m+k-i]f_0)\right|^2 \left|\mu(m,k,i)\right|^2 \qquad (3\text{-}24)$$

$$\kappa_2(f) = \frac{80}{81} f_0^4 R_s^2 \sum_{i=-\infty}^{+\infty} \delta(f - if_0) \sum_m \sum_k \sum_{k'}$$

$$\left| s_{\text{CUT}}(mf_0) \right|^2 s_{\text{CUT}}(kf_0) s_{\text{CUT}}^*([m+k-i]f_0)$$

$$s_{\text{CUT}}([m+k'-i]f_0) s_{\text{CUT}}^*(k'f_0) \, \mu(m,k,i) \mu^*(m,k',i)$$

$$+ \frac{16}{81} f_0^4 R_s^2 \sum_{i=-\infty}^{+\infty} \delta(f - if_0) \sum_m \sum_k \sum_{k'}$$

$$\left| s_{\text{CUT}}([m+k-i]f_0) \right|^2 s_{\text{CUT}}(mf_0) s_{\text{CUT}}(kf_0)$$

$$s_{\text{CUT}}^*([m+k-k']f_0) s_{\text{CUT}}^*(k'f_0) \, \mu(m,k,i) \mu^*(m+k-k',k',i)$$

(3-25)

$$\kappa_3(f) = \frac{16}{81} f_0^5 R_s \sum_{i=-\infty}^{+\infty} \delta(f - if_0) \sum_m \sum_k \sum_{m'} \sum_{k'}$$

$$s_{\text{CUT}}(mf_0) s_{\text{CUT}}^*([m+k-i]f_0) s_{\text{CUT}}(kf_0) s_{\text{CUT}}^*(m'f_0)$$

$$s_{\text{CUT}}([m'+k'-i]f_0) s_{\text{CUT}}^*(k'f_0) \, \mu(m,k,i) \mu^*(m',k',i)$$

(3-26)

where μ is the "link function", which weighs the generation of NLI and depends only on the link parameters, but not on the characteristics of the launched signal, defined as:

$$\mu(m,k,i) = \zeta(m,k,i) \cdot \nu(m,k,i)$$

(3-27)

with:

$$\nu(m,k,i) = \frac{\sin\left(2\beta_2 \pi^2 f_0^2 (m-i)(k-i) N_s L_s\right)}{\sin\left(2\beta_2 \pi^2 f_0^2 (m-i)(k-i) L_s\right)} e^{j2\beta_2 \pi^2 f_0^2 (m-i)(k-i)(N_s-1)L_s}$$

(3-28)

Letting $f_0 \to 0$, we can then change the discrete-summation formula into integral form:

$$\kappa_1(f) = \frac{16}{27} R_s^3 \int_{-R_s/2}^{+R_s/2} df_1 \int_{-R_s/2}^{+R_s/2} df_2$$

$$\left| s_{\text{CUT}}(f_1) \right|^2 \left| s_{\text{CUT}}(f_2) \right|^2 \left| s_{\text{CUT}}(f_1 + f_2 - f) \right|^2 \left| \mu(f_1, f_2, f) \right|^2$$

(3-29)

$$\kappa_2(f) = \frac{80}{81} R_s^2 \int_{-R_s/2}^{+R_s/2} df_1 \int_{-R_s/2}^{+R_s/2} df_2 \int_{-R_s/2}^{+R_s/2} df_2' \left| s_{\text{CUT}}(f_1) \right|^2 s_{\text{CUT}}(f_2) s_{\text{CUT}}^*(f_2')$$

$$s_{\text{CUT}}^*(f_1 + f_2 - f) s_{\text{CUT}}(f_1 + f_2' - f) \mu(f_1, f_2, f) \mu^*(f_1, f_2', f)$$

$$+ \frac{16}{81} R_s^2 \int_{-R_s/2}^{+R_s/2} df_1 \int_{-R_s/2}^{+R_s/2} df_2 \int_{-R_s/2}^{+R_s/2} df_2' \left| s_{\text{CUT}}(f_1 + f_2 - f) \right|^2 s_{\text{CUT}}(f_1)$$

$$s_{\text{CUT}}(f_2) s_{\text{CUT}}^*(f_1 + f_2 - f_2') s_{\text{CUT}}^*(f_2') \mu(f_1, f_2, f) \mu^*(f_1 + f_2 - f_2', f_2', f)$$

(3-30)

$$\kappa_3(f) = \frac{16}{81} R_s \int\limits_{-R_s/2}^{+R_s/2} df_1 \int\limits_{-R_s/2}^{+R_s/2} df_2 \int\limits_{-R_s/2}^{+R_s/2} df_1' \int\limits_{-R_s/2}^{+R_s/2} df_2'$$

$$s_{\mathrm{CUT}}(f_1) s_{\mathrm{CUT}}(f_2) s_{\mathrm{CUT}}^*(f_1 + f_2 - f) s_{\mathrm{CUT}}^*(f_1') \qquad (3\text{-}31)$$

$$s_{\mathrm{CUT}}^*(f_2') s_{\mathrm{CUT}}(f_1' + f_2' - f) \mu(f_1, f_2, f) \mu^*(f_1', f_2', f)$$

where the link function is,

$$\mu(f_1, f_2, f) = \zeta(f_1, f_2, f) \cdot \nu(f_1, f_2, f) \qquad (3\text{-}32)$$

with:

$$\zeta(f_1, f_2, f) = \gamma \frac{1 - e^{-2\alpha L_s} e^{j4\pi^2 \beta_2 (f_1 - f)(f_2 - f) L_s}}{2\alpha - j4\pi^2 \beta_2 (f_1 - f)(f_2 - f)} \qquad (3\text{-}33)$$

$$\nu(f_1, f_2, f) = e^{j2\beta_2 \pi^2 (f_1 - f)(f_2 - f)(N_s - 1) L_s} \cdot$$
$$\frac{\sin\left(2\beta_2 \pi^2 (f_1 - f)(f_2 - f) N_s L_s\right)}{\sin\left(2\beta_2 \pi^2 (f_1 - f)(f_2 - f) L_s\right)} \qquad (3\text{-}34)$$

The $\zeta(f_1, f_2, f)$ factor physically represents the efficiency of non-degenerate FWM occurring among three spectral components of the signal placed at frequencies $f_1, f_2,$ $f_3 = (f_1 + f_2 - f)$, producing a beat disturbance at frequency f. The factor ν relates to the coherent interference of NLI field contributions produced in different spans, when they are summed up at the receiver location.

If distributed amplification or non-identical spans are present in the link, the formulas shown in this chapter are still valid, provided that the link function μ is suitably modified. These generalizations will not be dealt with in this thesis.

The term related to $\kappa_1(f)$ in Eq. (3-37) accounts for the GN model component, that is: $G_{\mathrm{SCI}}^{\mathrm{GN}}(f) = P_{\mathrm{SCI}}^3 \kappa_1(f)$. The other two terms are corrections that take signal non-Gaussianity into account, that is: $G_{\mathrm{SCI}}^{\mathrm{corr}}(f) = P_{\mathrm{SCI}}^3 \left[\Phi_a \kappa_2(f) + \Psi_a \kappa_3(f) \right]$. The overall resulting corrected model $G_{\mathrm{SCI}}^{\mathrm{EGN}}(f)$ is the EGN model. Note the need to include both a 4th and a 6th-order moment of the transmitted symbol sequence, the latter appearing in the coefficient Ψ_a. The values of Φ_a and Ψ_a depend only on the chosen format. In Table 3-1 we report them for the most common QAM constellations. It shows that more complex formats have smaller values of Φ_a and Ψ_a. As a result, they have a smaller correction $G_{\mathrm{SCI}}^{\mathrm{corr}}(f)$ vs. the GN model component $G_{\mathrm{SCI}}^{\mathrm{GN}}(f)$. This is also the case with XCI and MCI (Sects. 3.1.2 and 3.1.3).

Table 3-1: Values of Φ_a and Ψ_a

Format	Φ_a	Ψ_a
PM-BPSK	1	-4
PM-QPSK	1	-4
PM-16QAM	17/25	-52/25
PM-64QAM	13/21	-1161/646
PM-∞-QAM	3/5	-12/7
PM-Gaussian	0	0

In Fig. 3-2(a)-(c) we show the result of the SCI calculation vs. simulations. Details about the simulation technique can be found in [38], where similar simulations were carried out. The simulated data length amounted to 300,000 symbols, a number that was used for all NLI span-by-span accumulation plots in this chapter. We looked at the SCI normalized average power η_{SCI} defined as follows:

$$\eta_{\mathrm{SCI}} = P_{\mathrm{CUT}}^{-3} \int_{-R_s/2}^{R_s/2} G_{\mathrm{SCI}}^{\mathrm{EGN}}(f)\, df \qquad (3\text{-}35)$$

This parameter collects the total SCI noise spectrally located over the CUT, normalized through P_{CUT}^{-3} so that η_{SCI} itself does not depend on launch power. The simulated system data are as follows:

- single channel PM-QPSK at R_s =32 GBaud;
- raised-cosine power spectrum with roll-off parameter 0.05;
- SMF with D =16.7 ps/(nm km), γ =1.3 1/(W km), α_{dB} =0.22 dB/km;
- NZDSF with D =3.8 ps/(nm km), γ =1.5 1/(W km), α_{dB} =0.22 dB/km;
- LS fiber with D =-1.8 ps/(nm km), γ =2.2 1/(W km), α_{dB} =0.22 dB/km;
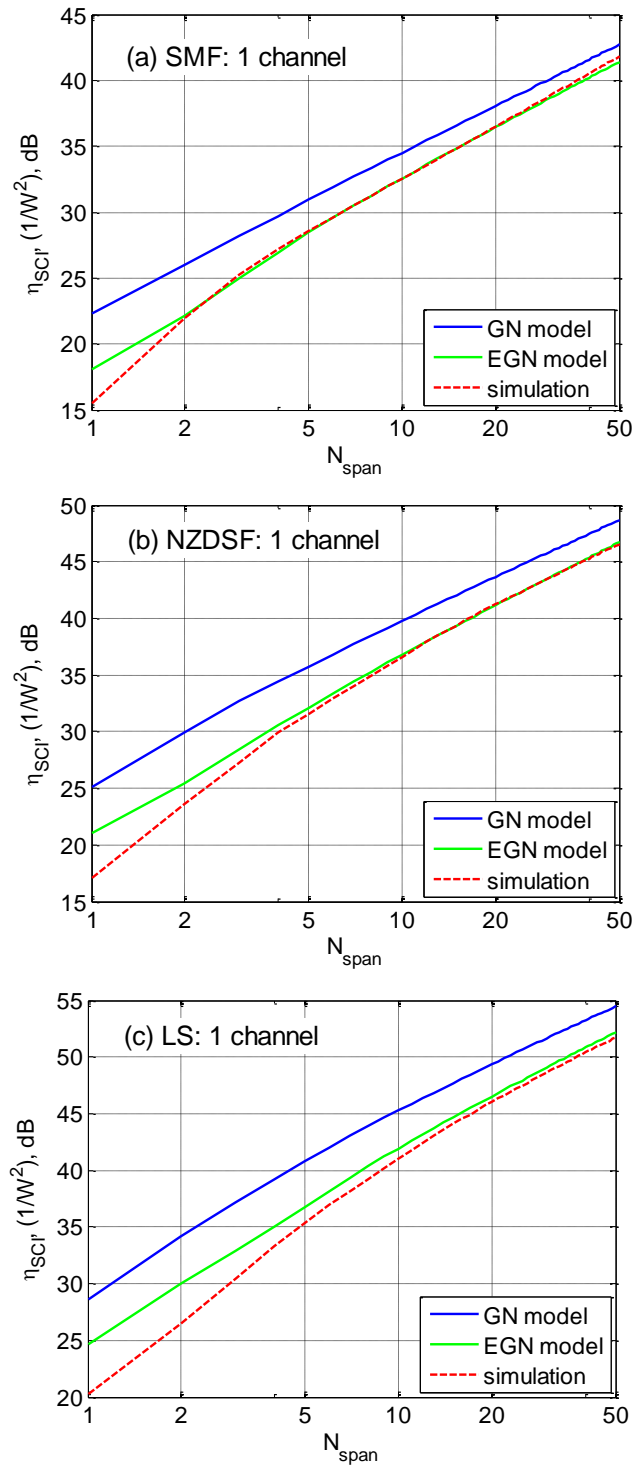- span length L_s =100 km.

Fig. 3-2: Plot of normalized SCI η_{SCI}, vs. number of spans in the link, assuming a single PM-QPSK channel over SMF, NZDSF and LS, with span length 100 km. Red dashed line: simulation. Blue solid line: the GN model. Green solid line: the EGN model (Eq. (3-23)).

Note that we chose not to use ideally rectangular spectra, to avoid possible numerical problems due to the truncation of excessively long, slowly decaying signal pulses. The selected roll-off value is very small and nonlinearity generation can be expected not to differ significantly from that of an ideal rectangular spectrum. We choose PM-QPSK as modulation format to maximize the correction $G_{\mathrm{SCI}}^{\mathrm{corr}}(f)$ vs. the GN model term $G_{\mathrm{SCI}}^{\mathrm{GN}}(f)$, according to Table 3-1. The same format is used, for the same reason, for the investigation of XCI and MCI span-by-span accumulation, shown in Sects. 3.1.2 and 3.1.3.

The plots in Fig. 3-2 show that Eq. (3-23) has good accuracy, as soon as there is some substantial accumulated dispersion. The gap between analytical and simulative results in the first few spans is currently being investigated. Beyond the first few spans, the agreement is excellent for SMF and NZDSF and still rather good for the challenging, very low-dispersion LS fiber. The overall accuracy improvement over the GN model is very substantial.

Note also that the difference between either simulation or the EGN model, vs. the GN model (blue line) tends to close up for large number of spans. At 50 spans the residual gap is 1.1 dB for SMF. It is however more significant for the lower-dispersion fibers: 2.1 dB for NZDSF and 2.8 dB for LS.

3.1.2 Cross-channel interference

A key aspect of XCI is that the individual contributions of each single INT channel in the WDM comb simply add up. As a result, one can concentrate on analytically finding the XCI due to a single INT channel. Then, the total XCI is the sum of the formally identical, albeit quantitatively different, contributions of each of the INT channels present in the WDM comb. In other words, the total PSD of XCI on the CUT is the sum of the PSDs generated due to each INT.

3.1.2.1 The XPM approximation to XCI

We started out from the formula provided in [30] in summation form, which the authors define as "XPM". We re-wrote it in integral dual-polarization form and in such a way as to make it represent the NLI PSD emerging at a generic frequency f within the CUT. It is:

$$G_{\text{XPM}}(f) = P_{\text{CUT}} P_{\text{INT}}^2 \left[\kappa_{11}(f) - \Phi_b \, \kappa_{12}(f) \right] \tag{3-36}$$

where:

$$\Phi_b = 2 - \frac{\text{E}\left\{|b|^4\right\}}{\text{E}^2\left\{|b|^2\right\}} \tag{3-37}$$

$$\kappa_{11}(f) = \frac{32}{27} R_s^3 \int_{-R_s/2}^{+R_s/2} df_1 \int_{\Delta f - R_s/2}^{\Delta f + R_s/2} df_2 \left| s_{\text{CUT}}(f_1) \right|^2$$
$$\left| s_{\text{INT}}(f_2) \right|^2 \left| s_{\text{INT}}(f_1 + f_2 - f) \right|^2 \left| \mu(f_1, f_2, f) \right|^2 \tag{3-38}$$

$$\kappa_{12}(f) = \frac{80}{81} R_s^2 \int_{-R_s/2}^{+R_s/2} df_1 \int_{\Delta f - R_s/2}^{\Delta f + R_s/2} df_2 \int_{\Delta f - R_s/2}^{\Delta f + R_s/2} df_2'$$
$$\left| s_{\text{CUT}}(f_1) \right|^2 s_{\text{INT}}(f_2) s_{\text{INT}}^*(f_2') s_{\text{INT}}^*(f_1 + f_2 - f)$$
$$s_{\text{INT}}(f_1 + f_2' - f) \mu(f_1, f_2, f) \mu^*(f_1, f_2', f) \tag{3-39}$$

where Δf is the channel spacing.

As argued in [30], the $\kappa_{11}(f)$ term corresponds to a GN-model-like contribution, that is, it assumes signal Gaussianity. Instead, $\kappa_{12}(f)$ represents a correction that takes into account the non-Gaussianity of the transmitted signal. As said, these formulas account for a single INT channel. Considering a WDM system, the same calculations shown above must be repeated for each INT channel and the results summed together.

Note that in [30] XPM is not proposed as a partial contribution to NLI, but as an overall NLI estimator, accurate enough to represent the whole nonlinearity affecting the CUT (excluding SCI). In the next subsection we will discuss this claim.

3.1.2.2   The overall XCI

Equation (3-36), derived from [30], neglects various XCI contributions arising when the INT channel is directly adjacent to the CUT. To provide a graphical intuitive description of what is left out, in Fig. 3-3 we show a plot of the domains in the $[f_1, f_2]$ plane where integration takes place for the $\kappa_{11}(f)$ and $\kappa_{12}(f)$ contributions. The reason why it is possible to discuss the integration domain of $\kappa_{12}(f)$ on the plane $[f_1, f_2]$, despite the fact that $\kappa_{12}(f)$ involves integration over three variables: f_1, f_2, f_2', is that each point of the $[f_1, f_2]$ plane represents a triple of frequencies, namely (f_1, f_2, f_3), that produce a

"FWM" beat at frequency f . They obey the fixed relation $f_3 = f_1 + f_2 - f$. The "elementary" NLI contributions, that are then integrated in the EGN formulas to provide the total NLI, arise each from two triples: (f_1, f_2, f_3) and (f_1', f_2', f_3'), both producing a FWM contribution at the same frequency $f = (f_1 + f_2 - f_3) = (f_1' + f_2' - f_3')$. There are other constraints that relate the pairs of triples, which depend on the statistical features of the signal. It turns out that all different NLI contributions can be fully categorized just based on properly dividing the $[f_1, f_2]$ plane into integration regions where the (f_1, f_2, f_3) triples are located. This is because, if the subdivision is done correctly, the (f_1', f_2', f_3') triples that interact with each (f_1, f_2, f_3) triple, for a specific type of NLI, are bound to originate from the same region of the $[f_1', f_2']$ plane as that of the $[f_1, f_2]$ plane where (f_1, f_2, f_3) originates. In other words, discussing the integration regions in $[f_1, f_2]$ is enough, because for each region in the $[f_1, f_2]$ plane the relevant region in the $[f_1', f_2']$ plane is the same, in a one-to-one correspondence.
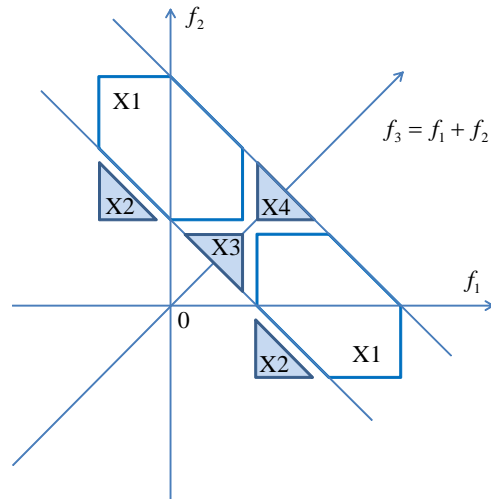

Fig. 3-3: Integration regions to obtain the power spectrum of XCI , $G_{\mathrm{XCI}}^{\mathrm{GN}}(f)$, at $f = 0$ (i.e., at the center of CUT), due to a single adjacent INT channel, assuming that its center frequency is slightly higher than the symbol rate. The XPM approximation [30] of Eq. (3-36) considers the X1 regions only. The full XCI formula of Eq. (3-40) accounts for all X1-X4 regions.

The example of Fig. 3-3 considers XCI due to a single INT channel adjacent to the CUT, placed at higher frequency than the CUT, and assumes $f = 0$. The XPM formulas reported in [30], and hence Eq. (3-36), take into account the two X1 domains only. They neglect X2, X3 and X4. The complete XCI formulas that take all regions X1-X4 into account, are:

$$
\begin{aligned}
G_{\mathrm{XCI}}^{\mathrm{EGN}}\left(f\right) = {} & P_{\mathrm{CUT}}P_{\mathrm{INT}}^2\left[\kappa_{11}\left(f\right) - \Phi_b\,\kappa_{12}\left(f\right)\right] + \\
& P_{\mathrm{CUT}}^2 P_{\mathrm{INT}}\left[\kappa_{21}\left(f\right) - \Phi_a\,\kappa_{22}\left(f\right)\right] + \\
& P_{\mathrm{CUT}}^2 P_{\mathrm{INT}}\left[\kappa_{31}\left(f\right) - \Phi_a\,\kappa_{32}\left(f\right)\right] + \\
& P_{\mathrm{INT}}^3\left[\kappa_{41}\left(f\right) - \Phi_b\,\kappa_{42}\left(f\right) - \Psi_b\,\kappa_{43}\left(f\right)\right]
\end{aligned}
\tag{3-40}
$$

where:

$$
\Psi_b = -\frac{\mathrm{E}\left\{|b|^6\right\}}{\mathrm{E}^3\left\{|b|^2\right\}} + 9\,\frac{\mathrm{E}\left\{|b|^4\right\}}{\mathrm{E}^2\left\{|b|^2\right\}} - 12
\tag{3-41}
$$

$$
\begin{aligned}
\kappa_{21}\left(f\right) = {} & \frac{32}{27}R_s^3 \int_{\Delta f - R_s/2}^{\Delta f + R_s/2} df_1 \int_{-R_s/2}^{+R_s/2} df_2 \left|s_{\mathrm{INT}}\left(f_1\right)\right|^2 \\
& \left|s_{\mathrm{CUT}}\left(f_2\right)\right|^2 \left|s_{\mathrm{CUT}}\left(f_1 + f_2 - f\right)\right|^2 \left|\mu\left(f_1, f_2, f\right)\right|^2
\end{aligned}
\tag{3-42}
$$

$$
\begin{aligned}
\kappa_{22}\left(f\right) = {} & \frac{80}{81}R_s^2 \int_{\Delta f - R_s/2}^{\Delta f + R_s/2} df_1 \int_{-R_s/2}^{+R_s/2} df_2 \int_{-R_s/2}^{+R_s/2} df_2' \\
& \left|s_{\mathrm{INT}}\left(f_1\right)\right|^2 s_{\mathrm{CUT}}\left(f_2\right) s_{\mathrm{CUT}}^*\left(f_2'\right) s_{\mathrm{CUT}}^*\left(f_1 + f_2 - f\right) \\
& s_{\mathrm{CUT}}\left(f_1 + f_2' - f\right) \mu\left(f_1, f_2, f\right) \mu^*\left(f_1, f_2', f\right)
\end{aligned}
\tag{3-43}
$$

$$
\begin{aligned}
\kappa_{31}\left(f\right) = {} & \frac{16}{27}R_s^3 \int_{-R_s/2}^{+R_s/2} df_1 \int_{-R_s/2}^{+R_s/2} df_2 \left|s_{\mathrm{CUT}}\left(f_1\right)\right|^2 \\
& \left|s_{\mathrm{CUT}}\left(f_2\right)\right|^2 \left|s_{\mathrm{INT}}\left(f_1 + f_2 - f\right)\right|^2 \left|\mu\left(f_1, f_2, f\right)\right|^2
\end{aligned}
\tag{3-44}
$$

$$
\begin{aligned}
\kappa_{32}\left(f\right) = {} & \frac{16}{81}R_s^2 \int_{-R_s/2}^{+R_s/2} df_1 \int_{-R_s/2}^{+R_s/2} df_2 \int_{-R_s/2}^{+R_s/2} df_2' \\
& \left|s_{\mathrm{INT}}\left(f_1 + f_2 - f\right)\right|^2 s_{\mathrm{CUT}}\left(f_1\right) s_{\mathrm{CUT}}\left(f_2\right) s_{\mathrm{CUT}}^*\left(f_2'\right) \\
& s_{\mathrm{CUT}}^*\left(f_1 + f_2 - f_2'\right) \mu\left(f_1, f_2, f\right) \mu^*\left(f_1 + f_2 - f_2', f_2', f\right)
\end{aligned}
\tag{3-45}
$$

$$
\begin{aligned}
\kappa_{41}\left(f\right) = {} & \frac{16}{27}R_s^3 \int_{\Delta f - R_s/2}^{\Delta f + R_s/2} df_1 \int_{\Delta f - R_s/2}^{\Delta f + R_s/2} df_2 \left|s_{\mathrm{INT}}\left(f_1\right)\right|^2 \\
& \left|s_{\mathrm{INT}}\left(f_2\right)\right|^2 \left|s_{\mathrm{INT}}\left(f_1 + f_2 - f\right)\right|^2 \left|\mu\left(f_1, f_2, f\right)\right|^2
\end{aligned}
\tag{3-46}
$$

$$
\kappa_{42}(f) = \frac{80}{81}R_s^2 \int\limits_{\Delta f - R_s/2}^{\Delta f + R_s/2} df_1 \int\limits_{\Delta f - R_s/2}^{\Delta f + R_s/2} df_2 \int\limits_{\Delta f - R_s/2}^{\Delta f + R_s/2} df_2'
$$

$$
\left| s_{INT}(f_1) \right|^2 s_{INT}(f_2) s_{INT}^*(f_2') s_{INT}^*(f_1 + f_2 - f)
$$

$$
s_{INT}(f_1 + f_2' - f)\mu(f_1, f_2, f)\mu^*(f_1, f_2', f)
$$

$$
+ \frac{16}{81}R_s^2 \int\limits_{\Delta f - R_s/2}^{\Delta f + R_s/2} df_1 \int\limits_{\Delta f - R_s/2}^{\Delta f + R_s/2} df_2 \int\limits_{\Delta f - R_s/2}^{\Delta f + R_s/2} df_2'
$$

$$
\left| s_{INT}(f_1 + f_2 - f) \right|^2 s_{INT}(f_1) s_{INT}(f_2) s_{INT}^*(f_2')
$$

$$
s_{INT}^*(f_1 + f_2 - f_2')\mu(f_1, f_2, f)\mu^*(f_1 + f_2 - f_2', f_2', f)
$$

(3-47)

$$
\kappa_{43}(f) = \frac{16}{81}R_s \int\limits_{\Delta f - R_s/2}^{\Delta f + R_s/2} df_1 \int\limits_{\Delta f - R_s/2}^{\Delta f + R_s/2} df_2 \int\limits_{\Delta f - R_s/2}^{\Delta f + R_s/2} df_1' \int\limits_{\Delta f - R_s/2}^{\Delta f + R_s/2} df_2'
$$

$$
s_{INT}(f_1) s_{INT}(f_2) s_{INT}^*(f_1 + f_2 - f) s_{INT}^*(f_1')
$$

$$
s_{INT}^*(f_2') s_{INT}(f_1' + f_2' - f))\mu(f_1, f_2, f)\mu^*(f_1', f_2', f)
$$

(3-48)

The GN model part of XCI, $G_{XCI}^{GN}(f)$, stems from the $\kappa_{m1}(f)$ functions, with m=1,2,3,4. All other functions generate the correction part $G_{XCI}^{corr}(f)$. The overall resulting corrected model $G_{XCI}^{EGN}(f)$ is the EGN model. Their derivation can be found in Appendix 3B. Similar to the SCI formula, when the correction contributions are addressed, both 4th order (Φ_a and Φ_b) and 6th order (Ψ_b) moments of the transmitted symbol sequences must be considered, whereas in the XPM approximation only 4th order moments are involved.

Note the important circumstance that the XCI domains X2-X4 are non-empty as long as the INT channel adjacent to the CUT is not too far from the CUT, depending on the value of both f and $|\Delta f|$. All three regions X2-X4 completely disappear when $|\Delta f| \geq 2R_s$, for any value of f in the CUT band. This is automatically accounted for in Eq. (3-40), which can hence be considered a generalized complete formula for XCI, valid for channels adjacent to the CUT but also for non-adjacent channels, placed at any frequency distance from the CUT.

Even though the extra XCI X2-X4 regions appear only for the two channels adjacent to the CUT, they may contribute substantially to the overall NLI variance, depending on link and system parameters, so that disregarding them may lead to non-negligible error. This is due to the fact that these regions are relatively close to the origin of the $[f_1, f_2]$,

where the μ integrand factors are maximum (see [17] for more details).

We investigated this matter by looking at the XCI normalized variance η_{XCI} defined as follows:

$$\eta_{\text{XCI}} = P_{\text{ch}}^{-3} \int\limits_{-R_s/2}^{R_s/2} G_{\text{XCI}}^{\text{EGN}}(f) df \tag{3-49}$$

with $G_{\text{XCI}}(f)$ given by Eq. (3-40). This parameter collects the total XCI noise spectrally located over the CUT, normalized so that η_{XCI} itself does not depend on launch power. Note that for simplicity we assume here:

$$P_{\text{ch}} = P_{\text{INT}} = P_{\text{CUT}} \tag{3-50}$$

We calculated η_{XCI} for the same system addressed in Sect. 3.1.1 for SCI. The only difference is that now the system has 3 channels, with the CUT as the center channel. The channel spacing is 33.6 GHz. For the same system we also calculated η_{XPM}, defined as:

$$\eta_{\text{XPM}} = P_{\text{ch}}^{-3} \int\limits_{-R_s/2}^{R_s/2} G_{\text{XPM}}(f) df \tag{3-51}$$

with $G_{\text{XPM}}(f)$ given by Eq. (3-36).

Finally, still for the same system, we simulatively estimated the overall nonlinearity, with single-channel effects removed. We did this because we wanted to see whether either XPM, or XCI, could be considered good approximations to the overall NLI produced in the link, once SCI is taken out. To remove SCI from the simulation results, we simulated both the CUT alone and the CUT with the two INT channels. Then we subtracted the former simulation result from the latter at the field level, thus ideally freeing the CUT completely from single-channel effects while leaving in all other non-linearity (XCI and MCI).

Fig. 3-4(a) shows the XPM approximation η_{XPM} of [30] provided by Eq. (3-51) as a magenta solid line. The green solid line represents η_{XCI} given by the EGN model Eq. (3-49). The red dashed curve represents the simulation result accounting for all NLI except SCI. All curves are represented as a function of the number of spans, up to 50.

This may seem a large number of spans but the reach of the simulated system, assuming SMF, conventional EDFA amplification with realistic noise figure (5-6 dB)

and a realistic FEC BER threshold of about 10^{-2}, is indeed on the order of 50 spans. The figure shows that in this specific scenario the XPM approximation η_{XPM} of [30] underestimates the simulated NLI by about 1.4 dB. XCI η_{XCI} reduces such error to less than 0.4 dB throughout the plot. The GN model starts out with a large 5 dB overestimation error, which gradually tapers down to about 1.3 dB at 50 spans.

In Fig. 3-4(b), we show a similar plot, this time for NZDSF. Above 5 spans, η_{XPM} of Eq. (3-51) underestimates NLI by about 2 dB whereas the GN model overestimates it by about the same amount. These gaps are substantially wider than in the SMF case. Interestingly, a 0.8 dB gap is now also present between the simulation results and η_{XCI}. This suggests that some NLI contributions are missing, i.e., the XCI component is not sufficiently representative of the overall NLI (excluding SCI).

A similar situation is also seen in Fig. 3-4(c), for the very low-dispersion scenario of LS fiber, with the interesting aspect that both XPM and XCI show a substantial underestimation error (1.7 and 1.3 dB, respectively) for a large number of spans. The GN model clearly does not cope well with ultra-low dispersion fibers, showing a wide overestimation error of about 3.2 dB across all spans.

In conclusion, Fig. 3-4 shows that the XCI component of NLI may be sufficiently representative of all NLI (excluding SCI) only over high-dispersion fibers. On low-dispersion fibers part of NLI is clearly missing. In these specific examples, XPM is not representative of all NLI and not even of XCI alone.

These results compellingly suggest that a complete model for NLI must include MCI as well. We introduce it in the next section. As a last remark, we point out that for larger values of the channel spacing $|\Delta f|$, a smaller gap can be expected between simulations and XPM, especially over SMF. Also, for $|\Delta f| \geq 2R_s$ XPM and XCI would coincide due to the vanishing of the X2-X4 regions.
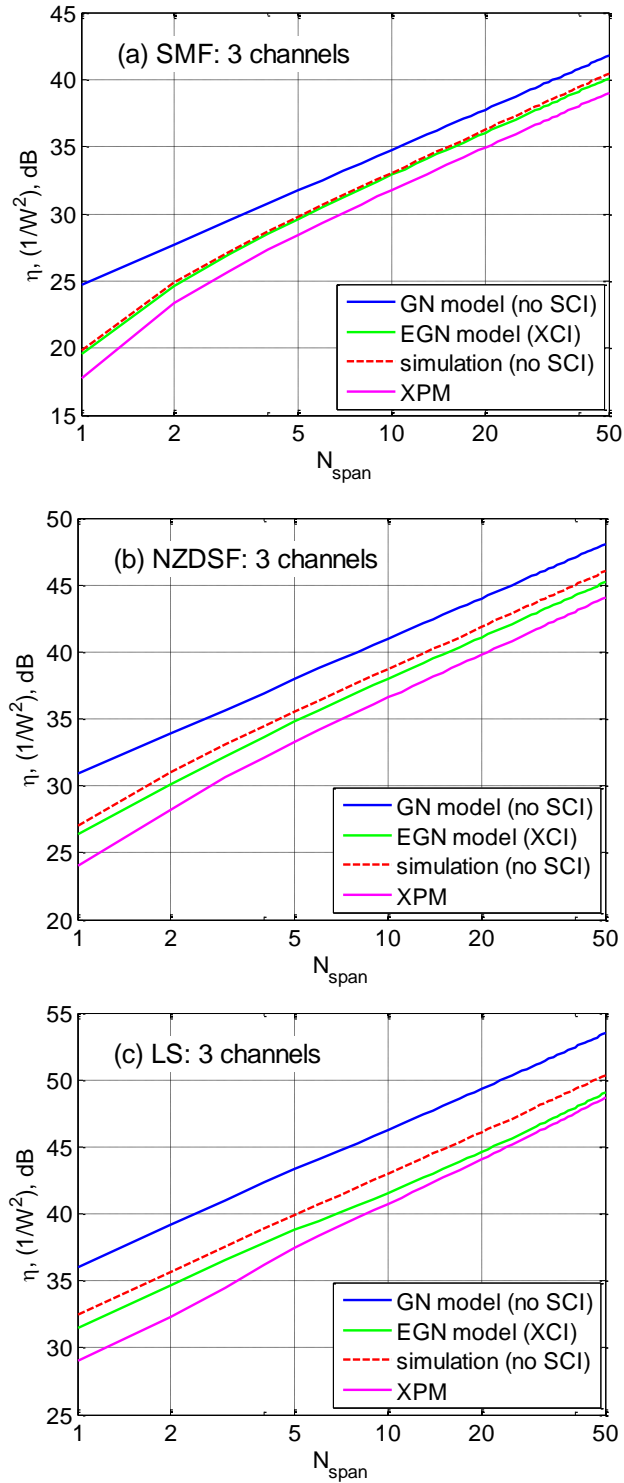
Fig. 3-4: Plot of normalized nonlinearity coefficient η vs. number of spans in the link, assuming 3 PM-QPSK channels over SMF, NZDSF and LS, with span length 100 km. The CUT is the center channel. The spacing is 1.05 times the symbol rate. Red dashed line: simulation, with SCI removed. Blue solid line: the GN model without SCI. Magenta solid line: the XPM approximation η_{XPM} of [30] (Eq. (3-51) here). Green solid line: η_{XCI} estimated through the EGN model (Eq. (3-49)).

3.1.3 Multi-channel interference

MCI can be thought of as typically being weaker than either SCI or XCI, because it arises on regions of the $[f_1, f_2]$ plane where the link function μ has a smaller magnitude than over the regions generating XCI and SCI. To provide an intuitive pictorial description of this circumstance, we show in Fig. 3-5 the integration regions arising in the plane $[f_1, f_2]$ when calculating the overall NLI PSD at the center of the CUT, i.e., $G_{\mathrm{NLI}}(0)$, for a three-channel example similar to the test PM-QPSK system of the previous section. The center region is SCI, the blue regions are XCI and the pink/red ones are MCI. Each point in these regions contributes to NLI, but it is weighed through the factors μ appearing in the integrals. These factors peak at the origin and along the $[f_1, f_2]$ plane axes. The larger the fiber dispersion is, the faster the decay of the μ factors away from such maxima. However, when dispersion is relatively low, such as with TrueWave RS or LS fibers, the decay of μ is much slower and MCI is not negligible, as the results of the previous section suggest.

Note also that when $G_{\mathrm{NLI}}(f)$ is evaluated at a frequency f which is different than 0, the overall picture changes quite significantly. In particular, for $f \approx \pm R_s/2$ (values that correspond to the cut-off edges for a filter matched to a pulse $s_{\mathrm{CUT}}(f)$ with rectangular spectrum) some of the MCI integration regions come close to where the μ's are at their maxima. This case is exemplified in Fig. 3-6, which depicts the integration regions for $f = R_s/2$. The lower M0 and especially the lower M1 region are next to the μ's maxima, whose location has shifted away from the $[f_1, f_2]$ axes and now occurs at the red dashed axes. In this situation, MCI may therefore contribute substantially.

The MCI formulas for the red regions of Fig. 3-5 and Fig. 3-6 are:

$$G_{\mathrm{MCI}}^{\mathrm{EGN}}(f) = P_{\mathrm{CUT}} P_{\mathrm{INT,1}} P_{\mathrm{INT,-1}} \kappa_{\mathrm{M0}}(f) + P_{\mathrm{INT,1}}^2 P_{\mathrm{INT,-1}} \left[\kappa_{\mathrm{M1,1}}(f) - \Phi_b \, \kappa_{\mathrm{M1,2}}(f) \right] \quad (3\text{-}52)$$

where:

$$\kappa_{\mathrm{M0}}(f) = 2 \cdot \frac{16}{27} R_s^3 \int_{\Delta f - R_s/2}^{\Delta f + R_s/2} df_1 \int_{-\Delta f - R_s/2}^{-\Delta f + R_s/2} df_2 \left| s_{\mathrm{INT_1}}(f_1) \right|^2$$
$$\left| s_{\mathrm{INT_1}}(f_2) \right|^2 \left| s_{\mathrm{CUT}}(f_1 + f_2 - f) \right|^2 \left| \mu(f_1, f_2, f) \right|^2 \quad (3\text{-}53)$$

$$\kappa_{\text{M1,1}}(f) = 4 \cdot \frac{16}{27} R_s^3 \int\limits_{-\Delta f - R_s/2}^{-\Delta f + R_s/2} df_1 \int\limits_{\Delta f - R_s/2}^{\Delta f + R_s/2} df_2 \left| s_{\text{INT}_{-1}}(f_1) \right|^2$$

$$\left| s_{\text{INT}_1}(f_2) \right|^2 \left| s_{\text{INT}_1}(f_1 + f_2 - f) \right|^2 \left| \mu(f_1, f_2, f) \right|^2 \tag{3-54}$$

$$\kappa_{\text{M1,2}}(f) = 2 \cdot \frac{80}{81} R_s^2 \int\limits_{-\Delta f - R_s/2}^{-\Delta f + R_s/2} df_1 \int\limits_{\Delta f - R_s/2}^{\Delta f + R_s/2} df_2 \int\limits_{\Delta f - R_s/2}^{\Delta f + R_s/2} df_2'$$

$$\left| s_{\text{INT}_{-1}}(f_1) \right|^2 s_{\text{INT}_1}(f_2) s_{\text{INT}_1}^*(f_2') s_{\text{INT}_1}^*(f_1 + f_2 - f) \tag{3-55}$$

$$s_{\text{INT}_1}(f_1 + f_2' - f) \mu(f_1, f_2, f) \mu^*(f_1, f_2', f)$$

The subscripts "INT$_{-1}$" and "INT$_1$" refer to the INT channel spectrally located, respectively, to the left (lower frequency) and to the right (higher frequency) of the CUT.

Interestingly, in the pink region M0, NLI is produced entirely according to the GN model, through κ_{M0}. No correction term for signal non-Gaussian distribution is present there. In the red region M1, the induced MCI has instead a similar structure as XCI in the blue region X1. In particular, both a GN-model-like term $\kappa_{\text{M1,1}}$ and a correction term $\kappa_{\text{M1,2}}$ are present.
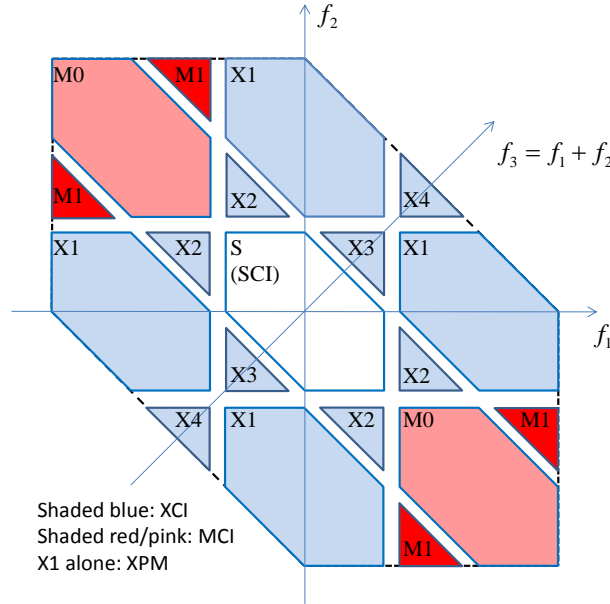

Fig. 3-5: Integration regions in the $[f_1, f_2]$ plane needed to obtain the power spectrum of NLI for f =0, due to 2 adjacent INT channels with spacing slightly higher than the symbol rate. The full XCI formula of Eq. (3-49) accounts for all X1-X4 regions. The XPM [30] (Eq. (3-51)) considers the X1 regions only. SCI is the center region. MCI is the red/pink regions. The M0 region has only the GN model term, the M1 ones have both the GN model term and non-Gaussianity correction terms.
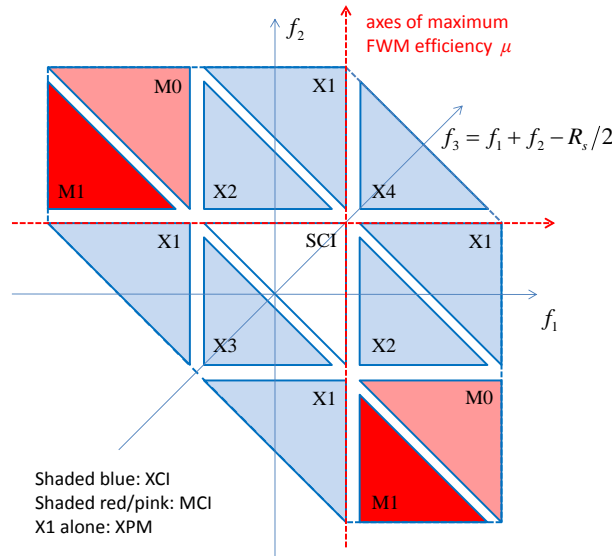
Fig. 3-6: Integration regions in the $[f_1, f_2]$ plane needed to obtain the power spectrum of NLI for $f = R_s/2$, due to 2 adjacent INT channels with spacing slightly higher than the symbol rate. Notice that all regions change shape vs. Fig. 3-5. Also, the maximum FWM efficiency now falls on the translated red-dashed axes, which do not coincide with the $[f_1, f_2]$ axes. The lower M0 and M1 MCI regions are now close to such maxima.

For the same system set-ups addressed in Sect. 3.1.2.2 we calculated η_{MCI}, defined as:

$$\eta_{\text{MCI}} = P_{\text{ch}}^{-3} \int\limits_{-R_s/2}^{R_s/2} G_{\text{MCI}}^{\text{EGN}}(f)df \tag{3-56}$$

with $G_{\text{MCI}}^{\text{EGN}}(f)$ given by Eq. (3-52). We then summed together the XCI and MCI contributions. We call the result "XMCI" for brevity:

$$\eta_{\text{XMCI}} = \eta_{\text{XCI}} + \eta_{\text{MCI}} \tag{3-57}$$

where η_{XCI} is given by Eq. (3-49). The quantity η_{XMCI} is the green solid line in Fig. 3-7. All curves except the green solid one are the same as in Fig. 3-4. Comparing the two sets of figures, we see that the gap that existed between XCI and simulations has now completely disappeared. The gap was therefore due to the missing MCI contributions. The accuracy of the EGN model in estimating η_{XMCI} is remarkable, for both SMF and NZDSF. A small error shows up for LS in the first few spans, which completely disappears along the link.
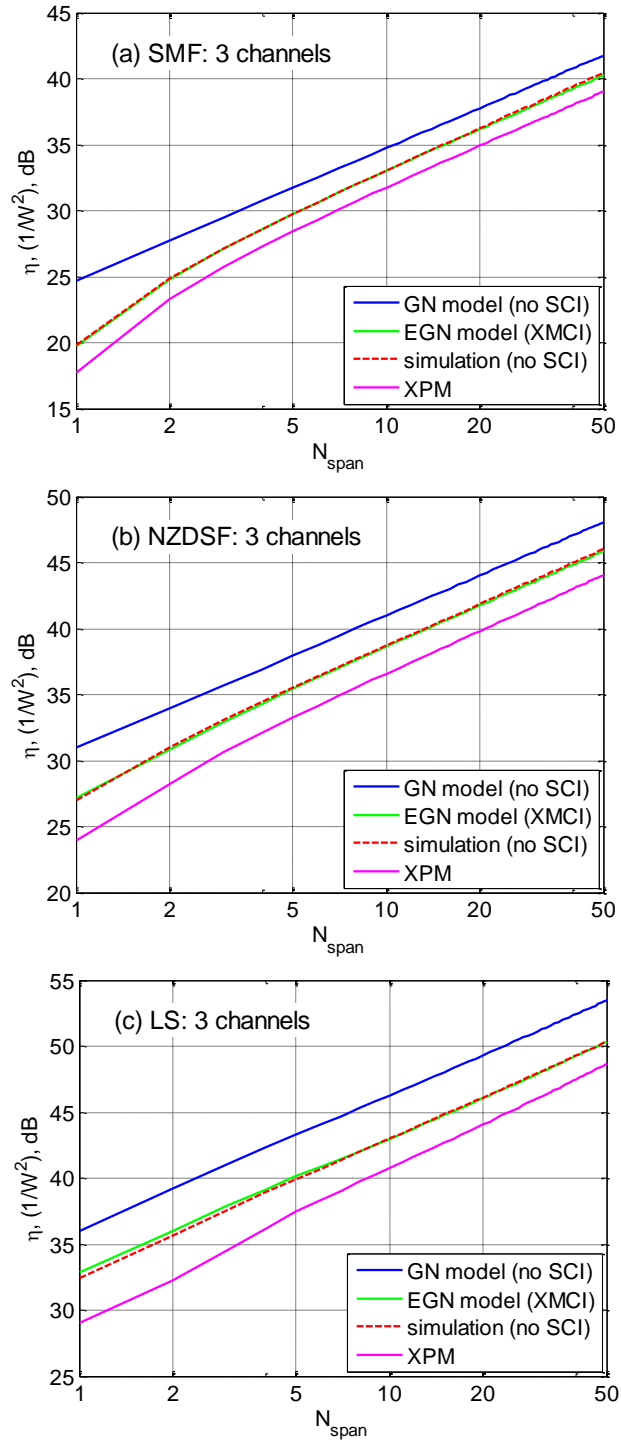
Fig. 3-7: Plot of normalized nonlinearity coefficient η vs. number of spans in the link, assuming 3 PM-QPSK channels over SMF, NZDSF and LS, with span length 100 km. The CUT is the center channel. The spacing is 1.05 times the symbol rate. Red dashed line: simulation, with SCI removed. Blue solid line: the GN model without SCI. Magenta solid line: the XPM approximation η_{XPM} of [30] (Eq. (3-51) here). Green solid line: η_{XMCI} estimated through the EGN model (Eq. (3-57)).

These results all assume just three channels. An interesting issue is whether the general picture shown in Fig. 3-7 changes when going to a higher number of channels. One might wonder whether the extent and/or hierarchy of the gaps vs. simulation may change among curves, or whether the EGN model might lose accuracy. This issue is dealt with in the next subsection, which also generalizes the MCI formulas to any number of WDM channels.

3.1.3.1   MCI for any number of WDM channels

When more than three channels are present in the comb, the picture of the MCI integration regions becomes more complex. In Fig. 3-8 we show an example of a nine-channel quasi-Nyquist WDM system, assuming $f = 0$ for simplicity. The plot contains all possible types of MCI regions, together with those generated by SCI and XCI. Even going to a higher channel number than nine, no new region types are generated.

In Fig. 3-8, the MCI regions are marked from M0 to M3. The white-filled regions (M0) correspond to regions whose contribution is simply the GN model; the other regions (M1-M3) have both a GN model contribution and a correction term. Since all regions have the GN model contribution, we can generalize and say that MCI as a whole can be written as:

$$G_{\mathrm{MCI}}^{\mathrm{EGN}}\left(f\right) = G_{\mathrm{MCI}}^{\mathrm{GN}}\left(f\right) - G_{\mathrm{MCI}}^{\mathrm{corr}} \qquad (3\text{-}58)$$

where $G_{\mathrm{MCI}}^{\mathrm{GN}}\left(f\right)$ is the MCI PSD according to the GN model (present in M0-M4), and $G_{\mathrm{MCI}}^{\mathrm{corr}}$ is the correction found in the M1-M3 regions.

If all channels are assumed to have the same transmitted power, that is,

$$P_{\mathrm{CUT}} = P_{\mathrm{INT},i} = P_{\mathrm{ch}} \quad i = -\left(N_{\mathrm{ch}}-1\right)/2, \ldots, -1, 1, \ldots, \left(N_{\mathrm{ch}}-1\right)/2 \qquad (3\text{-}59)$$

where N_{ch} (assumed odd) is the total number of channels and all INT channels are sitting symmetrically about CUT, then the MCI correction can be written as,

$$G_{\mathrm{MCI}}^{\mathrm{corr}} = \Phi_b P_{\mathrm{ch}}^3 \left(\kappa_{\mathrm{M1,2}}\left(f\right) + \kappa_{\mathrm{M2,2}}\left(f\right) + \kappa_{\mathrm{M3,2}}\left(f\right)\right) \qquad (3\text{-}60)$$

The main difference between MCI formulas and their similar XCI formulas is the integration limits, therefore we need to find out the channels where the two triples $\left(f_1, f_2, f_3\right)$ and $\left(f_1', f_2', f_3'\right)$ are located.
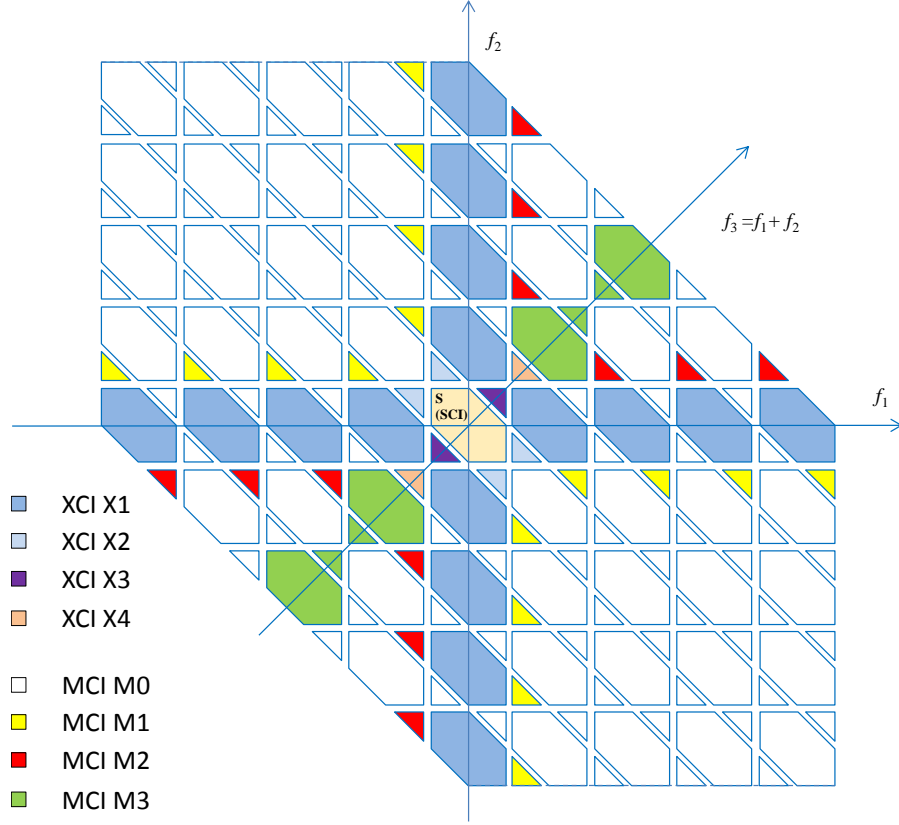
Fig. 3-8: Integration regions in the $[f_1, f_2]$ plane at $f = 0$, for a 9-channel WDM system with 4 left and 4 right INT channels adjacent to the CUT, with spacing slightly higher than the symbol rate. SCI is the center region. XCI and MCI regions are color-coded (see legend). The white-filled regions (all of type M0) have only the GN model term, all others have both the GN model term and one or more non-Gaussianity correction terms. Note that XPM amounts to the X1 regions only.

(a) M1: similar to X1

Due to the symmetry, we evaluated MCI in the domains locating in the II quadrant, parallel to f_2. We can get:

$$f_1, f_1' \in \text{INT}_{-1}, \quad f_2, f_3, f_2', f_3' \in \text{INT}_n, n = 1, 2, \ldots, (N_{ch} - 1)/2 \tag{3-61}$$

Therefore,

$$\kappa_{M1,2}(f) = 2 \cdot \frac{80}{81} R_s^2 \int_{-\Delta f - R_s/2}^{-\Delta f + R_s/2} df_1 \int_{n\Delta f - R_s/2}^{n\Delta f + R_s/2} df_2 \int_{n\Delta f - R_s/2}^{n\Delta f + R_s/2} df_2'$$

$$\left| s_{\text{INT}_{-1}}(f_1) \right|^2 s_{\text{INT}_n}(f_2) s_{\text{INT}_n}^*(f_2') s_{\text{INT}_n}^*(f_1 + f_2 - f) \tag{3-62}$$

$$s_{\text{INT}_n}(f_1 + f_2' - f) \mu(f_1, f_2, f) \mu^*(f_1, f_2', f)$$

$$\left(\text{with } n = 1, 2, \ldots, (N_{ch} - 1)/2 \right)$$

(b) M2: similar to X1

For the domains locating in the I quadrant, parallel to f_2. We can get:

$$f_1, f_1' \in \text{INT}_1, \quad f_2, f_3, f_2', f_3' \in \text{INT}_n, n = 2, 3, \ldots, (N_{\text{ch}} - 1)/2 \tag{3-63}$$

Therefore,

$$\kappa_{\text{M2,2}}(f) = 2 \cdot \frac{80}{81} R_s^2 \int_{\Delta f - R_s/2}^{\Delta f + R_s/2} df_1 \int_{n\Delta f - R_s/2}^{n\Delta f + R_s/2} df_2 \int_{n\Delta f - R_s/2}^{n\Delta f + R_s/2} df_2'$$

$$\left| s_{\text{INT}_1}(f_1) \right|^2 s_{\text{INT}_n}(f_2) s_{\text{INT}_n}^*(f_2') s_{\text{INT}_n}^*(f_1 + f_2 - f) \tag{3-64}$$

$$s_{\text{INT}_n}(f_1 + f_2' - f) \mu(f_1, f_2, f) \mu^*(f_1, f_2', f)$$

$$\left(\text{with } n = 2, 3, \ldots, (N_{\text{ch}} - 1)/2 \right)$$

(c) M3: similar to X3

For the domains locating in the I quadrant, we can get:

$$f_3, f_3' \in \text{INT}_n, n = 2, 3, \ldots, (N_{\text{ch}} - 1)/2$$

$$f_1, f_2, f_1', f_2' \in \text{INT}_m, m = \begin{cases} n/2, n \text{ is even} \\ (n \pm 1)/2, n \text{ is odd} \end{cases} \tag{3-65}$$

Therefore,

$$\kappa_{\text{M3,2}}(f) = 2 \cdot \frac{16}{81} R_s^2 \int_{m\Delta f - R_s/2}^{m\Delta f + R_s/2} df_1 \int_{m\Delta f - R_s/2}^{m\Delta f + R_s/2} df_2 \int_{m\Delta f - R_s/2}^{m\Delta f + R_s/2} df_2'$$

$$\left| s_{\text{INT}_n}(f_1 + f_2 - f) \right|^2 s_{\text{INT}_m}(f_1) s_{\text{INT}_m}(f_2) s_{\text{INT}_m}^*(f_2')$$

$$s_{\text{INT}_m}^*(f_1 + f_2 - f_2') \mu(f_1, f_2, f) \mu^*(f_1 + f_2 - f_2', f_2', f) \tag{3-66}$$

$$\left(\text{with} \begin{cases} n = 2, 3, \ldots, (N_{\text{ch}} - 1)/2 \\ m = \begin{cases} n/2, n \text{ is even} \\ (n \pm 1)/2, n \text{ is odd} \end{cases} \end{cases} \right)$$

Such equations, together with the ones for SCI and XCI, make the overall EGN model capable of dealing with any number of channels, for any type of NLI. Note that the MCI domains M1 and M2 are non-empty as long as the INT channel adjacent to the CUT is not too far from the CUT. Both regions M1 and M2 disappear when $|\Delta f| \geq 2R_s$, for any value of f in the CUT band.

Using these general formulas, in Fig. 3-9 we draw the same plot as Fig. 3-7, except

now nine WDM channels are present: the CUT and four adjacent INT channels on each side of the CUT. A comparison of the figures shows that, interestingly, the general picture is unchanged. The excellent accuracy of the EGN model in estimating η_{XMCI} is confirmed (green solid line) vs. simulations (red dashed) for all fibers.

In Fig. 3-10, the channel count goes up to fifteen, the CUT and seven adjacent INT channels on each side of the CUT, which is the largest number that we could cover through simulations. The behaviors of the three models (GN, EGN and XPM) vs. simulations are kept, at this higher channel count too, for all fibers.

3.1.4 The overall nonlinear interference

After obtaining all the formulas for SCI, XCI and MCI, the overall NLI can be calculated by:

$$G_{\text{NLI}}^{\text{EGN}}(f) = G_{\text{SCI}}^{\text{EGN}}(f) + G_{\text{XCI}}^{\text{EGN}}(f) + G_{\text{MCI}}^{\text{EGN}}(f) \qquad (3\text{-}67)$$

Note that each one of the right-hand side terms possesses both a GN model part and a correction part. For instance: $G_{\text{SCI}}(f) = G_{\text{SCI}}^{\text{GN}}(f) - G_{\text{SCI}}^{\text{corr}}(f)$, and similarly for $G_{\text{XCI}}^{\text{EGN}}(f)$ and $G_{\text{MCI}}^{\text{EGN}}(f)$.

For the same system set-ups addressed in Sect. 3.1.2.2 we calculated η_{NLI}, defined as:

$$\eta_{\text{NLI}} = P_{\text{ch}}^{-3} \int_{-R_s/2}^{R_s/2} G_{\text{NLI}}^{\text{EGN}}(f)df \qquad (3\text{-}68)$$

with $G_{\text{NLI}}^{\text{EGN}}(f)$ given by Eq. (3-67).

In Fig. 3-11, all NLI are calculated for the same system in Fig. 3-10. In this figure, we did not plot the curve "XPM" again. The plots show that after the first few spans, the agreement is excellent for SMF and NZDSF and still rather good for LS fiber. The overall accuracy improvement over the GN model is very substantial.

3.2 Estimating System Performance

In this section, we shift focus from the characterization of NLI accumulation along the link to system analysis. In fact, the main declared goal of the GN model has always been that of providing a practical tool for realistic system performance prediction. Here, we present a comparison of the accuracy of the GN model and of the EGN model in predicting system maximum reach.
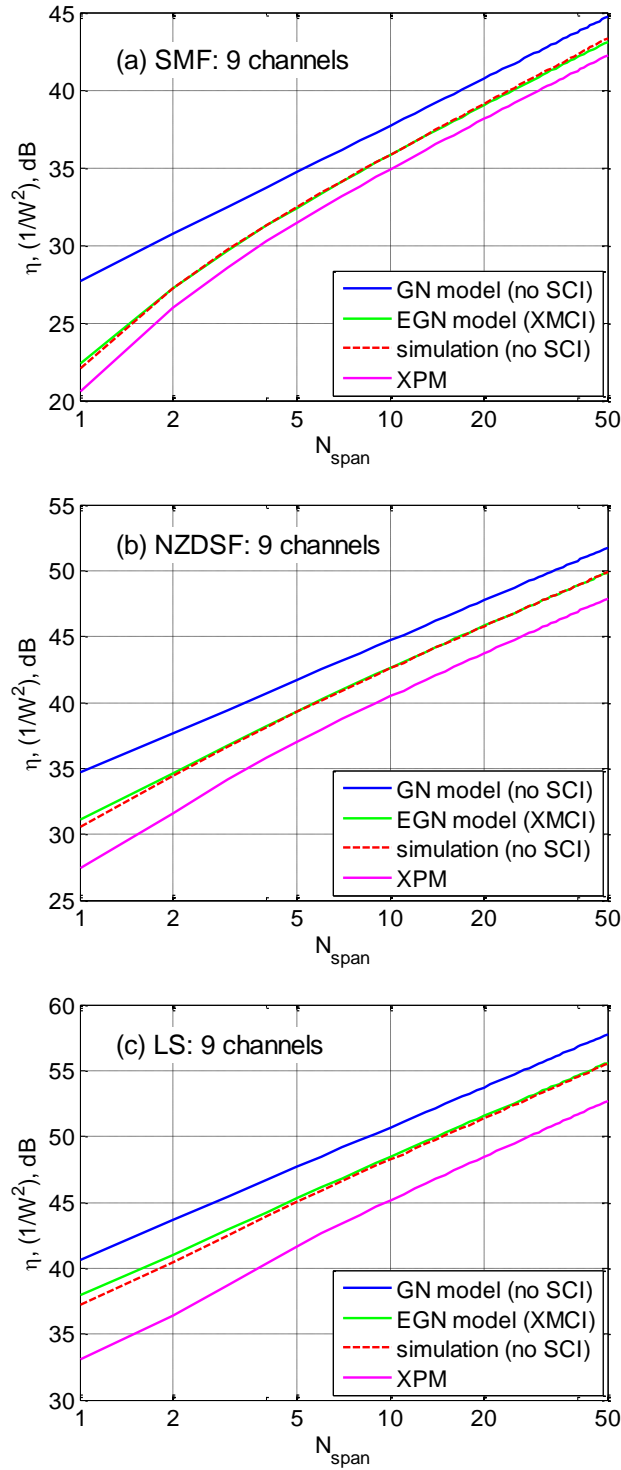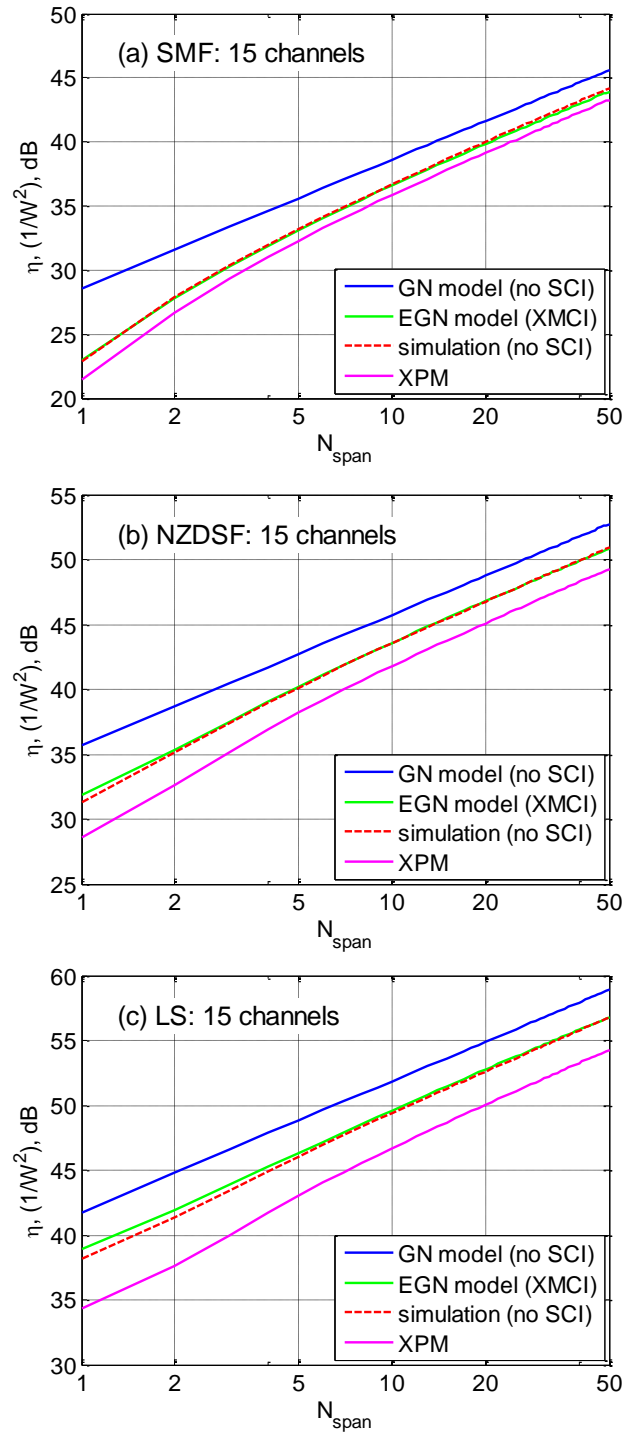
Fig. 3-9: Plot of normalized nonlinearity coefficient η vs. number of spans in the link, assuming 9 PM-QPSK channels over SMF, NZDSF and LS, with span length 100 km. The CUT is the center channel. The spacing is 1.05 times the symbol rate. Red dashed line: simulation, with SCI removed. Blue solid line: the GN model without SCI. Magenta solid line: the XPM approximation η_{XPM} of [30] (Eq. (3-51) here). Green solid line: η_{XMCI} estimated through the EGN model (Eq. (3-57)).
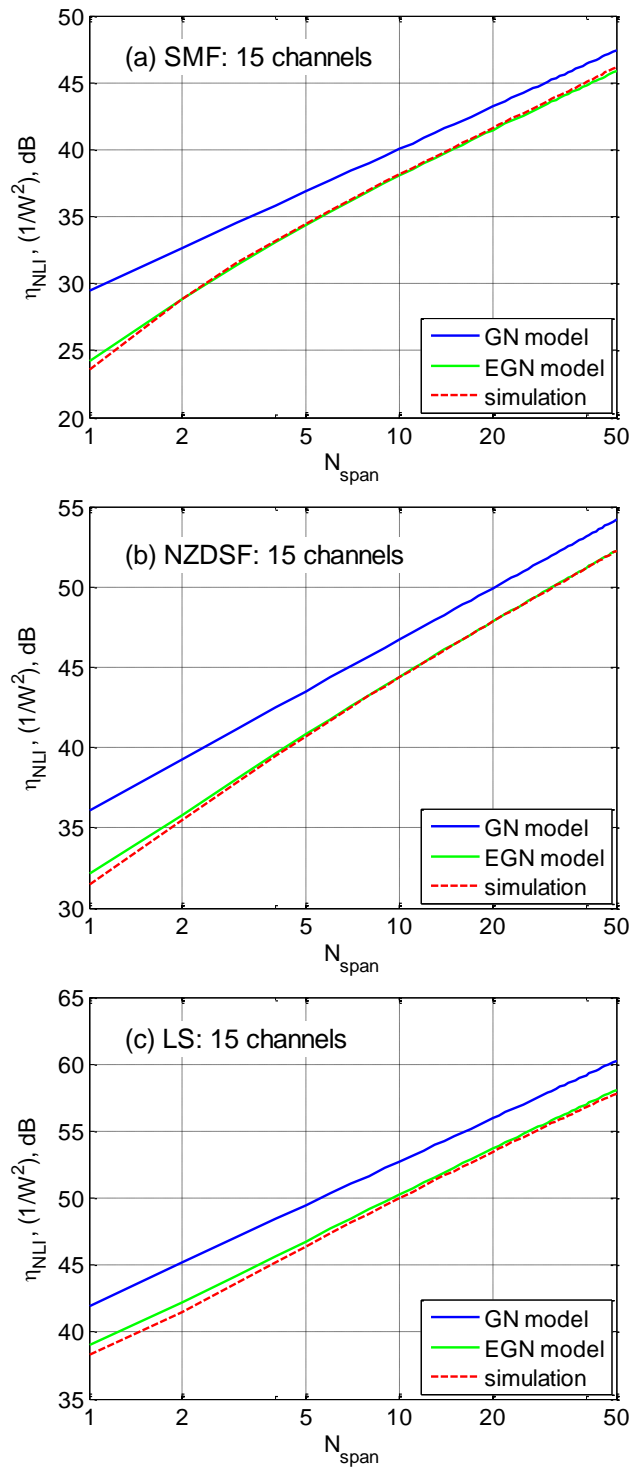
Fig. 3-10: Plot of normalized nonlinearity coefficient η vs. number of spans in the link, assuming 15 PM-QPSK channels over SMF, NZDSF and LS, with span length 100 km. The CUT is the center channel. The spacing is 1.05 times the symbol rate. Red dashed line: simulation, with SCI removed. Blue solid line: the GN model without SCI. Magenta solid line: the XPM approximation $\eta_{\scriptscriptstyle XPM}$ of [30] (Eq. (3-51) here). Green solid line: $\eta_{\scriptscriptstyle XMCI}$ estimated through the EGN model (Eq. (3-57)).

Fig. 3-11: Plot of normalized nonlinearity coefficient η vs. number of spans in the link, assuming 15 PM-QPSK channels over SMF, NZDSF and LS, with span length 100 km. The CUT is the center channel. The spacing is 1.05 times the symbol rate. Red dashed line: simulation. Blue solid line: the GN model. Green solid line: η_{NLI} estimated through the EGN model (Eq. (3-68)).

The systems that we tested are identical to those described in [38], Sect. V. Specifically, they are 15-channel WDM PM-QPSK and PM-16QAM systems, running at 32 GBaud. The simulation technique is also similar to that of [38]. The simulated data length was 130,000 symbols. The target BERs were $1.7 \cdot 10^{-3}$ and $2 \cdot 10^{-3}$ respectively, found by assuming a 10^{-2} FEC threshold, decreased by 2 dB of realistic OSNR system margin. We considered the following channel spacings: 33.6, 35, 40, 45 and 50 GHz. The spectrum was root-raised-cosine with roll-off 0.05. EDFA amplification was assumed, with 5 dB noise figure. The considered fibers were: SMF, NZDSF and LS, with same parameters as listed in Sect. 3.1.1, with the exception of the SMF loss that was $\alpha_{dB} = 0.2$ dB/km rather than 0.22. In addition, we also considered PSCF with the following parameters: $D = 20.1$ ps/(nm km), $\gamma = 0.8$ 1/(W km), $\alpha_{dB} = 0.17$ dB/km.

Fig. 3-12 shows a plot of system maximum reach vs. channel spacing. Squares are simulation results. The dashed line is the GN model and the solid line is the EGN model. Note that lines are just visual aids. The actually calculated data points are the filled circles. The GN model underestimates the system maximum reach by 0.3-0.6 dB over PSCF, SMF and NZDSF, in agreement with [38, 39]. The error goes up to 0.8 dB in the case of the very low dispersion and high nonlinearity LS fiber.

These errors are in line with the typical amount of NLI overestimation by the GN model that emerges from the previous sections, when taking into account the "1/3 rule".

With all fibers and spacings, the EGN model provides very good accuracy, completely removing the underestimation error incurred by the GN model. The error is less than 0.2 dB across all system configurations. At this error level, it is difficult to attribute it to either model inaccuracy or Monte-Carlo uncertainty.

We would like to point out that a slight difference, on the order of small fractions of a dB, is visible between some of the system results shown in [38], and the ones reported here in Fig. 3-12. They are due to two circumstances. First, in [38] the local-white-noise approximation was used in the calculation of NLI using the GN model. Such approximation consists of assuming that the NLI spectrum is essentially flat over the bandwidth of the channel under test. Here, the non-flatness of the NLI spectrum was fully taken into account when plotting all the figures in this chapter. Specifically regarding Fig. 3-12, the difference between taking and not taking the non-flat NLI

spectrum into account causes an upshift of the analytical curves ranging between 0.05 dB for Δf =33.6 GHz and 0.15 dB for Δf = 50 GHz. As a result, the GN model prediction here is different from [37] by this much.
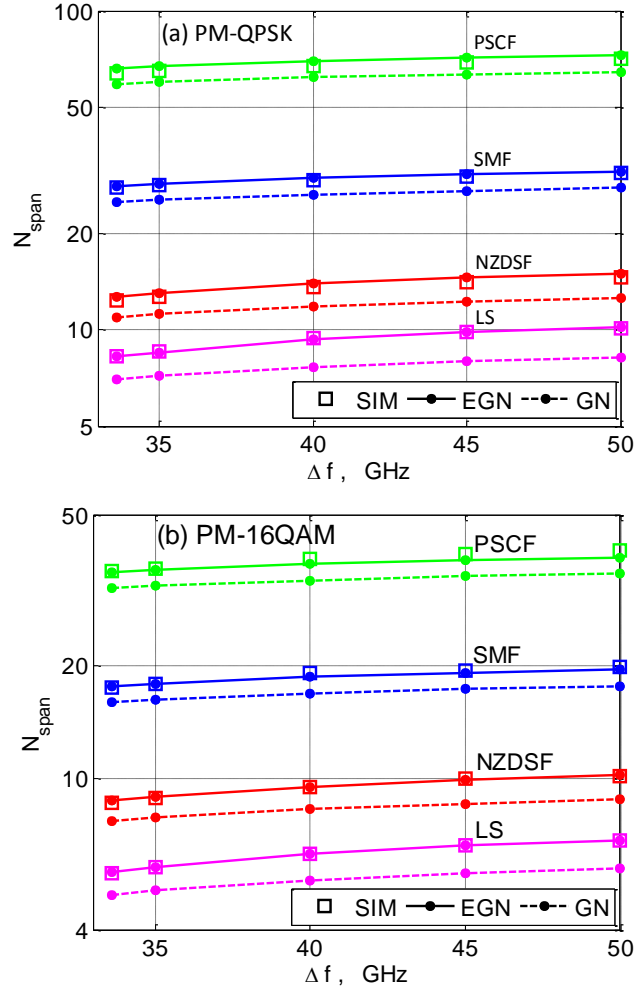

Fig. 3-12: Plot of maximum system reach for 15-channel PM-QPSK and PM-16QAM systems at 32 GBaud, vs. channel spacing, over four different fiber types: PSCF, SMF, NZDSF and LS. The span length is 120 km for PM-QPSK and 85 km for PM-16QAM. Small filled circles: analytical predictions. Square hollow markers: simulations. Lines were added to connect analytical points as a visual aid. Dashed line: the GN model. Solid line: the EGN model.

A second difference with [38] is that the simulations there, for the sake of full realism, were run with ASE noise added in-line along the link. Here, we want to carefully validate a model that neglects the interaction of in-line ASE noise with nonlinearity, so we added all ASE noise at the end of the link. The effect is that all simulative PM-QPSK results are pulled up here by about 0.15 dB on average. The effect on PM-16QAM is

almost negligible (less than 0.05 dB), because PM-16QAM requires a much higher OSNR at the receiver and hence much less ASE noise is present along the link than for PM-QPSK.

3.3 Discussion

3.3.1 Accuracy vs. computational effort

The GN model overestimates NLI. The amount of overestimation is large in the first few spans (several dB's) but it abates along the link. When looked at for a number of spans that is close to the system maximum reach, the error on NLI power estimation is typically 1 to 2 dB, depending on fiber type, modulation format and span length, for realistic systems. Larger errors can be found by pushing the system parameters to extremes, such as single-polarization, lossless fiber (or ideal distributed amplification) or very short spans.

The GN model errors in NLI power estimation in turn lead to about 0.3-0.6 dB of error on the prediction of the system maximum reach or of the optimum launch power, for typical realistic systems. This error may or may not be acceptable, depending on applications, but is guaranteed to be conservative (i.e., reach is underestimated) for PM-QAM systems. When such error is not acceptable, the EGN model can be used, which is capable of providing very accurate estimates of NLI variance at any number of spans along the link, potentially for any format and system set of parameters.

The results of Fig. 3-12 contain both simulations and analytical calculations. The simulations required a large CPU effort, due to our will to impose very strict accuracy constraints. Please see [38] for a description of simulation accuracy settings. As a whole, the simulated points populating Fig. 3-12 required several months of equivalent single-core CPU (PC-type) time. This should not surprise, since accurately finding system maximum reach by simulation requires demodulating the signal at multiple spans and also scanning numerous launch powers at small steps. For each launch power, an entirely new simulation must be run. Some optimizations are possible but the overall burden is massive.

The EGN model calculations needed to generate the corresponding data points, thanks to various optimizations, were trimmed down to about 15 days of total single-core CPU

time. One key factor contributing to reducing the computational effort of the EGN model is the fact that, even when three or more nested integrals are present in any of NLI contributions, the actual complexity is always equivalent to a double integral. This aspect is explained in Appendix 3C. Another important speed-up circumstance vs. simulations is that the model calculations do not need to be run at different launch powers. Once the normalized coefficient η_{NLI} has been estimated, NLI can be extrapolated to any power by simply scaling it analytically by P_{ch}^3. One circumstance acting against model calculations efficiency is however that if very high accuracy is needed, the NLI white-noise approximation used for instance in [38] must be avoided. This entails evaluating the NLI PSD (essentially η_{NLI}) at many frequencies inside the CUT bandwidth (32 GHz in our case) and then averaging them. We used a step of 1 GHz, which we found sufficient.

Despite forgoing the white-noise approximation, the EGN model CPU gain vs. Monte-Carlo simulations was still quantifiable as a factor of 10-20. It should however be mentioned that we were conservative as to setting the integration parameters for accuracy. Also, we think the efficiency of our code could be improved upon. As a result, we feel that it should be possible to push the previously mentioned speed-up factor to at least 20-40. This factor is significant. It is however not significant enough to make the EGN model a real-time tool for quick system optimization. We should also point out that not even the GN model can be considered a real-time tool, as the speed-up of the GN model vs. the EGN model is only about another factor of 5-10, insufficient for real-time use.

The fastest GN related model available is the incoherent GN model, whose accuracy was shown to typically appear to be even better than the GN model [38]. This is somewhat surprising, since the incoherent GN model is derived from the GN model by making one further approximation, namely that the NLI produced in each span sums up incoherently (that is, in power) at the receiver [14, 15, 17, 38]. However, as explained in [38], it benefits from an error cancellation circumstance. This means that, while the GN model produces a guaranteed lower bound to the maximum reach, the incoherent GN model can be either pessimistic or optimistic. On the other hand, its speed of computation is 10-20 times faster than the GN model, and another order of magnitude

can be gained if the white noise assumption is used. In essence, the incoherent GN model is so far the fastest tool, and essentially a real-time tool, for system performance assessment. On the other hand, caution must be used and its limitations must be fully understood to use it properly. Its margin of error can potentially be substantial, although so far, in the context of many validation campaigns using realistic system parameters [14, 15, 38], it has been consistently found to be rather accurate. It should also be mentioned that a number of closed-form or quasi-closed form analytical solutions have also been worked out for both the GN model and the incoherent GN model [17, 40, 41], which clearly reduce complexity to almost negligible levels, at the cost of some potential loss of accuracy.

The best of all options would arguably be that of finding a tool with a similar complexity as the incoherent GN model, whose accuracy would however not rest on an error cancellation, but on firm theoretical ground. A first promising attempt towards this direction, based on an analytical closed-form approximation to the EGN model, is reported in Chapter 4.

Overall, an array of analytical tools are already available for the system designer, with different degrees of complexity and accuracy that can be tailored to specific needs. Trade-offs between accuracy and complexity can already be addressed with numerous options at hand.

3.3.2 Nonlinear phase noise

One of the assumptions used by the GN model, as well as by most prior nonlinearity models, is that of NLI being approximately Gaussian and additive, so that its system impact can be assessed simply by summing its variance to that of ASE noise. This assumption was challenged in [30] and [31]. The claim of [30] is that a very substantial part of the XCI contribution to NLI is in fact phase noise (PN) and hence non-additive. In addition, such PN appears to have a very long correlation time, on the order of tens or even hundreds of symbols.

The presence of a nonlinear noise component with very long correlation time had first been pointed out in [26], there too attributed to "cross-phase modulation". The correlation results in [30] actually agree well with those found earlier in [26]. Both papers, however, concentrate on a single-polarization, lossless fiber scenario to assess

the strength of the long-correlated PN component of NLI. In that idealized context, the PN component may indeed turn out to be very large.

In this section, we investigated this important issue by carrying out an in-depth simulative span-by-span characterization of PN in UT links using realistic span lengths and amplification schemes, in dual-polarization. The system is the same as in Sect. 3.1.2, with nine channels. The fiber is NZDSF, and span length is either 100 or 60 km. Lumped amplification is assumed but no ASE noise is injected to avoid masking NLI noise.

We characterized PN at the Rx as follows. The signal is demodulated using a matched filter. Polarization is recovered statically. No dynamic equalizer is present which could perturb the constellation or otherwise remove long-correlated noise components. Similar to [30] and [31], we eliminated all SCI effects. one reason for this is for easier comparison with [30] and [31]. Another reason is that this provides a better picture of what could be the behavior of a fully loaded system, where SCI effects would be relatively small. At any rate, we provide indications on SCI effects, as well.

The signal is analyzed as shown in Fig. 3-13. The four constellation points are analytically rotated so that they superimpose on the horizontal axis, in such a way that the major and minor axes of the four ellipses shown in figure are aligned. PN, if present, shows up on the tangential $\hat{\varphi}$ axis. To study it in detail, we estimated the auto- and cross-correlation functions of the $\hat{\varphi}$ and $\hat{\rho}$ NLI components, that is: $R_{\hat{\varphi}\hat{\varphi}}(k), R_{\hat{\rho}\hat{\rho}}(k)$ and $R_{\hat{\varphi}\hat{\rho}}(k)$ where k is the delay in number of symbol times. The variances of $\hat{\varphi}$ and $\hat{\rho}$ NLI are given by $\sigma_{\hat{\varphi}}^2 = R_{\hat{\varphi}\hat{\varphi}}(0)$, $\sigma_{\hat{\rho}}^2 = R_{\hat{\rho}\hat{\rho}}(0)$. If substantial PN was present, we would expect $\sigma_{\hat{\varphi}}^2 \gg \sigma_{\hat{\rho}}^2$, i.e., elliptic noisy signal "points" would show up as pictured in Fig. 3-13, similar to results shown in [30, 31]. Also, if PN had a long-correlated component, it would show up as non-zero values of the $R_{\hat{\varphi}\hat{\varphi}}(k)$ curve for $|k| \neq 0$.

In Fig. 3-14 we plot the measured results on the center channel, vs. number of spans N_s. We show results on one polarization, the other being identical. All results are normalized vs. P_{ch}^3, where P_{ch} is the power per channel. According to theoretical models, such normalization makes the results launch-power independent.
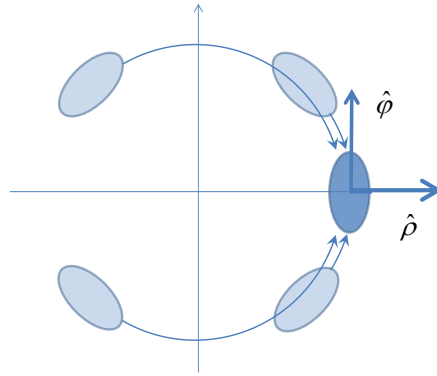
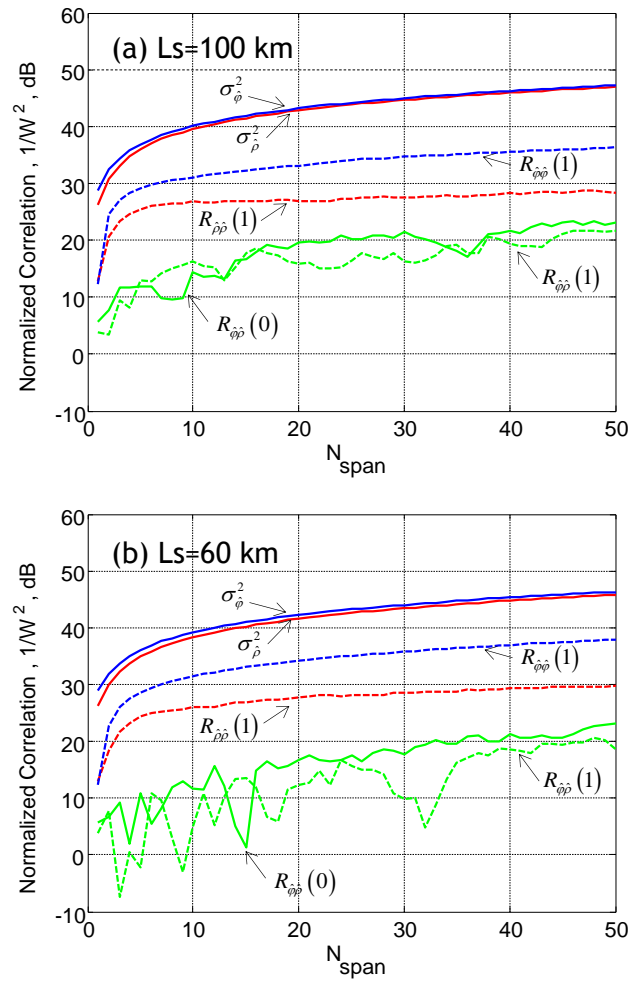Fig. 3-13: Phase noise detection post-processing for PM-QPSK.

Fig. 3-14: Plots of variances and auto- and cross-correlation functions of the $\hat{\varphi}$ and $\hat{\rho}$ components of NLI noise, vs. number of spans (SCI is removed). Correlation arguments are in symbol-time intervals. The system is 9-channel PM-QPSK, 32GBaud, quasi-Nyquist. The fiber is NZDSF.

Fig. 3-14 shows that after one span $\sigma^2_{\hat{\varphi}}$ is about 2.5 dB larger than $\sigma^2_{\hat{\rho}}$, both for 60 and 100 km NZDSF spans. However, already at ten spans the difference is down to 0.8 and

0.5 dB (respectively) and tends to vanish at higher span count. Similar variance means that approximately "circular" noise shows up in the signals post-processed as in Fig. 3-13 (small ellipticity of the constellation points). To provide visual evidence, in Fig. 3-15 we show a plot structured as Fig. 3-13, extracted from the simulation at 20 spans of NZDSF (100km spans), where $\sigma_{\hat{\varphi}}^2 / \sigma_{\hat{\rho}}^2$=0.37 dB. The individual signal points, as well as the "superimposition" one, show in fact very little "ellipticity".
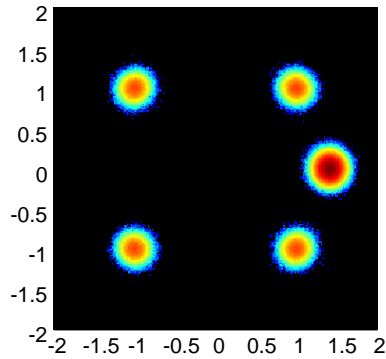

Fig. 3-15: Constellation and "superimposed" signal point, structured as Fig. 3-13, for an actually simulated case: 20 spans of NZDSF, span length 100km, 9-channel PM-QPSK, 32GBaud, quasi-Nyquist. SCI is removed.
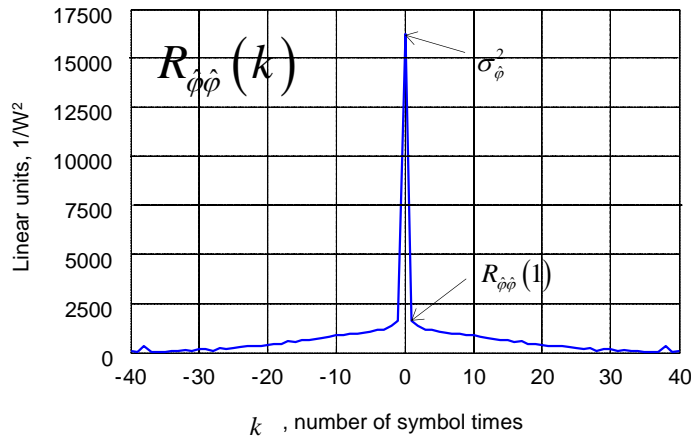

Fig. 3-16: Plot of the normalized autocorrelation function of the $\hat{\varphi}$ component of NLI noise, $R_{\hat{\varphi}\hat{\varphi}}(k)$, vs. number of symbol intervals, for NZDSF at 20 spans, span length 100 km. SCI is removed.

Regarding the presence of a long-correlated PN component, in Fig. 3-16 we show the PN autocorrelation function $R_{\hat{\varphi}\hat{\varphi}}(k)$ for NZDSF (100 km spans) at 20 spans, which presents a sharp peak $R_{\hat{\varphi}\hat{\varphi}}(0)$ (i.e., the variance $\sigma_{\hat{\varphi}}^2$) and then a slowly decaying trend vs.

the delay k. Both [26, 30], predicted a slowly-decaying $\hat{\varphi}$ autocorrelation, so our results agree with this prediction. However, such long-correlated component appears to be small. A possible measure of its strength is the ratio $R_{\hat{\varphi}\hat{\varphi}}(1)/\sigma_{\hat{\varphi}}^2$ where $R_{\hat{\varphi}\hat{\varphi}}(1)$ is the correlation of PN at one symbol delay. Both Fig. 3-14 and Fig. 3-16 show that such ratio is small and Fig. 3-14 shows that it steadily goes down along the link. At 20 spans, it is -10 and -8 dB, for 100 and 60 km spans, respectively. Finally, in Fig. 3-14 we also plot the cross-correlation function $R_{\hat{\varphi}\hat{\rho}}(k)$ for k =0 and 1. These curves are less than -20 dB vs. $\sigma_{\hat{\varphi}}^2$ and $\sigma_{\hat{\rho}}^2$. Not shown, $R_{\hat{\varphi}\hat{\rho}}(k)$ stays this low for any value of k. These results indicate that the $\hat{\varphi}$ and $\hat{\rho}$ NLI components are essentially uncorrelated.

When SCI is not suppressed, at 10 spans of NZDSF, the ratio $\sigma_{\hat{\varphi}}^2/\sigma_{\hat{\rho}}^2$ goes up slightly, to 1 and 0.7 dB (60 and 100 km spans, respectively), still tending to vanish vs. N_s. Therefore, the PN in NLI is limited and has little impact on system performance for typical PM-QPSK systems. The impact of PN on PM-16QAM is currently under investigation.

Appendix 3A: Some relevant ξ_n moments calculation

In frequency-domain, the transmitted symbol sequence in a generic INT can be written as:

$$\xi_n = \sqrt{f_0}\, s\left(nf_0\right) \sum_{\omega=0}^{W-1} b_\omega e^{-j\frac{2\pi}{W}\omega n} \tag{3A-1}$$

Its 2nd-order moment is well known as,

$$\mathrm{E}\left\{\xi_m \xi_n^*\right\} = R_s \left|s\left(mf_0\right)\right|^2 \mathrm{E}\left\{\left|b\right|^2\right\}\left(\delta_{m-n+pW}\right)_{p=0,\pm 1,\ldots} \tag{3A-2}$$

Its 4th-order moment is,

$$
\begin{aligned}
&\mathrm{E}\left\{\xi_m \xi_n^* \xi_{m'}^* \xi_{n'}\right\} \\
&= \mathrm{E}\left\{\sqrt{f_0}\, s\left(mf_0\right) \sum_{\omega_1=0}^{W-1} b_{\omega_1} e^{-j\frac{2\pi}{W}\omega_1 m} \cdot \sqrt{f_0}\, s^*\left(nf_0\right) \sum_{\omega_2=0}^{W-1} b_{\omega_2}^* e^{j\frac{2\pi}{W}\omega_2 n} \right. \\
&\left. \cdot \sqrt{f_0}\, s^*\left(m'f_0\right) \sum_{\omega_3=0}^{W-1} b_{\omega_3}^* e^{j\frac{2\pi}{W}\omega_3 m'} \cdot \sqrt{f_0}\, s\left(n'f_0\right) \sum_{\omega_4=0}^{W-1} b_{\omega_4} e^{-j\frac{2\pi}{W}\omega_4 n'} \right\} \\
&= f_0^2 \mathcal{P}_{mnm'n'} \sum_{\omega_1=0}^{W-1} \sum_{\omega_2=0}^{W-1} \sum_{\omega_3=0}^{W-1} \sum_{\omega_4=0}^{W-1} \mathrm{E}\left\{b_{\omega_1} b_{\omega_2}^* b_{\omega_3}^* b_{\omega_4}\right\} e^{-j\frac{2\pi}{W}\left(\omega_1 m - \omega_2 n - \omega_3 m' + \omega_4 n'\right)}
\end{aligned}
\tag{3A-3}
$$

where $\mathcal{P}_{mnm'n'} = s(mf_0)s^*(nf_0)s^*(m'f_0)s(n'f_0)$.

The calculation of the 4th-order correlation of RV b can be split to two groups:

- $\omega_1 = \omega_2 = \omega_3 = \omega_4$: the four-summation can be reduced to one single-summation.

$$\begin{aligned}
\mathrm{E}^{(1)}\left\{\xi_m\xi_n^*\xi_{m'}^*\xi_{n'}\right\} &= f_0^2\mathcal{P}_{mnm'n'}\mathrm{E}\left\{|b|^4\right\}\sum_{\omega_1=0}^{W-1} e^{-j\frac{2\pi}{W}\omega_1(m-n-m'+n')} \\
&= R_s f_0 \mathrm{E}\left\{|b|^4\right\}\mathcal{P}_{mnm'n'}\left(\delta_{m-n-m'+n'+pW}\right)_{p=0,\pm1,\dots}
\end{aligned}$$
(3A-4)

where we used the stationary $\mathrm{E}\left\{|b|^4\right\} = \mathrm{E}\left\{\left|b_{\omega_i}\right|^4\right\}$.

- $\left\{\omega_i=\omega_j, i=1,4, j=2,3\right\}, \omega_1\neq\omega_4$: the four-summation can be reduced to two double-summation.

(2.1) $\left\{\omega_1=\omega_2, \omega_4=\omega_3, \omega_1\neq\omega_4\right\}$

$$\begin{aligned}
&\mathrm{E}^{(2.1)}\left\{\xi_m\xi_n^*\xi_{m'}^*\xi_{n'}\right\} \\
&= f_0^2\mathcal{P}_{mnm'n'}\cdot\mathrm{E}^2\left\{|b|^2\right\}\sum_{\omega_1=0}^{W-1} e^{-j\frac{2\pi}{W}\omega_1(m-n)}\sum_{\omega_4=0, \omega_4\neq\omega_1}^{W-1} e^{-j\frac{2\pi}{W}\omega_3(-m'+n')} \\
&= f_0^2\mathrm{E}^2\left\{|b|^2\right\}\mathcal{P}_{mnm'n'}\left(W^2\delta_{m-n+pW}\delta_{-m'+n'+pW} - W\delta_{m-n-m'+n'+pW}\right)_{p=0,\pm1,\dots} \\
&= R_s^2\mathrm{E}^2\left\{|b|^2\right\}\mathcal{P}_{mnm'n'}\left(\delta_{m-n+pW}\delta_{-m'+n'+pW}\right)_{p=0,\pm1,\dots} \\
&\quad - R_s f_0\mathrm{E}^2\left\{|b|^2\right\}\mathcal{P}_{mnm'n'}\left(\delta_{m-n-m'+n'+pW}\right)_{p=0,\pm1,\dots}
\end{aligned}$$
(3A-5)

(2.2) $\left\{\omega_1=\omega_3, \omega_4=\omega_2, \omega_1\neq\omega_4\right\}$

$$\begin{aligned}
&\mathrm{E}^{(2.2)}\left\{\xi_m\xi_n^*\xi_{m'}^*\xi_{n'}\right\} \\
&= R_s^2\mathrm{E}^2\left\{|b|^2\right\}\mathcal{P}_{mnm'n'}\left(\delta_{m-m'+pW}\delta_{-n+n'+pW}\right)_{p=0,\pm1,\dots} \\
&\quad - R_s f_0\mathrm{E}^2\left\{|b|^2\right\}\mathcal{P}_{mnm'n'}\left(\delta_{m-n-m'+n'+pW}\right)_{p=0,\pm1,\dots}
\end{aligned}$$
(3A-6)

Putting these contributions together, we can get,

$$\begin{aligned}
\mathrm{E}\left\{\xi_m\xi_n^*\xi_{m'}^*\xi_{n'}\right\} &= \mathrm{E}^{(1)}\left\{\xi_m\xi_n^*\xi_{m'}^*\xi_{n'}\right\} + \mathrm{E}^{(2)}\left\{\xi_m\xi_n^*\xi_{m'}^*\xi_{n'}\right\} + \mathrm{E}^{(3)}\left\{\xi_m\xi_n^*\xi_{m'}^*\xi_{n'}\right\} \\
&= R_s^2\mathrm{E}^2\left\{|b|^2\right\}\mathcal{P}_{mnm'n'}\left(\delta_{m-n+pW}\delta_{n'-m'+pW} + \delta_{m-m'+pW}\delta_{n'-n+pW}\right)_{p=0,\pm1,\dots} \\
&\quad + R_s f_0\left[\mathrm{E}\left\{|b|^4\right\} - 2\mathrm{E}^2\left\{|b|^2\right\}\right]\mathcal{P}_{mnm'n'}\left(\delta_{m-n-m'+n'+pW}\right)_{p=0,\pm1,\dots}
\end{aligned}$$
(3A-7)

Its 6th-order moment is:

$$
E\left\{\xi_m \xi_n^* \xi_k \xi_{m'}^* \xi_{n'} \xi_{k'}^*\right\}
$$

$$
= f_0^3 \mathcal{P}_{mnkm'n'k'} \sum_{\omega_1=0}^{W-1} \sum_{\omega_2=0}^{W-1} \sum_{\omega_3=0}^{W-1} \sum_{\omega_4=0}^{W-1} \sum_{\omega_5=0}^{W-1} \sum_{\omega_6=0}^{W-1} \tag{3A-8}
$$

$$
E\left\{b_{\omega_1} b_{\omega_2}^* b_{\omega_3} b_{\omega_4}^* b_{\omega_5} b_{\omega_6}^*\right\} e^{-j\frac{2\pi}{W}(\omega_1 m - \omega_2 n + \omega_3 k - \omega_4 m' + \omega_5 n' - \omega_6 k')}
$$

where $\mathcal{P}_{mnkm'n'k'} = s(mf_0)s^*(nf_0)s(kf_0)s^*(m'f_0)s(n'f_0)s^*(k'f_0)$, and the 6th-order correlation of RV b can be split to three groups.

- $\omega_1 = \omega_2 = \omega_3 = \omega_4 = \omega_5 = \omega_6$: the six-summation can be reduced to one single-summation.

$$
E^{(1)}\left\{\xi_m \xi_n^* \xi_k \xi_{m'}^* \xi_{n'} \xi_{k'}^*\right\}
$$

$$
= f_0^3 \mathcal{P}_{mnkm'n'k'} E\left\{|b|^6\right\} \sum_{\omega_1=0}^{W-1} e^{-j\frac{2\pi}{W}\omega_1(m-n+k-m'+n'-k')} \tag{3A-9}
$$

$$
= R_s f_0^2 E\left\{|a_0|^6\right\} \mathcal{P}_{mnkm'n'k'} \left(\delta_{m-n+k-m'+n'-k'+pW}\right)_{p=0,\pm1,\ldots}
$$

- Two of them are identical, and the other four are identical, thus the six-summation can be reduced to nine dual-summation.

(2.1) $\omega_1 = \omega_2, \omega_3 = \omega_4 = \omega_5 = \omega_6, \omega_1 \neq \omega_3$

(2.2) $\omega_1 = \omega_4, \omega_3 = \omega_2 = \omega_5 = \omega_6, \omega_1 \neq \omega_3$

(2.3) $\omega_1 = \omega_6, \omega_3 = \omega_4 = \omega_5 = \omega_2, \omega_1 \neq \omega_3$

(2.4) $\omega_3 = \omega_2, \omega_1 = \omega_4 = \omega_5 = \omega_6, \omega_3 \neq \omega_1$

(2.5) $\omega_3 = \omega_4, \omega_1 = \omega_2 = \omega_5 = \omega_6, \omega_3 \neq \omega_1$

(2.6) $\omega_3 = \omega_6, \omega_1 = \omega_4 = \omega_5 = \omega_2, \omega_3 \neq \omega_1$

(2.7) $\omega_5 = \omega_2, \omega_1 = \omega_4 = \omega_3 = \omega_6, \omega_5 \neq \omega_1$

(2.8) $\omega_5 = \omega_4, \omega_1 = \omega_2 = \omega_3 = \omega_6, \omega_5 \neq \omega_1$

(2.9) $\omega_5 = \omega_6, \omega_1 = \omega_4 = \omega_3 = \omega_2, \omega_5 \neq \omega_1$

Here we only give the procedure for calculating (2.1).

$$\mathrm{E}^{(2.1)}\left\{\xi_m \xi_n^* \xi_k \xi_{m'}^* \xi_{n'} \xi_{k'}^*\right\}$$

$$= f_0^3 \mathcal{P}_{mnkm'n'k'} \mathrm{E}\left\{|b|^2\right\} \sum_{\omega_1=0}^{W-1} e^{-j\frac{2\pi}{W}\omega_1(m-n)} \mathrm{E}\left\{|b|^4\right\} \sum_{\omega_3=0,\,\omega_3\neq\omega_1}^{W-1} e^{-j\frac{2\pi}{W}\omega_3(k-m'+n'-k')}$$

$$= f_0^3 \mathrm{E}\left\{|b|^2\right\} \mathrm{E}\left\{|b|^4\right\} \mathcal{P}_{mnkm'n'k'}$$

$$\cdot\left(W^2 \delta_{m-n+pW} \delta_{k-m'+n'-k'+pW} - W\delta_{m-n+k-m'+n'-k'+pW}\right)_{p=0,\pm1,\dots}$$ (3A-10)

$$= R_s^2 \mathrm{E}\left\{|b|^2\right\} \mathrm{E}\left\{|b|^4\right\} \mathcal{P}_{mnkm'n'k'} \left(\delta_{m-n+pW} \delta_{k-m'+n'-k'+pW}\right)_{p=0,\pm1,\dots}$$

$$-R_s f_0^2 \mathrm{E}\left\{|b|^2\right\} \mathrm{E}\left\{|b|^4\right\} \mathcal{P}_{mnkm'n'k'} \left(\delta_{m-n+k-m'+n'-k'+pW}\right)_{p=0,\pm1,\dots}$$

- $\left\{\omega_i = \omega_j, i = 1,3,5, j = 2,4,6\right\}, \omega_1 \neq \omega_3 \neq \omega_5$: the six-summation can be reduced to six triple-summation.

  (3.1) $\omega_1 = \omega_2, \omega_3 = \omega_4, \omega_5 = \omega_6$ (3.2) $\omega_1 = \omega_2, \omega_3 = \omega_6, \omega_5 = \omega_4$

  (3.3) $\omega_1 = \omega_4, \omega_3 = \omega_2, \omega_5 = \omega_6$ (3.4) $\omega_1 = \omega_4, \omega_3 = \omega_6, \omega_5 = \omega_2$

  (3.5) $\omega_1 = \omega_6, \omega_3 = \omega_2, \omega_5 = \omega_4$ (3.6) $\omega_1 = \omega_6, \omega_3 = \omega_4, \omega_5 = \omega_2$

Here we only give the procedure for calculating (3.1).

$$\mathrm{E}^{(3.1)}\left\{\xi_m \xi_n^* \xi_k \xi_{m'}^* \xi_{n'} \xi_{k'}^*\right\}$$

$$= f_0^3 \mathcal{P}_{mnkm'n'k'} \mathrm{E}^3\left\{|b|^2\right\} \sum_{\omega_1=0}^{W-1} e^{-j\frac{2\pi}{W}\omega_1(m-n)} \sum_{\omega_3=0}^{W-1} e^{-j\frac{2\pi}{W}\omega_3(k-m')} \sum_{\omega_5=0}^{W-1} e^{-j\frac{2\pi}{W}\omega_5(n'-k')}$$

$$= f_0^3 \mathcal{P}_{mnkm'n'k'} \mathrm{E}^3\left\{|b|^2\right\} \left(W^3 \delta_{m-n+pW} \delta_{k-m'+pW} \delta_{n'-k'+pW}\right.$$

$$-W^2 \delta_{m-n+pW} \delta_{k-m'+n'-k'+pW} - W^2 \delta_{k-m'+pW} \delta_{m-n+n'-k'+pW}$$

$$\left.-W^2 \delta_{n'-k'+pW} \delta_{m-n+k-m'+pW} + 2W\delta_{m-n+k-m'+n'-k'+pW}\right)_{p=0,\pm1,\dots}$$ (3A-11)

$$= R_s^3 \mathcal{P}_{mnkm'n'k'} \mathrm{E}^3\left\{|b|^2\right\} \left(\delta_{m-n+pW} \delta_{k-m'+pW} \delta_{n'-k'+pW}\right)_{p=0,\pm1,\dots}$$

$$-R_s^2 f_0 \mathcal{P}_{mnkm'n'k'} \mathrm{E}^3\left\{|b|^2\right\} \cdot \left(\delta_{m-n+pW} \delta_{k-m'+n'-k'+pW}\right.$$

$$\left.+\delta_{k-m'+pW} \delta_{m-n+n'-k'+pW} + \delta_{n'-k'+pW} \delta_{m-n+k-m'+pW}\right)_{p=0,\pm1,\dots}$$

$$+2R_s f_0^2 \mathcal{P}_{mnkm'n'k'} \mathrm{E}^3\left\{|b|^2\right\} \left(\delta_{m-n+k-m'+n'-k'+pW}\right)_{p=0,\pm1,\dots}$$

Putting all contributions together, we can get:

$$\mathrm{E}\left\{\xi_m \xi_n^* \xi_k \xi_{m'}^* \xi_{n'} \xi_{k'}^*\right\}$$

$$= R_s f_0^2 \mathrm{E}^3\left\{|b|^2\right\}\left[\mathrm{E}\left\{|b|^6\right\}\Big/\mathrm{E}^3\left\{|b|^2\right\} - 9\,\mathrm{E}\left\{|b|^4\right\}\Big/\mathrm{E}^2\left\{|b|^2\right\} + 12\right]$$

$$\cdot \mathcal{P}_{mnkm'n'k'}\left(\delta_{m-n+k-m'+n'-k'+pW}\right)_{p=0,\pm 1,\ldots} + R_s^2 f_0 \mathrm{E}^3\left\{|b|^2\right\}$$

$$\cdot\left[\mathrm{E}\left\{|b|^4\right\}\Big/\mathrm{E}^2\left\{|b|^2\right\} - 2\right]\mathcal{P}_{mnkm'n'k'}\left(\delta_{m-n+pW}\delta_{k-m'+n'-k'+pW}\right.$$

$$+\delta_{m-m'+pW}\delta_{k-n+n'-k'+pW} + \delta_{m-k'+pW}\delta_{k-n-m'+n'+pW}$$

$$+\delta_{k-n+pW}\delta_{m-m'+n'-k'+pW} + \delta_{k-m'+pW}\delta_{m-n+n'-k'+pW}$$

$$+\delta_{k-k'+pW}\delta_{m-n-m'+n'+pW} + \delta_{n'-n+pW}\delta_{m+k-m'-k'+pW}$$

$$+\delta_{n'-m'+pW}\delta_{m-n+k-k'+pW} + \delta_{n'-k'+pW}\delta_{m-n+k-m'+pW}\Big)_{p=0,\pm 1,\ldots}$$

$$+R_s^3 \mathrm{E}^3\left\{|b|^2\right\}\mathcal{P}_{mnkm'n'k'}\left(\delta_{m-n+pW}\delta_{k-m'+pW}\delta_{n'-k'+pW}\right.$$

$$+\delta_{m-n+pW}\delta_{k-k'+pW}\delta_{n'-m'+pW} + \delta_{m-m'+pW}\delta_{k-n+pW}\delta_{n'-k'+pW}$$

$$+\delta_{m-m'+pW}\delta_{k-k'+pW}\delta_{n'-n+pW} + \delta_{m-k'+pW}\delta_{k-n+pW}\delta_{n'-m'+pW}$$

$$+\delta_{m-k'+pW}\delta_{k-m'+pW}\delta_{n'-n+pW}\Big)_{p=0,\pm 1,\ldots} \tag{3A-12}$$

If we choose ideally rectangular spectrum, the parameter p is equal to 0. In this thesis we assume that the channels are rectangular or almost rectangular and neglect the contribution of the terms arising when $p \neq 0$. Investigating the impact of this approximation, when channel spectra are significantly far from rectangular, is left for future investigation.

Appendix 3B: Derivation of XCI formulas

In frequency-domain, the signal model for two channels (dual polarization), i.e., the CUT and one INT channel, can be written as:

$$\vec{E}(f) = \left(E_{\mathrm{CUT},x}(f) + E_{\mathrm{INT},x}(f)\right)\hat{x} + \left(E_{\mathrm{CUT},y}(f) + E_{\mathrm{INT},y}(f)\right)\hat{y} \tag{3B-1}$$
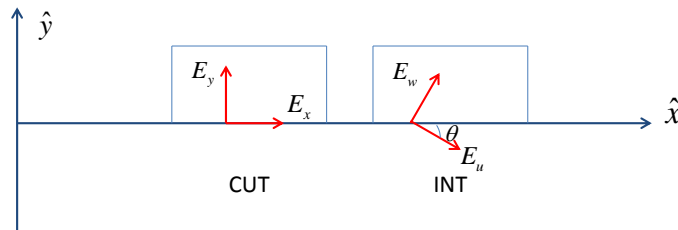

Fig. B-1: The fields in CUT and INT channels.

As a general investigation, we considered there was an angle, $0 \le \theta \le 90°$, between the

polarizations of CUT and INT, as shown in Fig. B-1, the fields in both INT and CUT can be expressed as,

$$E_{\mathrm{CUT},x}(f) = \sqrt{f_0}\sum_{n=-\infty}^{+\infty} v_{x,n}\delta(f - nf_0)$$

$$E_{\mathrm{CUT},y}(f) = \sqrt{f_0}\sum_{n=-\infty}^{+\infty} v_{y,n}\delta(f - nf_0)$$

(3B-2)

$$
\begin{aligned}
E_{\mathrm{INT},x}(f) &= \cos(\theta)E_{\mathrm{INT},u}(f) + \sin(\theta)E_{\mathrm{INT},w}(f) \\
&= \sqrt{f_0}\sum_{n=-\infty}^{+\infty}\left(\xi_{u,n}\cos(\theta) + \xi_{w,n}\sin(\theta)\right)\delta(f - \Delta f - nf_0) \\
&= \sqrt{f_0}\sum_{n=-\infty}^{+\infty}\xi_{x,n}\delta(f - \Delta f - nf_0)
\end{aligned}
$$

$$
\begin{aligned}
E_{\mathrm{INT},y}(f) &= -\sin(\theta)E_{\mathrm{INT},u}(f) + \cos(\theta)E_{\mathrm{INT},w}(f) \\
&= \sqrt{f_0}\sum_{n=-\infty}^{+\infty}\left(-\sin(\theta)\xi_{u,n} + \cos(\theta)\xi_{w,n}\right)\delta(f - \Delta f - nf_0) \\
&= \sqrt{f_0}\sum_{n=-\infty}^{+\infty}\xi_{y,n}\delta(f - \Delta f - nf_0)
\end{aligned}
$$

(3B-3)

The RVs $v_{x,n}$, $v_{y,n}$, $\xi_{u,n}$ and $\xi_{w,n}$ are defined similar to [15]:, Appendix B, Eq. (36):

$$v_{x,n} = \sqrt{f_0}\,s_{\mathrm{CUT},x}(nf_0)\sum_{\omega=0}^{W-1} a_{x,\omega}e^{-j\frac{2\pi}{W}\omega n}$$

$$v_{y,n} = \sqrt{f_0}\,s_{\mathrm{CUT},y}(nf_0)\sum_{\omega=0}^{W-1} a_{y,\omega}e^{-j\frac{2\pi}{W}\omega n}$$

(3B-4)

$$\xi_{u,n} = \sqrt{f_0}\,s_{\mathrm{INT},u}(\Delta f + nf_0)\sum_{\omega=0}^{W-1} b_{u,\omega}e^{-j\frac{2\pi}{W}\omega n}$$

$$\xi_{w,n} = \sqrt{f_0}\,s_{\mathrm{INT},w}(\Delta f + nf_0)\sum_{\omega=0}^{W-1} b_{w,\omega}e^{-j\frac{2\pi}{W}\omega n}$$

(3B-5)

$$\xi_{x,n} = \xi_{u,n}\cos(\theta) + \xi_{w,n}\sin(\theta)$$

$$\xi_{y,n} = -\sin(\theta)\xi_{u,n} + \cos(\theta)\xi_{w,n}$$

(3B-6)

where W is an integer number that can be chosen to be arbitrarily large.

Using the ME, the Kerr term at the fiber input on the x polarization can be written as:

$$Q_{\text{NLI},x}\left(0,f\right) = -j\gamma\frac{8}{9}f_0^{3/2}\sum_{i=-\infty}^{+\infty}\delta\left(f-if_0\right)$$

$$\left[\sum_{S_i}\left(v_{x,m}v_{x,n}^*v_{x,k}+v_{x,m}v_{y,n}^*v_{y,k}\right)\right.$$

$$+\sum_{X1_i}\left(2v_{x,m}\xi_{x,n}^*\xi_{x,k}+v_{y,m}\xi_{y,n}^*\xi_{x,k}+v_{x,m}\xi_{y,n}^*\xi_{y,k}\right)$$

$$+\sum_{X2_i}\left(2\xi_{x,m}v_{x,n}^*v_{x,k}+\xi_{x,m}v_{y,n}^*v_{y,k}+\xi_{y,m}v_{y,n}^*v_{x,k}\right)$$

$$+\sum_{X3_i}\left(v_{x,m}\xi_{x,n}^*v_{x,k}+v_{y,m}\xi_{y,n}^*v_{x,k}\right)$$

$$+\sum_{X4_i}\left(\xi_{x,m}\xi_{x,n}^*\xi_{x,k}+\xi_{y,m}\xi_{y,n}^*\xi_{x,k}\right)$$

$$\left.+\sum_{X5_i}\left(\xi_{x,m}v_{x,n}^*\xi_{x,k}+\xi_{y,m}v_{y,n}^*\xi_{x,k}\right)\right] \tag{3B-7}$$

where:

$$X1_i \equiv S_i \equiv \left\{(m,n,k):(m-n+k)f_0=if_0\right\}$$
$$X2_i \equiv X4_i \equiv \left\{(m,n,k):(m-n+k)f_0+f_c=if_0\right\} \tag{3B-8}$$
$$X3_i \equiv \left\{(m,n,k):(m-n+k)f_0-f_c=if_0\right\}$$
$$X5_i \equiv \left\{(m,n,k):(m-n+k)f_0+2f_c=if_0\right\}$$

The first summation in the $Q_{\text{NLI},x}\left(0,f\right)$ formula is SCI. The summation related to the index set X5 is always zero, as long as the channels do not spectrally overlap, i.e., as long as their separation is greater than R_s. We considered the spectral overlap case outside of the scope of this thesis and therefore from now on we removed the summation related to X5.

Specifically, set X5 is generated by, $mf_0, kf_0 \in \text{INT}, nf_0 \in \text{CUT}$. It must be that $if_0 = mf_0 + kf_0 - nf_0 \in \text{CUT}$. In this thesis, the bandwidth of each channel is equal to symbol rate R_s, and the central frequency of the INT is f_c, with ($f_c \geq R_s$). Therefore, we can write:

$$f_c - \frac{R_s}{2} \leq mf_0 \leq f_c + \frac{R_s}{2}$$
$$f_c - \frac{R_s}{2} \leq kf_0 \leq f_c + \frac{R_s}{2} \tag{3B-9}$$
$$-\frac{R_s}{2} \leq nf_0 \leq +\frac{R_s}{2}$$

Combining these inequalities we get:

$$2f_c - \frac{3R_s}{2} \le mf_0 + kf_0 - nf_0 \le 2f_c + \frac{3R_s}{2} \tag{3B-10}$$

Assuming $f_c > 0$, we can then remark that $2f_c - 3R_s/2 \ge R_s/2$, so that we can write:

$$\frac{R_s}{2} \le mf_0 + kf_0 - nf_0 = if_0 \tag{3B-11}$$

where "=" holds only for $f_c = R_s$. Therefore, $if_0 \notin \text{CUT}$ and the contribution of the set X5 is zero. A similar conclusion can be found when assuming $f_c < 0$.

The resulting NLI field for the XCI component only, after a homogenous span of length L_s, can be written as:

$$
\begin{aligned}
&E_{\text{XCI},x}\left(L_s, f\right) \\
&= -j\frac{8}{9} f_0^{3/2} e^{-\alpha L_s} e^{-j2\beta_2 \pi^2 i^2 f_0^2 L_s} \sum_{i=-\infty}^{+\infty} \delta\left(f - if_0\right) \\
&\left[\sum_{\text{X1}_i} \zeta\left(k, m-\tfrac{\Delta f}{f_0}, n\right)\cdot\left(2v_{x,m}\xi_{x,n}^*\xi_{x,k} + v_{y,m}\xi_{y,n}^*\xi_{x,k} + v_{x,m}\xi_{y,n}^*\xi_{y,k}\right) \right. \\
&+ \sum_{\text{X2}_i} \zeta\left(k, m+\tfrac{\Delta f}{f_0}, n\right)\cdot\left(2\xi_{x,m}v_{x,n}^*v_{x,k} + \xi_{x,m}v_{y,n}^*v_{y,k} + \xi_{y,m}v_{y,n}^*v_{x,k}\right) \\
&+ \sum_{\text{X3}_i} \zeta\left(k-\tfrac{\Delta f}{f_0}, m-\tfrac{\Delta f}{f_0}, n\right)\cdot\left(v_{x,m}\xi_{x,n}^*v_{x,k} + v_{y,m}\xi_{y,n}^*v_{x,k}\right) \\
&\left. + \sum_{\text{X4}_i} \zeta\left(k, m, n\right)\cdot\left(\xi_{x,m}\xi_{x,n}^*\xi_{x,k} + \xi_{y,m}\xi_{y,n}^*\xi_{x,k}\right) \right]
\end{aligned}
\tag{3B-12}
$$

where ζ is defined as in Eq. (3-10). By "homogeneous span" we mean that the fiber parameters are constant over the length L_s.

As for the field on the *y* polarization, it can be found by swapping the subscripts *x* and *y*. Therefore the total XCI PSD is:

$$G_{\text{XCI}}^{\text{EGN}}\left(f\right) = G_{\text{X1}_i}\left(f\right) + G_{\text{X2}_i}\left(f\right) + G_{\text{X3}_i}\left(f\right) + G_{\text{X4}_i}\left(f\right) \tag{3B-13}$$

Since the only difference between these contributions is the cross-moments among six random variables, we just give the detailed derivation of the first contribution from set X1$_i$, which is related to the integration region X1 in Fig. 3-3.

In region X1, the XCI PSD is,

$$G_{\text{X1}_i}\left(f\right) = G_{\text{X1}_i,x}\left(f\right) + G_{\text{X1}_i,y}\left(f\right) \tag{3B-14}$$

where:

$$
\begin{aligned}
G_{\mathrm{X1}_i,x}\left(f\right) = &\frac{64}{81} f_0^3 e^{-2\alpha L_s} \sum_{i=-\infty}^{+\infty} \delta\left(f-if_0\right) \sum_{m,n,k\in\mathrm{X1}_i} \sum_{m',n',k'\in\mathrm{X1}_i} \\
&\zeta\left(k,m-\tfrac{\Delta f}{f_0},n\right)\zeta^*\left(k',m'-\tfrac{\Delta f}{f_0},n'\right) \\
&\Big[4\mathrm{E}\left\{v_{x,m}v_{x,m'}^*\right\}\mathrm{E}\left\{\xi_{x,n}^*\xi_{x,k}\xi_{x,n'}\xi_{x,k'}^*\right\} \\
&+\mathrm{E}\left\{v_{y,m}v_{y,m'}^*\right\}\mathrm{E}\left\{\xi_{x,k}\xi_{x,k'}^*\right\}\mathrm{E}\left\{\xi_{y,n}^*\xi_{y,n'}\right\} \\
&+\mathrm{E}\left\{v_{x,m}v_{x,m'}^*\right\}\mathrm{E}\left\{\xi_{y,n}^*\xi_{y,k}\xi_{y,n'}\xi_{y,k'}^*\right\} \\
&+2\mathrm{E}\left\{v_{x,m}v_{x,m'}^*\right\}\mathrm{E}\left\{\xi_{x,n'}\xi_{x,k'}^*\right\}\mathrm{E}\left\{\xi_{y,n}^*\xi_{y,k}\right\}\Big]
\end{aligned}
\tag{3B-15}
$$

Substituting Eq. (3B-6) into (3B-15), we can get:

$$
\begin{aligned}
G_{\mathrm{X1}_i,x}\left(f\right) = &\frac{64}{81} f_0^3 e^{-2\alpha L_s} \sum_{i=-\infty}^{+\infty} \delta\left(f-if_0\right) \sum_{m,n,k\in\mathrm{X1}_i} \sum_{m',n',k'\in\mathrm{X1}_i} \\
&\zeta\left(k,m-\tfrac{\Delta f}{f_0},n\right)\zeta^*\left(k',m'-\tfrac{\Delta f}{f_0},n'\right) \\
&\Big[\mathrm{E}\left\{v_{x,m}v_{x,m'}^*\right\}\mathrm{E}\left\{\xi_{u,n}^*\xi_{u,k}\xi_{u,n'}\xi_{u,k'}^*\right\}\left(1+\cos^2\left(\theta\right)\right)^2 \\
&+\mathrm{E}\left\{v_{x,m}v_{x,m'}^*\right\}\mathrm{E}\left\{\xi_{u,n}^*\xi_{u,n'}\right\}\mathrm{E}\left\{\xi_{w,k}\xi_{w,k'}^*\right\}\sin^2\left(\theta\right)\cos^2\left(\theta\right) \\
&+\mathrm{E}\left\{v_{x,m}v_{x,m'}^*\right\}\mathrm{E}\left\{\xi_{u,k}\xi_{u,k'}^*\right\}\mathrm{E}\left\{\xi_{w,n}^*\xi_{w,n'}\right\}\sin^2\left(\theta\right)\cos^2\left(\theta\right) \\
&+\mathrm{E}\left\{v_{x,m}v_{x,m'}^*\right\}\mathrm{E}\left\{\xi_{w,n}^*\xi_{w,k}\xi_{w,n'}\xi_{w,k'}^*\right\}\left(1+\sin^2\left(\theta\right)\right)^2 \\
&+\mathrm{E}\left\{v_{y,m}v_{y,m'}^*\right\}\mathrm{E}\left\{\xi_{u,n}^*\xi_{u,k}\xi_{u,n'}\xi_{u,k'}^*\right\}\sin^2\left(\theta\right)\cos^2\left(\theta\right) \\
&+\mathrm{E}\left\{v_{y,m}v_{y,m'}^*\right\}\mathrm{E}\left\{\xi_{u,k}\xi_{u,k'}^*\right\}\mathrm{E}\left\{\xi_{w,n}^*\xi_{w,n'}\right\}\cos^4\left(\theta\right) \\
&+\mathrm{E}\left\{v_{y,m}v_{y,m'}^*\right\}\mathrm{E}\left\{\xi_{u,n}^*\xi_{u,n'}\right\}\mathrm{E}\left\{\xi_{w,k}\xi_{w,k'}^*\right\}\sin^4\left(\theta\right) \\
&+\mathrm{E}\left\{v_{y,m}v_{y,m'}^*\right\}\mathrm{E}\left\{\xi_{w,n}^*\xi_{w,k}\xi_{w,n'}\xi_{w,k'}^*\right\}\sin^2\left(\theta\right)\cos^2\left(\theta\right)\Big]
\end{aligned}
\tag{3B-16}
$$

We calculated these special expectations according to the formulas given in Appendix 3A, and we removed the terms with $k=n$ or $k'=n'$ because they can be shown to contribute a frequency-flat, constant phase shift which has no detrimental effect on transmission. In addition, we assume that:

$$
\mathrm{E}\left\{\left|a_x\right|^2\right\}=\mathrm{E}\left\{\left|a_y\right|^2\right\}=\frac{1}{2}\mathrm{E}\left\{\left|a\right|^2\right\} \quad , \quad \mathrm{E}\left\{\left|b_x\right|^2\right\}=\mathrm{E}\left\{\left|b_y\right|^2\right\}=\frac{1}{2}\mathrm{E}\left\{\left|b\right|^2\right\}
\tag{3B-17}
$$

$$
s_{\mathrm{CUT},x}\left(f\right)=s_{\mathrm{CUT},y}\left(f\right)=s_{\mathrm{CUT}}\left(f\right) \quad , \quad s_{\mathrm{INT},u}\left(f\right)=s_{\mathrm{INT},w}\left(f\right)=s_{\mathrm{INT}}\left(f\right)
\tag{3B-18}
$$

Consequently, we can rewrite Eq. (3B-15)as:

$$
\begin{aligned}
G_{\mathrm{X1}_{i},x}\left(f\right) ={}& \frac{8}{81} f_0^3 e^{-2\alpha L_s} \mathrm{E}\left\{|a|^2\right\} \mathrm{E}^2\left\{|b|^2\right\} \sum_{i=-\infty}^{+\infty} \delta\left(f - i f_0\right) \\
& \sum_{m,n,k \in \mathrm{X1}_i} \sum_{m',n',k' \in \mathrm{X1}_i} \zeta\left(k, m - \tfrac{\Delta f}{f_0}, n\right) \zeta^*\left(k', m' - \tfrac{\Delta f}{f_0}, n'\right) \\
& \left[\left\{ \left(1 + \cos^2\left(\theta\right)\right)^2 + \left(1 + \sin^2\left(\theta\right)\right)^2 + 4\sin^2\left(\theta\right)\cos^2\left(\theta\right) \right.\right. \\
& \left.+ \sin^4\left(\theta\right) + \cos^4\left(\theta\right) \right\} R_s^3 \mathcal{P}_{\mathrm{INT}} \delta_{k-k'} \delta_{n'-n} \\
& + \left\{ \left(1 + \cos^2\left(\theta\right)\right)^2 + \left(1 + \sin^2\left(\theta\right)\right)^2 + 2\sin^2\left(\theta\right)\cos^2\left(\theta\right) \right\} \\
& \left. \cdot R_s^2 f_0 \left[\mathrm{E}\left\{|b|^4\right\} \Big/ \mathrm{E}^2\left\{|b|^2\right\} - 2 \right] \mathcal{P}_{\mathrm{INT}} \delta_{m-m'} \delta_{k-n-k'+n'} \right]
\end{aligned}
\tag{3B-19}
$$

where:

$$
\begin{aligned}
\mathcal{P}_{\mathrm{INT}} ={}& s_{\mathrm{CUT}}\left(m f_0\right) s_{\mathrm{INT}}^*\left(\Delta f + n f_0\right) s_{\mathrm{INT}}\left(\Delta f + k f_0\right) \\
& \cdot s_{\mathrm{CUT}}^*\left(m' f_0\right) s_{\mathrm{INT}}\left(\Delta f + n' f_0\right) s_{\mathrm{INT}}^*\left(\Delta f + k' f_0\right)
\end{aligned}
\tag{3B-20}
$$

Furthermore, we figure out that:

$$
\begin{aligned}
& \left\{ \left(1 + \cos^2\left(\theta\right)\right)^2 + \left(1 + \sin^2\left(\theta\right)\right)^2 + 4\sin^2\left(\theta\right)\cos^2\left(\theta\right) + \sin^4\left(\theta\right) + \cos^4\left(\theta\right) \right\} \\
&= 2 + 2\left(\cos^2\left(\theta\right) + \sin^2\left(\theta\right)\right) + 4\sin^2\left(\theta\right)\cos^2\left(\theta\right) + 2\sin^4\left(\theta\right) + 2\cos^4\left(\theta\right) \\
&= 2 + 2 + 2\sin^2(\theta) + 2\cos^2(\theta) = 6
\end{aligned}
\tag{3B-21}
$$

$$
\begin{aligned}
& \left\{ \left(1 + \cos^2\left(\theta\right)\right)^2 + \left(1 + \sin^2\left(\theta\right)\right)^2 + 2\sin^2\left(\theta\right)\cos^2\left(\theta\right) \right\} \\
&= 2 + 2\left(\cos^2\left(\theta\right) + \sin^2\left(\theta\right)\right) + \left(\sin^2\left(\theta\right) + \cos^2\left(\theta\right)\right)^2 = 5
\end{aligned}
\tag{3B-22}
$$

Therefore, Eq. (3B-19) can be simplified as:

$$
\begin{aligned}
G_{\mathrm{X1}_{i},x}\left(f\right) ={}& \frac{8}{81} f_0^3 e^{-2\alpha L_s} \mathrm{E}\left\{|a|^2\right\} \mathrm{E}^2\left\{|b|^2\right\} \sum_{i=-\infty}^{+\infty} \delta\left(f - i f_0\right) \\
& \sum_{m,n,k \in \mathrm{X1}_i} \sum_{m',n',k' \in \mathrm{X1}_i} \zeta\left(k, m - \tfrac{\Delta f}{f_0}, n\right) \zeta^*\left(k', m' - \tfrac{\Delta f}{f_0}, n'\right) \\
& \left\{ 6 R_s^3 \mathcal{P}_{\mathrm{INT}}\, \delta_{m-m'} \delta_{k-k'} \delta_{n'-n} \right. \\
& \left. + 5 R_s^2 f_0 \left[\mathrm{E}\left\{|b|^4\right\} \Big/ \mathrm{E}^2\left\{|b|^2\right\} - 2 \right] \mathcal{P}_{\mathrm{INT}} \delta_{m-m'} \delta_{k-n-k'+n'} \right\}
\end{aligned}
\tag{3B-23}
$$

which demonstrates that the angle θ has no impact on the final expression.

As for $G_{X1_i,y}(f)$, it is identical to $G_{X1_i,x}(f)$. Therefore, the XCI PSD in X1 is,

$$G_{X1_i}(f) = E\{|a|^2\} E^2\{|b|^2\}\left[\chi_1(f) - \Phi_b\,\chi_2(f)\right] \tag{3B-24}$$

where:

$$
\begin{aligned}
\chi_1(f) &= \frac{16}{81}f_0^3 e^{-2\alpha L_s}\sum_{i=-\infty}^{+\infty}\delta(f-if_0)\sum_{m,n,k\in X1_i}\sum_{m',n',k'\in X1_i}\\
&\quad \zeta\left(k,m-\tfrac{\Delta f}{f_0},n\right)\zeta^*\left(k',m'-\tfrac{\Delta f}{f_0},n'\right)\cdot 6R_s^3\mathcal{P}_{\text{INT}}\delta_{m-m'}\delta_{k-k'}\delta_{n'-n}\\
&= \frac{32}{27}f_0^3 e^{-2\alpha L_s}R_s^3\sum_{i=-\infty}^{+\infty}\delta(f-if_0)\sum_m\sum_k\left|s_{\text{CUT}}(mf_0)\right|^2\\
&\quad \left|s_{\text{INT}}(\Delta f+kf_0)\right|^2\left|s_{\text{INT}}(\Delta f+[m+k-i]f_0)\right|^2\left|\zeta\left(m,k+\tfrac{\Delta f}{f_0},i\right)\right|^2
\end{aligned}
\tag{3B-25}
$$

$$
\begin{aligned}
\chi_2(f) &= \frac{16}{81}f_0^3 e^{-2\alpha L_s}\sum_{i=-\infty}^{+\infty}\delta(f-if_0)\sum_{m,n,k\in X1_i}\sum_{m',n',k'\in X1_i}\\
&\quad \zeta\left(k,m-\tfrac{\Delta f}{f_0},n\right)\zeta^*\left(k',m'-\tfrac{\Delta f}{f_0},n'\right)\cdot 5R_s^2 f_0\mathcal{P}_{\text{INT}}\delta_{m-m'}\delta_{k-n-k'+n'}\\
&= \frac{80}{81}f_0^4 e^{-2\alpha L_s}R_s^2\sum_{i=-\infty}^{+\infty}\delta(f-if_0)\sum_m\sum_k\sum_{k'}\left|s_{\text{CUT}}(mf_0)\right|^2\\
&\quad s_{\text{INT}}(\Delta f+kf)s_{\text{INT}}^*(\Delta f+k'f_0)s_{\text{INT}}^*(\Delta f+[m+k-i]f_0)\\
&\quad s_{\text{INT}}(\Delta f+[m+k'-i]f_0)\zeta\left(m,k+\tfrac{\Delta f}{f_0},i\right)\zeta^*\left(m,k'+\tfrac{\Delta f}{f_0},i\right)
\end{aligned}
\tag{3B-26}
$$

   If identical spans using the same fiber type are assumed, with lumped amplifiers exactly compensating for the loss of each span, the XCI PSD is then:

$$G_{X1_i}(f) = E\{|a|^2\} E^2\{|b|^2\}\left[\kappa_1(f) - \Phi_b\,\kappa_2(f)\right] \tag{3B-27}$$

where:

$$
\begin{aligned}
\kappa_1(f) &= \frac{32}{27}f_0^3 R_s^3\sum_{i=-\infty}^{+\infty}\delta(f-if_0)\sum_m\sum_k\left|s_{\text{CUT}}(mf_0)\right|^2\\
&\quad \left|s_{\text{INT}}(\Delta f+kf_0)\right|^2\left|s_{\text{INT}}(\Delta f+[m+k-i]f_0)\right|^2\left|\mu\left(m,k+\tfrac{\Delta f}{f_0},i\right)\right|^2
\end{aligned}
\tag{3B-28}
$$

$$\kappa_2(f) = \frac{80}{81} f_0^4 R_s^2 \sum_{i=-\infty}^{+\infty} \delta(f - if_0) \sum_m \sum_k \sum_{k'} \left| s_{\mathrm{CUT}}(mf_0) \right|^2$$

$$s_{\mathrm{INT}}(\Delta f + kf_0) s_{\mathrm{INT}}^*(\Delta f + [m+k-i]f_0) s_{\mathrm{INT}}^*(\Delta f + k'f_0) \qquad (3B\text{-}29)$$

$$s_{\mathrm{INT}}(\Delta f + [m+k'-i]f_0) \mu\left(m, k + \tfrac{\Delta f}{f_0}, i\right) \mu^*\left(m, k' + \tfrac{\Delta f}{f_0}, i\right)$$

Then transiting to integral form, we can get the final formulas shown in Sect. 3.1.2.2. As for the other contributions, they can be calculated through the same procedure, and related to different integration regions in Fig. 3-3. $G_{X2_i}(f)$, $G_{X3_i}(f)$ and $G_{X4_i}(f)$ are induced by the integration regions X2, X3 and X4 respectively.

Appendix 3C: Analytical complexity of the EGN model terms

As shown in Sect. 3.1, the EGN model consists of a GN model term and a "correction term". All the contributions making up the GN model term consist of double integrals over f_1, f_2. The contributions of the EGN model correction term are instead expressed as either triple or quadruple integrals. This seems to suggest that the numerical integration of the correction contributions may be quite challenging.

In reality, the correction contributions can be shown to always require only a double integral to be evaluated. For instance, one of the correction terms for SCI which has a triple integral is Eq. (3-30):

$$\kappa_2(f) = \frac{80}{81} R_s^2 \int_{-R_s/2}^{+R_s/2} df_1 \int_{-R_s/2}^{+R_s/2} df_2 \int_{-R_s/2}^{+R_s/2} df_2' \left| s_{\mathrm{CUT}}(f_1) \right|^2 s_{\mathrm{CUT}}(f_2) s_{\mathrm{CUT}}^*(f_2')$$

$$s_{\mathrm{CUT}}^*(f_1 + f_2 - f) s_{\mathrm{CUT}}(f_1 + f_2' - f) \mu(f_1, f_2, f) \mu^*(f_1, f_2', f) \qquad (3C\text{-}1)$$

$$+ \frac{16}{81} R_s^2 \int_{-R_s/2}^{+R_s/2} df_1 \int_{-R_s/2}^{+R_s/2} df_2 \int_{-R_s/2}^{+R_s/2} df_2' \left| s_{\mathrm{CUT}}(f_1 + f_2 - f) \right|^2 s_{\mathrm{CUT}}(f_1)$$

$$s_{\mathrm{CUT}}(f_2) s_{\mathrm{CUT}}^*(f_1 + f_2 - f_2') s_{\mathrm{CUT}}^*(f_2') \mu(f_1, f_2, f) \mu^*(f_1 + f_2 - f_2', f_2', f)$$

The term preceded by 80/81 in the equation above, which we will call $\kappa_{21}(f)$, can be re-written as:

$$\kappa_{21}(f) = \frac{80}{81} R_s^2 \int\limits_{-R_s/2}^{+R_s/2} df_1 \left| s_{\text{CUT}}(f_1) \right|^2$$

$$\int\limits_{-R_s/2}^{+R_s/2} df_2 s_{\text{CUT}}(f_2) s_{\text{CUT}}^*(f_1 + f_2 - f) \mu(f_1, f_2, f)$$

$$\int\limits_{-R_s/2}^{+R_s/2} df_2' s_{\text{CUT}}^*(f_2') s_{\text{CUT}}(f_1 + f_2' - f) \mu^*(f_1, f_2', f) \qquad \text{(3C-2)}$$

$$= \frac{80}{81} R_s^2 \int\limits_{-R_s/2}^{+R_s/2} df_1 \left| s_{\text{CUT}}(f_1) \right|^2$$

$$\cdot \left| \int\limits_{-R_s/2}^{+R_s/2} df_2 s_{\text{CUT}}(f_2) s_{\text{CUT}}^*(f_1 + f_2 - f) \mu(f_1, f_2, f) \right|^2$$

In other words, the second and third integrals are the same integral, except for a complex conjugation, so that only one integration is needed to obtain both.

For the term preceded by 16/81, which we will call $\kappa_{22}(f)$, we replace the integration variable f_1 with $f_3 = f_1 + f_2 - f$, that is $f_1 = f_3 - f_2 + f$. Then:

$$\kappa_{22}(f) = \frac{16}{81} R_s^2 \int\limits_{-R_s/2}^{+R_s/2} df_3 \int\limits_{-R_s/2}^{+R_s/2} df_2 \int\limits_{-R_s/2}^{+R_s/2} df_2' \left| s_{\text{CUT}}(f_3) \right|^2$$

$$s_{\text{CUT}}(f_3 - f_2 + f) s_{\text{CUT}}(f_2) s_{\text{CUT}}^*(f_3 - f_2' + f)$$

$$s_{\text{CUT}}^*(f_2') \mu(f_3 - f_2 + f, f_2, f) \mu^*(f_3 - f_2' + f, f_2', f)$$

$$= \frac{16}{81} R_s^2 \int\limits_{-R_s/2}^{+R_s/2} df_3 \left| s_{\text{CUT}}(f_3) \right|^2$$

$$\int\limits_{-R_s/2}^{+R_s/2} df_2 s_{\text{CUT}}(f_2) s_{\text{CUT}}(f_3 - f_2 + f) \mu(f_3 - f_2 + f, f_2, f)$$

$$\int\limits_{-R_s/2}^{+R_s/2} df_2' s_{\text{CUT}}^*(f_2') s_{\text{CUT}}^*(f_3 - f_2' + f) \mu^*(f_3 - f_2' + f, f_2', f)$$

$$= \frac{16}{81} R_s^2 \int\limits_{-R_s/2}^{+R_s/2} df_3 \left| s_{\text{CUT}}(f_3) \right|^2$$

$$\cdot \left| \int\limits_{-R_s/2}^{+R_s/2} df_2 s_{\text{CUT}}(f_2) s_{\text{CUT}}(f_3 - f_2 + f) \mu(f_3 - f_2 + f, f_2, f) \right|^2 \qquad \text{(3C-3)}$$

Again, the second and third integrals are the same integral, except for a complex conjugation, so that only one integration is actually needed to obtain both.

One of the correction terms for SCI has a quadruple integral Eq. (3-31):

$$\kappa_3(f) = \frac{16}{81}R_s \int\limits_{-R_s/2}^{+R_s/2} df_1 \int\limits_{-R_s/2}^{+R_s/2} df_2 \int\limits_{-R_s/2}^{+R_s/2} df_1' \int\limits_{-R_s/2}^{+R_s/2} df_2'$$

$$s_{\text{CUT}}(f_1)s_{\text{CUT}}(f_2)s_{\text{CUT}}^*(f_1+f_2-f)s_{\text{CUT}}^*(f_1')$$

$$s_{\text{CUT}}^*(f_2')s_{\text{CUT}}(f_1'+f_2'-f)\mu(f_1,f_2,f)\mu^*(f_1',f_2',f)$$

$$= \frac{16}{81}R_s \int\limits_{-R_s/2}^{+R_s/2} df_1 \int\limits_{-R_s/2}^{+R_s/2} df_2 s_{\text{CUT}}(f_1)s_{\text{CUT}}(f_2)s_{\text{CUT}}^*(f_1+f_2-f)\mu(f_1,f_2,f) \qquad (3C\text{-}4)$$

$$\int\limits_{-R_s/2}^{+R_s/2} df_1' \int\limits_{-R_s/2}^{+R_s/2} df_2' s_{\text{CUT}}^*(f_1')s_{\text{CUT}}^*(f_2')s_{\text{CUT}}(f_1'+f_2'-f)\mu^*(f_1',f_2',f)$$

$$= \frac{16}{81}R_s \left| \int\limits_{-R_s/2}^{+R_s/2} df_1 \int\limits_{-R_s/2}^{+R_s/2} df_2 s_{\text{CUT}}(f_1)s_{\text{CUT}}(f_2)s_{\text{CUT}}^*(f_1+f_2-f)\mu(f_1,f_2,f) \right|^2$$

Here, it turns out that the first two integrals together are the complex conjugate of the third and fourth, so that a double integration only is needed to assess the whole contribution.

Similar manipulations can be used to show that all other EGN model contributions, (including XCI and MCI) have an inherent complexity that is just that of a double-integral.

This property is clearly important and we exploited it in the numerical evaluation software that we used. It is also possible that more analytical manipulation can be carried out to further reduce the integration complexity. For instance in [17] a hyperbolic variable substitution proved quite effective for the GN model. However, we have not yet carried out a similar investigation for the EGN model and leave this topic for possible future research.

Chapter 4   The EGN model approximation

Although the EGN model is theoretically rigorous, its complexity is substantially larger than that of the GN model, which can make its extensive practical use difficult. Therefore, we proposed a very simple, closed-form correction to the GN model. It is fully derived from the EGN model formulas.

4.1 The closed-form correction formula

Throughout this chapter we assume dual-polarization propagation, over realistic fibers with non-zero loss. The EGN model approximation according to the EGN model is:

$$\hat{G}_{\text{NLI}}^{\text{EGN}}\left(f\right) \approx G_{\text{NLI}}^{\text{GN}}\left(f\right) - \hat{G}_{\text{NLI}}^{\text{corr}} \tag{4-1}$$

where:

$$\hat{G}_{\text{NLI}}^{\text{corr}} = \frac{80}{81}\Phi\frac{\gamma^2 \overline{L}_{\text{eff}}^2 P_{\text{ch}}^3 N_s}{R_s^2 \Delta f \pi \beta_2 \overline{L}_s}\text{HN}\left(\left[N_{\text{ch}}-1\right]/2\right) \tag{4-2}$$

whose derivation is given by other OptCom Group members and is reported in [42]. In this chapter, I provided its validation. The term $\hat{G}_{\text{NLI}}^{\text{corr}}$ is a closed-form correction which approximately corrects the GN model for the errors due to the signal Gaussianity assumption. $\overline{L}_s$ is the average span length. $\overline{L}_{\text{eff}}$ is the average span effective length, with span effective length defined as $L_{\text{eff}} = \left(1 - e^{-2\alpha L_s}\right)/2\alpha$.

In addition, $\text{HN}\left(N\right)$ is the harmonic number series, defined as:

$$\text{HN}\left(N\right) = \sum_{n=1}^{N}\left(1/n\right) \tag{4-3}$$

Finally, Φ is a constant that depends on the modulation format, which is the same as Φ_a shown in Table 3-1.

Eq. (4-2) assumes that:

(1) all channels are identical and equally spaced. This assumption can be removed but this topic will not be dealt with in this chapter.

(2) channels are single-carrier type (neither OFDM nor massively multi-subcarrier).

(3) the same type of fiber is used in all spans. Spans can be of different length,

though: Eq. (4-2) uses the average span length $\bar{L}_s$ and the average span effective length $\bar{L}_{eff}$. Accuracy is quite good for links having all individual span lengths within $\bar{L}_s \pm 15\%$. Caution should be used for larger deviations.

(4) lumped amplification is used to exactly compensate for the loss of the preceding span. Regarding the use of Eq. (4-1) with Raman-amplified systems, see discussion in Sect. 4.4.

Furthermore, Eq. (4-2) has the following limitations:

(1) $\hat{G}_{NLI}^{corr}$ approximately corrects the XCI contributions to NLI. It does not correct the SCI contribution Therefore, the overall Eq. (4-1) is increasingly more accurate as the number of channels is increased, whereas for a single channel system it coincides with the standard GN model. A fully analytical correction for SCI is available as part of the EGN model, but currently not in simple closed-form.

(2) $\hat{G}_{NLI}^{corr}$ is asymptotic in the number of spans. As a result, its accuracy improves as the number of spans grows. The speed of the asymptotic convergence depends on the number of channels and on fiber dispersion .

(3) $\hat{G}_{NLI}^{corr}$ is derived assuming ideally rectangular channel spectra. If spectra have a significantly different shape (such as sinc-shaped), some accuracy may be lost.

(4) $\hat{G}_{NLI}^{corr}$ is calculated at $f = 0$ and then it is assumed to be frequency-flat.

4.2 Validation of the correction formula

As pointed out, $\hat{G}_{NLI}^{corr}$ does not correct the SCI contribution to nonlinearity. Therefore, we focused its specific validation effort on the other two NLI components, XMCI. As a consequence, a straightforward choice for the quantity to focus on for model validation could be:

$$\eta_{XMCI} = P_{ch}^{-3} \int_{-R_s/2}^{R_s/2} G_{XMCI}(f) \, df \qquad (4\text{-}4)$$

The approximate $\hat{G}_{XMCI}(f)$ can be calculated using the EGN model approximation Eq. (4-1) with SCI contribution removed from the GN model term:

$$\hat{G}_{XMCI}(f) \approx G_{NLI}^{GN}(f) - G_{SCI}^{GN}(f) - \hat{G}_{NLI}^{corr} \qquad (4\text{-}5)$$

The first set of results is plotted in Fig. 4-1 and Fig. 4-2, which are the same as Fig. 3-

7 and Fig. 3-10, respectively, with another black curve representing the approximate EGN model Eq. (4-5). Relying on the simple correction Eq. (4-2), the approximate EGN model is quite effective with all fibers, showing good convergence towards the exact EGN model curve and vs. simulations, as the number of spans grows. As a result of its asymptotic behavior, Eq. (4-2) only partially corrects the GN model at low span count. On the other hand, at span counts that are typically of interest for system maximum reach predictions, its accuracy is good. The error vs. either simulations or the EGN model curve is less than 0.4 dB in the whole range 10-50 spans, for all three analyzed fibers. It stays below 0.7 dB even down to only 5 spans, across all cases.

4.2.1 Higher channel count

We wanted to check whether a similarly reliable behavior was maintained at a substantially higher channel count. We looked at 41 channels where, however, we could not run benchmark simulations because of the excessive required computation time. The check is therefore made towards the EGN model curve alone. Fig. 4-3 shows the η_{XMCI} results for the three reference fibers. The very good asymptotic convergence of Eq. (4-2) towards the EGN model is confirmed even at this substantially higher channel count.

4.2.2 Larger channel spacing

To see whether Eq. (4-2) held up at larger channel spacing, we ran checks at 50 GHz spacing, with 9 channels. Fig. 4-4 shows that Eq. (4-2) is asymptotically accurate at this spacing as well, on all three reference fibers.

4.2.3 Shorter span lengths

We also ran a set of checks at a substantially shorter span length L_s =60 km. Fig. 4-5 shows a quite good overall convergence of the approximate EGN estimate, even at relatively low number of spans.
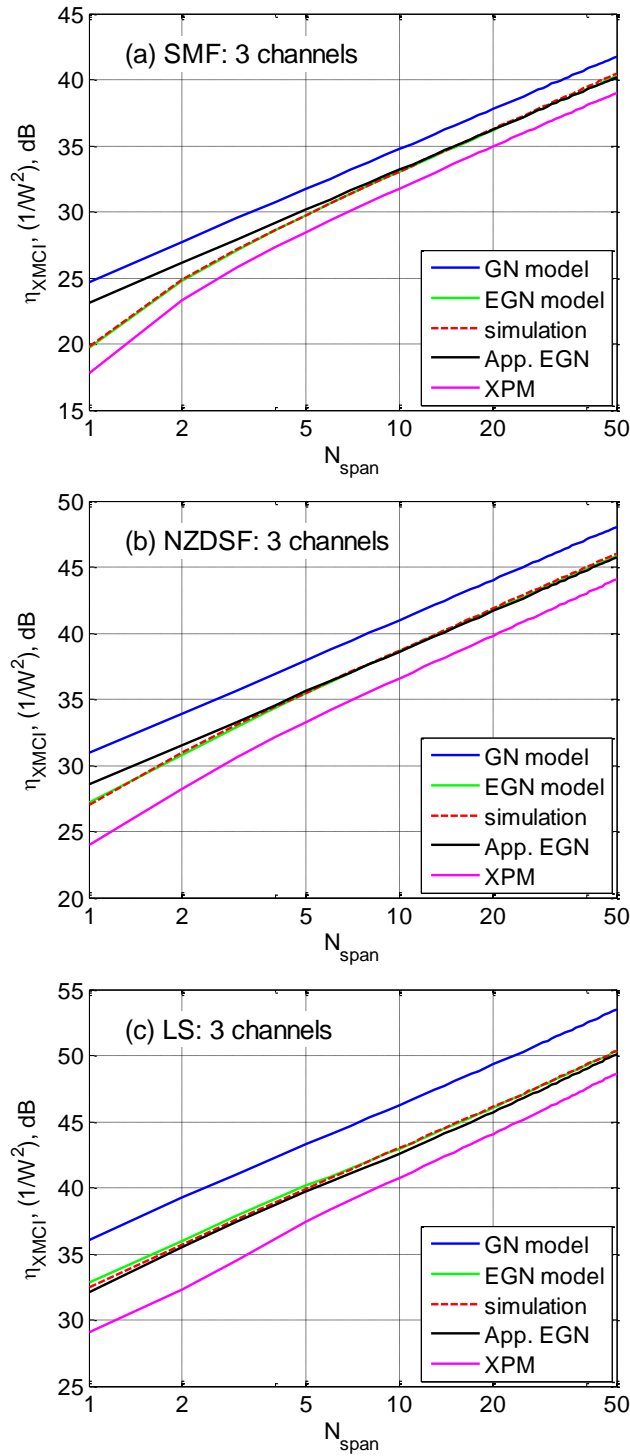
Fig. 4-1: Plot of the normalized nonlinearity coefficient η_{XMCI} vs. number of spans in the link, assuming 3 PM-QPSK channels over SMF, NZDSF and LS, with span length 100 km, at 32 GBaud, roll-off 0.05, span length 100 km, channel spacing 33.6 GHz. SCI effects are completely removed from all curves. The "App. EGN" curve is generated using Eq. (4-5).
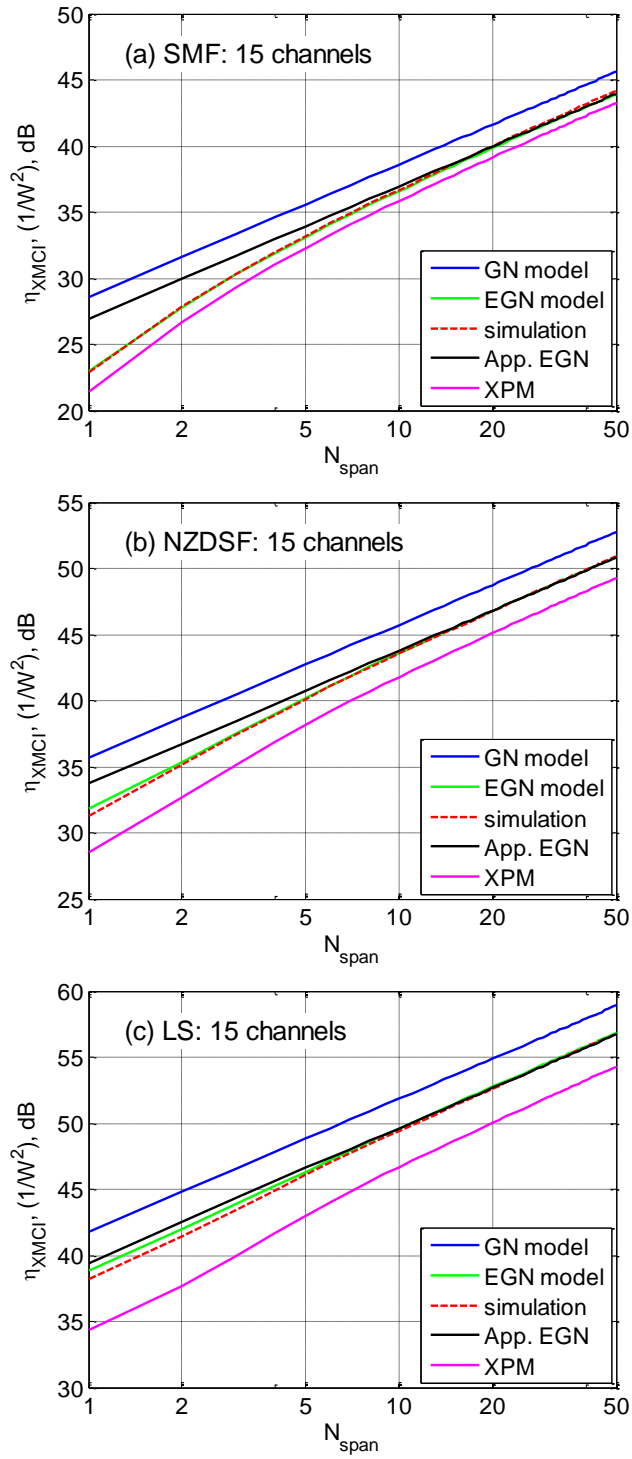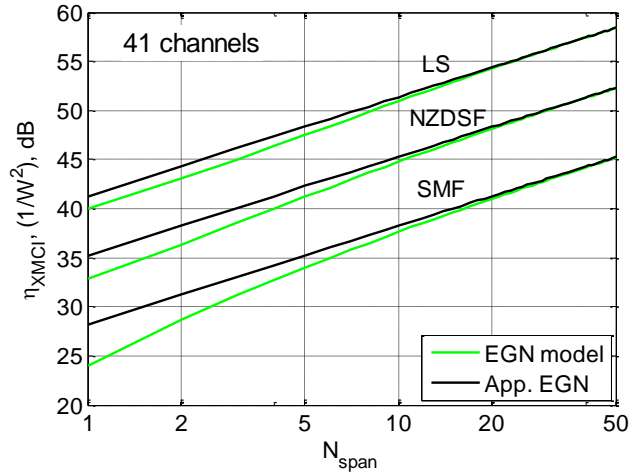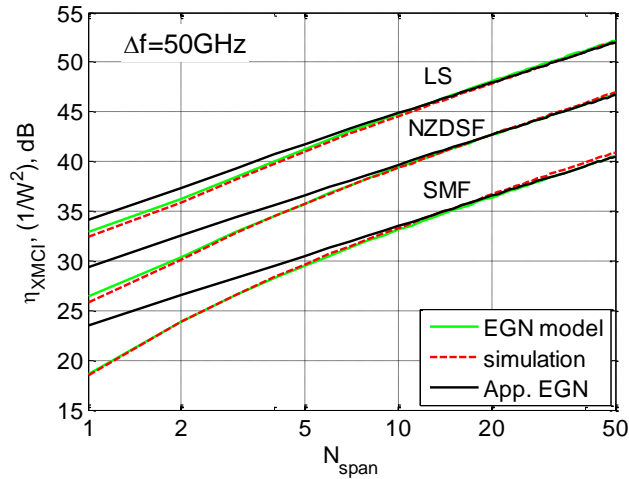
Fig. 4-2: Plot of the normalized nonlinearity coefficient η_{XMCI} vs. number of spans in the link, assuming 15 PM-QPSK channels over SMF, NZDSF and LS, with span length 100 km, at 32 GBaud, roll-off 0.05, span length 100 km, channel spacing 33.6 GHz. SCI effects are completely removed from all curves. The "App. EGN" curve is generated using Eq. (4-5).

Fig. 4-3: Plot of the normalized nonlinearity coefficient η_{XMCI} vs. number of spans in the link, assuming 41 PM-QPSK channels over SMF, NZDSF and LS, with span length 100 km, at 32 GBaud, roll-off 0.05, span length 100 km, channel spacing 33.6 GHz. SCI effects are completely removed from all curves. The "App. EGN" curve is generated using Eq. (4-5).

Fig. 4-4: Plot of the normalized nonlinearity coefficient η_{XMCI} vs. number of spans in the link, assuming 9 PM-QPSK channels over SMF, NZDSF and LS, with span length 100 km, at 32 GBaud, roll-off 0.05, span length 100 km, channel spacing 50 GHz. SCI effects are completely removed from all curves. The "App. EGN" curve is generated using Eq. (4-5).

4.2.4 PM-16QAM transmission

With PM-16QAM, the GN model correction becomes weaker, as the coefficient Φ in Eq. (4-2) shrinks from 1 (for PM-QPSK) to 17/25. Nonetheless, PM-16QAM system maximum reach prediction is improved in a non-negligible way by correcting the GN model. Therefore, it is desirable that the approximate correction formula Eq. (4-2)

performs well for this format, too. The detailed η_{XMCI} vs. number of spans result obtained for 9-channel systems, with spacing 33.6 GHz, is shown in Fig. 4-6. The accuracy of the asymptotic formula is very good, too.
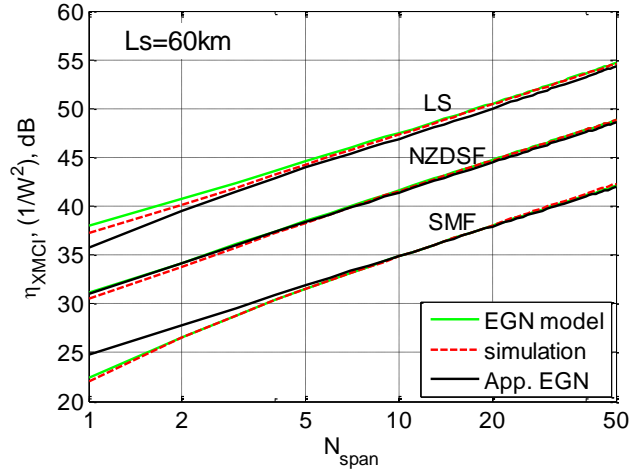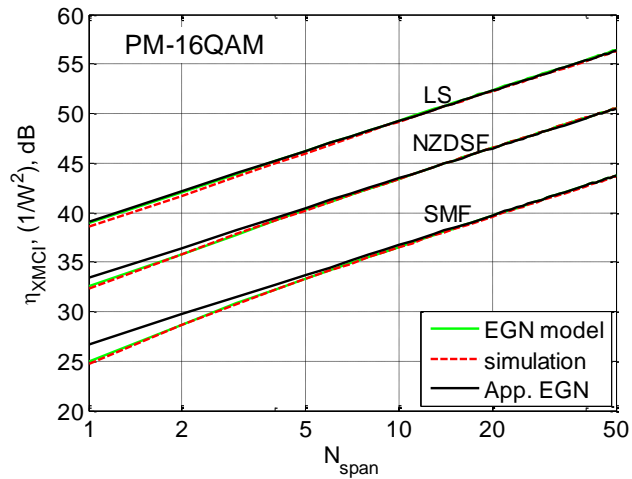

Fig. 4-5: Plot of the normalized nonlinearity coefficient η_{XMCI} vs. number of spans in the link, assuming 9 PM-QPSK channels over SMF, NZDSF and LS, with span length 100 km, at 32 GBaud, roll-off 0.05, span length 60 km, channel spacing 33.6 GHz. SCI effects are completely removed from all curves. The "App. EGN" curve is generated using Eq. (4-5).

Fig. 4-6: Plot of the normalized nonlinearity coefficient η_{XMCI} vs. number of spans in the link, assuming 9 PM-16QAM channels over SMF, NZDSF and LS, with span length 100 km, at 32 GBaud, roll-off 0.05, span length 100 km, channel spacing 33.6 GHz. SCI effects are completely removed from all curves. The "App. EGN" curve is generated using Eq. (4-5).

4.3 System performance prediction

The main declared goal of many of the recent modeling efforts has been that of providing a practical tool for realistic system performance prediction. In this section we present a comparison of the accuracy of the GN model and of the approximate EGN model of Eq. (4-1) in predicting system maximum reach in the same scenarios used in Sect. 3.2. Note that, differently from Fig. 4-1, single-channel nonlinear effects were not removed from the simulations.

We point out that we did not assume that the spectrum of NLI was flat, i.e., we did not use the so-called "white-noise approximation". We did take into account its actual shape when estimating the system maximum reach, either based on the GN model alone or based on Eq. (4-1). Note though that, as pointed out in Sect. 4.1, the approximate correction (4-2) is assumed frequency-independent. We also point out that the simulative results of this section are found by adding all ASE noise at the end of the link, rather than in-line.

Fig. 4-7 shows a plot of maximum system reach vs. channel spacing. With all fibers, the approximate EGN model Eq. (4-1) is quite effective and for low frequency spacing (33.6 and 35 GHz) the predictions based on it come within a quite small error range [-0.2, 0] dB across all scenarios. The error range widens slightly to [-0.4, -0.1] dB for the larger frequency spacing. Since Eq. (4-2) does not appear to lose accuracy at 50 GHz (see Fig. 4-4) we do not think that the somewhat larger error can be ascribed to it. Rather, it could be ascribed to the fact that Eq. (4-1) neglects the non-Gaussianity correction for SCI. This means SCI is overestimated, leading to a pessimistic maximum reach prediction. The impact of such error is greater at larger channel spacing because single-channel effects have a greater relative impact at larger spacing than for quasi-Nyquist spacing. On the other hand, for larger channel counts this error decreases, as SCI is a fixed quantity whereas XMCI increases vs. N_{ch}.
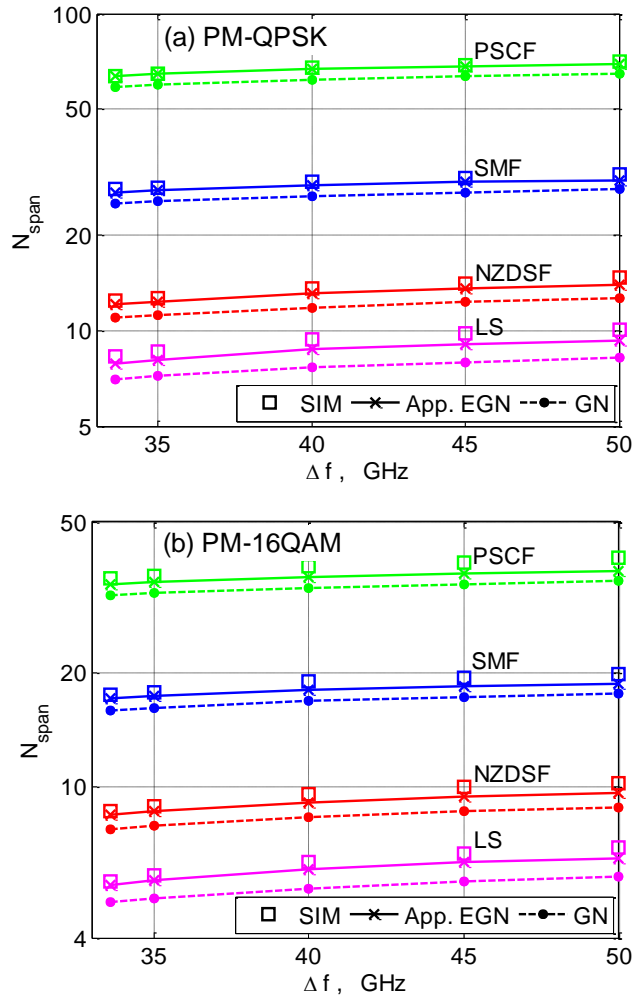
Fig. 4-7: Plot of maximum system reach for 15-channel PM-QPSK and PM-16QAM systems at 32 GBaud, roll-off 0.05, vs. channel spacing Δf, over four different fiber types: PSCF, SMF, NZDSF and LS. The span length is 120 km for PM-QPSK and 85 km for PM-16QAM. The "App. EGN" curve is generated using Eq. (4-5).

4.4 Parameter dependencies of the EGN model approximation

Eq. (4-1) can be made fully closed-form by substituting $G_{\mathrm{NLI}}^{\mathrm{GN}}(f)$ with one of the GN model approximations described for instance in [17]. We discuss here a specific example, that of ideal Nyquist WDM transmission with all-identical spans ([17], Eq. 15), for the sole purpose of pointing out certain parameter dependencies of the resulting formula. NLI is evaluated at the center of the center channel ($f=0$).

Due to the approximations used in [17] to derive Eq. 15 there, to combine such formula with Eq. (4-2) meaningfully we have to assume that for all the spans in the link

the following approximation is accurate enough:

$$\left[1-\exp\left(-2\alpha L_s\right)\exp\left(j\varphi\right)\right]\approx 1 \tag{4-6}$$

where $\varphi=4\pi^2\beta_2\left(f_1-f\right)\left(f_2-f\right)L_s^{n_s}$, and $L_s^{n_s}$ is the length of n_s-th the span. Therefore, the remarks made in the following are valid only if the loss of all of the spans in the link is greater than approximately 10 dB. If so, we can then write:

$$\hat{G}_{\text{NLI}}^{\text{EGN}}\left(0\right)\approx G_{\text{NLI}}^{\text{GN}}\left(0\right)-\hat{G}_{\text{NLI}}^{\text{corr}}\approx\frac{4}{27}\frac{\gamma^2 P_{\text{ch}}^3 N_s}{R_s^3\pi\beta_2\alpha}\cdot$$
$$\left[N_s^{\varepsilon}\operatorname{asinh}\left(\tfrac{1}{4}\beta_2\alpha^{-1}\pi^2 N_{\text{ch}}^2 R_s^2\right)-\frac{10}{3}\Phi\frac{1}{2\alpha L_s}\operatorname{HN}\left(\left[N_{\text{ch}}-1\right]/2\right)\right] \tag{4-7}$$

where "asinh" is the hyperbolic arcsine. The symbol ε is the NLI noise coherent accumulation exponent, typically $\ll 1$. The first term in square brackets derives from $G_{\text{NLI}}^{\text{GN}}\left(f\right)$ whereas the second term stems from the non-Gaussianity correction $\hat{G}_{\text{NLI}}^{\text{corr}}$ shown in Eq. (4-2). The formula shows that these two terms have important common dependencies, which appear as common factors outside the square brackets, such as γ^2, P_{ch}^3 and $1/\beta_2$. Note that the presence of β_2 in the asinh function has little effect because asinh is a log-like slowly increasing function.

From Eq. (4-7) one can directly derive the relative strength of the non-Gaussianity correction $\hat{G}_{\text{NLI}}^{\text{corr}}$ vs. the GN model contribution $G_{\text{NLI}}^{\text{GN}}\left(0\right)$, which can be written as:

$$\hat{G}_{\text{NLI}}^{\text{corr}}\Big/G_{\text{NLI}}^{\text{GN}}\left(0\right)\approx\frac{\dfrac{10}{3}\Phi\dfrac{1}{2\alpha L_s}\operatorname{HN}\left(\left[N_{\text{ch}}-1\right]/2\right)}{N_s^{\varepsilon}\operatorname{asinh}\left(\tfrac{1}{4}\beta_2\alpha^{-1}\pi^2 N_{\text{ch}}^2 R_s^2\right)} \tag{4-8}$$

One interesting aspect is that this ratio is inversely proportional to the span length L_s. It is also inversely proportional to the span loss coefficient α, though approximately, because α is also present in the argument of the asinh function. However, the log-like nature of asinh dampens its variations so that the $1/\alpha$ factor at the numerator of Eq. (4-8) sets the prevailing trend for typical values of the other parameters. Note also that the effect of the asinh is in any case that of making the overall ratio Eq. (4-8) decrease even faster than $1/\alpha$.

Neglecting the asinh variation, then it appears that Eq. (4-8) is inversely proportional to the overall span loss, expressed as $1/(2\alpha L_s)$. In other words, the non-Gaussianity correction has more impact over low span-loss systems. Conversely, it tends to vanish for high-loss spans. This is in agreement with what simulatively or numerically predicted in [30-32], but here this dependence stands out analytically. Once again, though, note that the above formula is accurate only as long as span loss is greater than about 10 dB, i.e., for $1/(2\alpha L_s) \leq 0.43$.

Chapter 5   The EGN model applications

In previous chapters, the EGN model has been proposed and well validated by simulations in a wide range of system scenarios. In this chapter, we employ the EGN model to evaluate NLI generation in some study-cases.

5.1 Dispersion pre-compensation over mixed-fiber links

Chromatic dispersion pre-compensation (CDP) was extensively used and provided substantial performance gains in IMDD DM systems. After the advent of coherent systems operating over UT links, several studies have been carried out to find out whether CDP would be useful in this new system scenarios as well, both simulative [43, 44] and experimental [45-51]. It was found that the optimum CDP, over links with same fiber and span length ("homogenous links"), amounts to 50% of the total link accumulated dispersion. The potential gain on either the Q factor or the system maximum reach was however modest, on the order of a fraction of a dB. The highest gain was 0.9 dB on Q^2 in [46], where PM-BSPK was used. Inhomogeneous links have been investigated, too. In [51], a mixed-fiber link was addressed where a multi-span section used one fiber type and another section a different type, with the two types being either SMF or TrueWave RS. The optimum CDP was for zero-accumulated-dispersion being at the middle of the lower dispersion and more nonlinear Truewave RS fiber section. The Q^2 gain was however minimal, about 0.2 dB at the optimum launch power.

One of the problems in the investigation of CDP systems has also been the lack of models capable of accurately predicting their nonlinear behavior. The GN model, for example, cannot deal with this situation because it assumes that the signal behaves as Gaussian noise (as if it had undergone "infinite" CDP). However, the EGN model avoids making the signal-Gaussianity assumption, enabling it to account for CDP. We first analyzed homogenous links, and then addressed a mixed-fiber case. Through this section, PM-QPSK modulation is used.

5.1.1 Homogeneous fiber links

The systems that we tested are identical to those described in Chapter 3. Specifically,

they are 15-channel WDM PM-QPSK systems, running at 32 GBaud. The channel spacing is 33.6 GHz. The spectrum is root-raised-cosine with roll-off 0.05. EDFA amplification is assumed, with 5 dB noise figure. The considered fibers are: SMF, NZDSF and LS, with same parameters as listed in Sect. 3.1.1, with the exception of the SMF loss that is 0.2 dB/km rather than 0.22, and the LS nonlinearity coefficient that is 2.1 1/W/km) rather than 2.2. The simulation technique is also similar to that of [38].

The homogenous (single fiber type) link uses 120 km span length. We first characterized the system maximum reach, for a target BER 10^{-2}. Its value depends on both launch power per channel P_{ch} and pre-compensation D_{PRE}. The results are displayed in Fig. 5-1. The best values of D_{PRE} essentially coincide with 50% pre-compensation. The optimum P_{ch} appears to depend very weakly on D_{PRE}. The actual improvement in system maximum reach vs. no pre-compensation is, however, small. It is 3.6% for LS and about 3% for NZDSF and SMF. The respective max-reaches are 13.3, 19.4 and 43.7 spans.

To better understand the effect, we studied in detail the accumulation of NLI along the link. The estimation of the NLI noise power was performed as follows. We set P_{ch} to the value granting maximum reach ($P_{ch,max}$). The Rx electrical noise variance of each signal point of the constellation was evaluated on both quadratures and polarizations, turning off ASE noise. The variances were then averaged to obtain an estimate of NLI power P_{NLI} impinging on the Rx. We then calculated the quantity η_{NLI} defined as in Eq. (3-37).

Considering the impact of CDP, the only change in all formulas for SCI, XCI and MCI is the link function μ. At the Tx, a certain amount of dispersion β_{CDP} is compensated, the link function can be written as:

$$\mu(f_1, f_2, f) = \zeta(f_1, f_2, f) \cdot \nu(f_1, f_2, f) \tag{5-1}$$

with:

$$\zeta(f_1, f_2, f) = \gamma \frac{1 - e^{-2\alpha L_s} e^{j4\pi^2 \beta_2 (f_1 - f)(f_2 - f) L_s}}{2\alpha - j4\pi^2 \beta_2 (f_1 - f)(f_2 - f)} \tag{5-2}$$

$$\nu(f_1, f_2, f) = e^{j2\pi^2 (f_1 - f)(f_2 - f)\left[(N_s - 1)\beta_2 L_s - 2\beta_{CDP}\right]} \cdot$$
$$\frac{\sin\left(2\beta_2 \pi^2 (f_1 - f)(f_2 - f) N_s L_s\right)}{\sin\left(2\beta_2 \pi^2 (f_1 - f)(f_2 - f) L_s\right)} \tag{5-3}$$
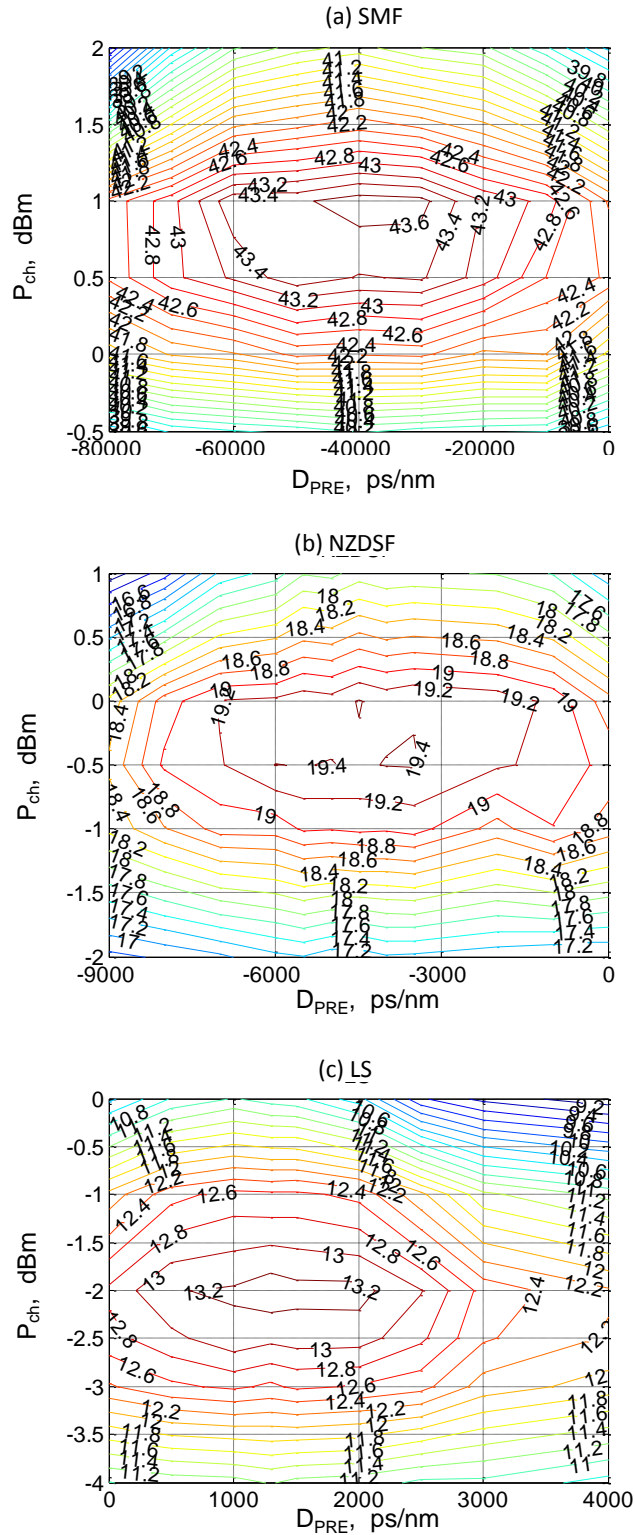
Fig. 5-1: System maximum reach in number of spans (interpolated to non-integer for smoothness), vs. launch power per channel P_{ch} and pre-compensation D_{PRE}, assuming 15 PM-QPSK channels over SMF, NZDSF and LS, with span length 120 km. The CUT is the center channel. The spacing is 1.05 times the symbol rate.

Comparing with the link function without CDP in Eq. (3-32)-(3-34), ζ is identical, but ν is modified with β_{CDP} . In Fig. 5-2, we plot the accumulated η_{NLI} along the link. the range of N_s goes from one to the system maximum reach. The black solid curves are the incoherent GN model. The red curves are for no CDP, the blue curves are for optimum CDP. Solid lines are analytical EGN model, dashed lines are simulations.

A first remark is that simulations and the EGN model match well, which cross-validates the two results. The GN model instead, as expected, overestimates NLI noise. The blue curves have initially a higher value than the red curves but at about mid-link they cross over and, from then on, the red curves have a higher value. The advantage due to optimum CDP is the gap found at maximum reach between the blue and red curves. Its values are rather modest: 0.32, 0.39 and 0.43 dB for SMF, NZDSF and LS, respectively. Note that the gain in maximum reach is expected to follow the "1/3 rule". This agrees with the 3% maximum reach gain found directly as shown in Fig. 5-1.

In Fig. 5-3 we plot the increments span after span of η_{NLI} , called $\Delta\eta_{NLI}$, which can be thought of the derivatives of η_{NLI} curves in Fig. 5-2. Without CDP, the red curves show little NLI generation near the Tx, where the signal is not dispersed. As the signal propagates, the red curves tends to reach the GN model prediction. It is faster over the more dispersive SMF fiber and slower over the less dispersive NZDSF and LS. With optimum CDP at Tx, the signal is substantially dispersed, thus the blue curves tend to behave as the GN model. Then, as the accumulated dispersion reaches to zero near the mid-link, a very evident dip shows up. Thereafter, the signal disperses again and it tends towards the GN model.
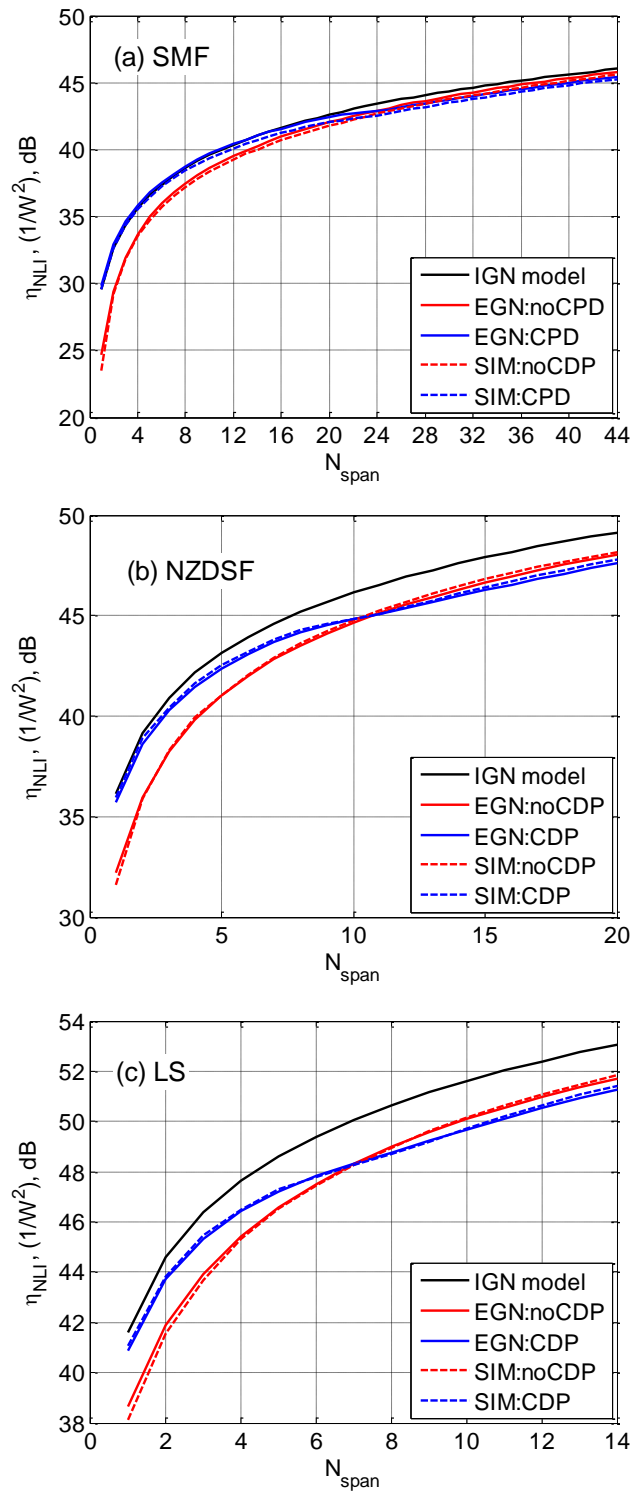
Fig. 5-2: Plot of normalized nonlinearity coefficient η vs. number of spans in the link, assuming 15 PM-QPSK channels over SMF, NZDSF and LS, with span length 120 km. The CUT is the center channel. The spacing is 1.05 times the symbol rate.
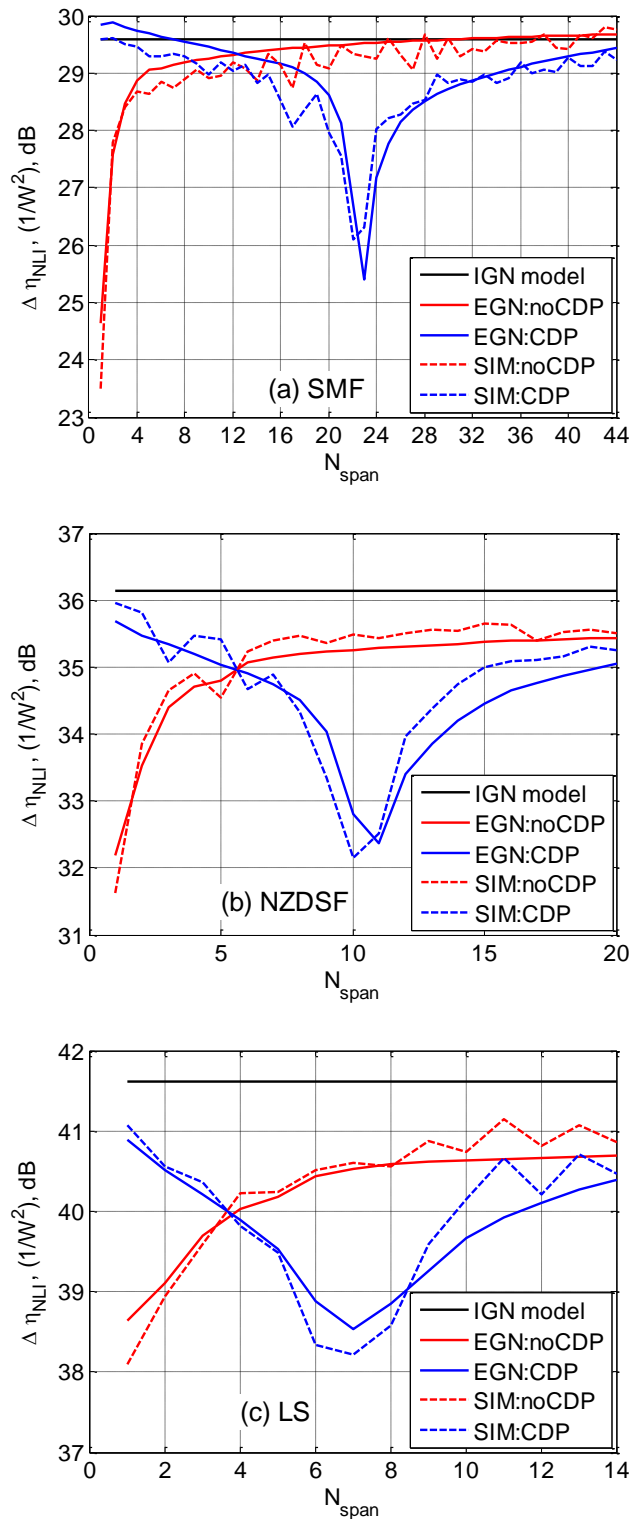
Fig. 5-3: Plot of normalized span-by-span NLI generation $\Delta\eta$ vs. number of spans in the link, assuming 15 PM-QPSK channels over SMF, NZDSF and LS, with span length 120 km. The CUT is the center channel. The spacing is 1.05 times the symbol rate.

5.1.2 Inhomogeneous fiber links

In this section, we moved to consider an inhomogeneous link made up of 20 spans of SMF and 20 spans of LS, in 9 channels with span length 100 km. We evaluated both the case of SMF followed by LS and vice-versa. The system is plotted in Fig. 5-4, at the connection of the two fibers, an attenuator was used to adjust the power.
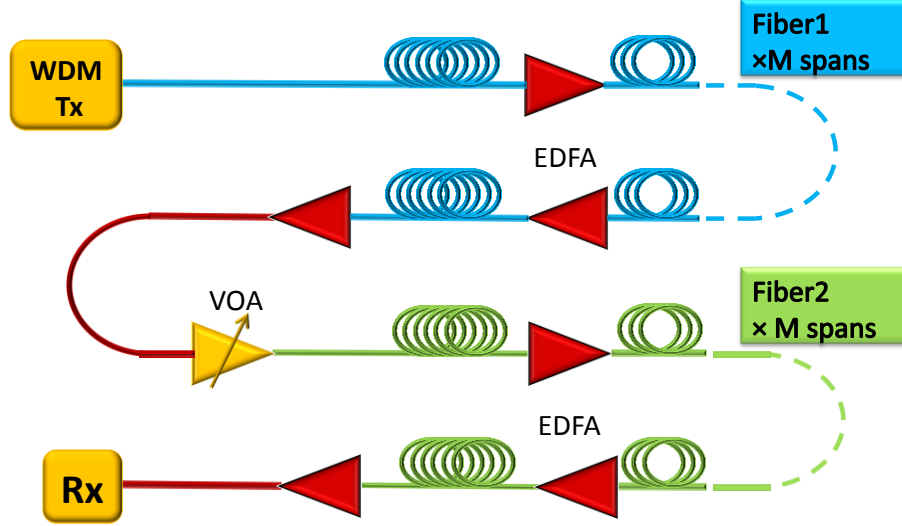
Fig. 5-4: System structure for inhomogeneous fiber links.

In such a system, the link function in the EGN model, without CDP, is:

$$
\begin{aligned}
\mu\left(f_1, f_2, f\right) &= \gamma_1 \frac{1 - e^{-2\alpha_1 L_s} e^{j4\pi^2 \beta_{2,1}(f_1 - f)(f_2 - f)L_s}}{2\alpha_1 - j4\pi^2 \beta_{2,1}\left(f_1 - f\right)\left(f_2 - f\right)} \\
&\quad \cdot e^{j2\beta_{2,1}\pi^2(f_1 - f)(f_2 - f)(N_{s,1} - 1)L_s} \\
&\quad \cdot \frac{\sin\left(2\beta_{2,1}\pi^2\left(f_1 - f\right)\left(f_2 - f\right)N_{s,1}L_s\right)}{\sin\left(2\beta_{2,1}\pi^2\left(f_1 - f\right)\left(f_2 - f\right)L_s\right)} \\
&\quad + \gamma_2 \frac{1 - e^{-2\alpha_2 L_s} e^{j4\pi^2 \beta_{2,2}(f_1 - f)(f_2 - f)L_s}}{2\alpha_2 - j4\pi^2 \beta_{2,2}\left(f_1 - f\right)\left(f_2 - f\right)} \\
&\quad \cdot e^{j2\pi^2(f_1 - f)(f_2 - f)\left[2\beta_{2,1}N_{s,1}L_s + (N_{s,2} - 1)\beta_{2,2}L_s\right]} \\
&\quad \cdot \frac{\sin\left(2\beta_{2,2}\pi^2\left(f_1 - f\right)\left(f_2 - f\right)N_{s,2}L_s\right)}{\sin\left(2\beta_{2,2}\pi^2\left(f_1 - f\right)\left(f_2 - f\right)L_s\right)}
\end{aligned}
\tag{5-4}
$$

where $\left\{\gamma_1, \alpha_1, \beta_{2,1}, N_{s,1}\right\}$ is the parameters for the first type of fiber, and $\left\{\gamma_2, \alpha_2, \beta_{2,2}, N_{s,2}\right\}$ for the second type of fiber.

With CDP, Eq. (5-4) is modified by β_{CDP}, similar to previous section, and the link

function is:

$$
\begin{aligned}
\mu(f_1, f_2, f) = &\gamma_1 \frac{1 - e^{-2\alpha_1 L_s} e^{j4\pi^2 \beta_{2,1}(f_1-f)(f_2-f)L_s}}{2\alpha_1 - j4\pi^2 \beta_{2,1}(f_1-f)(f_2-f)} \\
&\cdot e^{j2\pi^2(f_1-f)(f_2-f)\left[(N_{s,1}-1)\beta_{2,1}L_s - 2\beta_{CDP}\right]} \\
&\cdot \frac{\sin\left(2\beta_{2,1}\pi^2(f_1-f)(f_2-f)N_{s,1}L_s\right)}{\sin\left(2\beta_{2,1}\pi^2(f_1-f)(f_2-f)L_s\right)} \\
&+ \gamma_2 \frac{1 - e^{-2\alpha_2 L_s} e^{j4\pi^2 \beta_{2,2}(f_1-f)(f_2-f)L_s}}{2\alpha_2 - j4\pi^2 \beta_{2,2}(f_1-f)(f_2-f)} \\
&\cdot e^{j2\pi^2(f_1-f)(f_2-f)\left[2\beta_{2,1}N_{s,1}L_s - 2\beta_{CDP}+(N_{s,2}-1)\beta_{2,2}L_s\right]} \\
&\cdot \frac{\sin\left(2\beta_{2,2}\pi^2(f_1-f)(f_2-f)N_{s,2}L_s\right)}{\sin\left(2\beta_{2,2}\pi^2(f_1-f)(f_2-f)L_s\right)}
\end{aligned}
\tag{5-5}
$$

Differently from the homogenous case, we fixed the system reach, to ease the calculations burden. The target of the optimization is then to obtain the highest Rx OSNR, defined as:

$$
\text{OSNR} = \frac{P_{Rx}}{P_{ASE} + P_{NLI}}
\tag{5-6}
$$

Since the overall NLI noise at the Rx depends on both transmitted power at SMF and LS sections, the optimization process involves both parts. As CDP value, we assume either 0 (no CDP) or the optimum value to have zero accumulated dispersion in the middle of the LS section, similar to [51]. The optimum values are -31600 ps/nm and 1800 ps/nm in the SMF-first case and the LS-first case, respectively. They are close to the optimum, but this issue needs further investigation.

The OSNR optimization vs. the transmitted power for SMF and LS is carried out using the EGN model, over a bandwidth equal to the symbol rate. In Fig. 5-5, the optimization is for the SMF-first case. Without CDP, $P_{ch,\,SMF} = -0.6\,\text{dBm}$, $P_{ch,\,LS} = -3.9\,\text{dBm}$, $\text{OSNR} = 7.13\,\text{dB}$. With optimum CDP, $P_{ch,\,SMF} = -0.2\,\text{dBm}$, $P_{ch,\,LS} = -3\,\text{dBm}$, $\text{OSNR} = 7.89\,\text{dB}$. The OSNR gain is 0.76 dB.

In Fig. 5-6, the optimization is for the LS-first case. Without CDP, $P_{ch,\,SMF} = -3.2\,\text{dBm}$, $P_{ch,\,LS} = -0.3\,\text{dBm}$, $\text{OSNR} = 7.70\,\text{dB}$. With optimum CDP, $P_{ch,\,SMF} = -2.9\,\text{dBm}$, $P_{ch,\,LS} = -0.3\,\text{dBm}$, $\text{OSNR} = 7.94\,\text{dB}$. The OSNR gain is only 0.24 dB.

Then we run a simulation to cross-check NLI generation along the link, at the optimum launch power. At present, $P_{ch,SMF}$ and $P_{ch,LS}$ are not any more identical to each other, therefore we could not evaluate the simple quantity η_{NLI} as for the homogeneous link. Taking this impact into account, we focus on the quantity SNR_{NLI}, defined as,

$$SNR_{NLI} = \frac{P_{ch}}{P_{NLI}} \tag{5-7}$$

We looked at the SMF-first case. The numerator of Eq. (5-7) must be the optimum launch power into the SMF up to 20 spans, and then into the LS up to 40 spans. All these values have been read from Fig. 5-5. In Fig. 5-7, the SNR_{NLI} is plotted, showing an excellent agreement between the EGN model and simulations. This provides a compelling confirmation of the results.
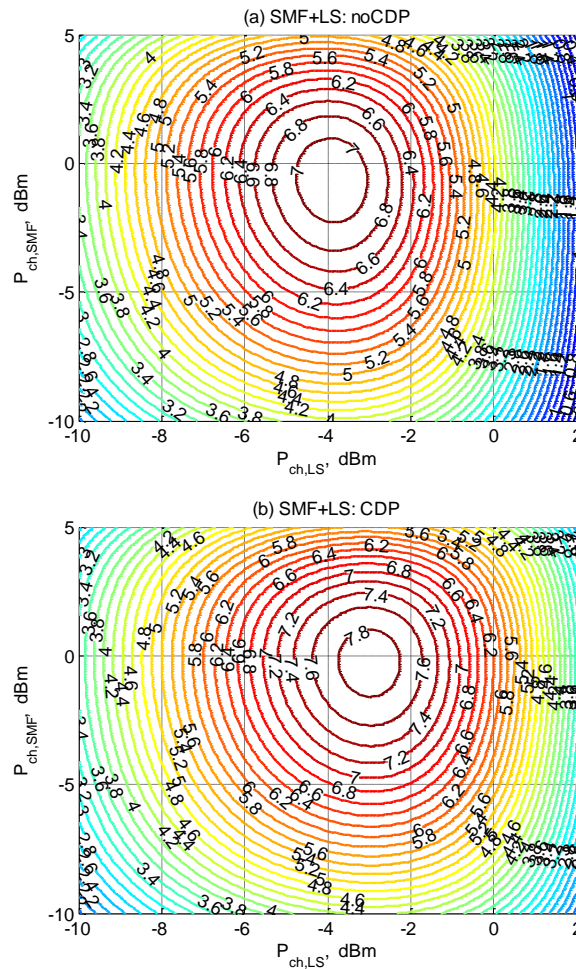

Fig. 5-5: System optimum OSNR vs. launch power per channel for SMF and LS, no CDP and with optimum CDP, for an inhomogeneous system with 20 spans of SMF followed by 20 spans of LS fiber, 9 PM-QPSK channels, span length 100 km, 32 GBaud and 33.6 GHz spacing.
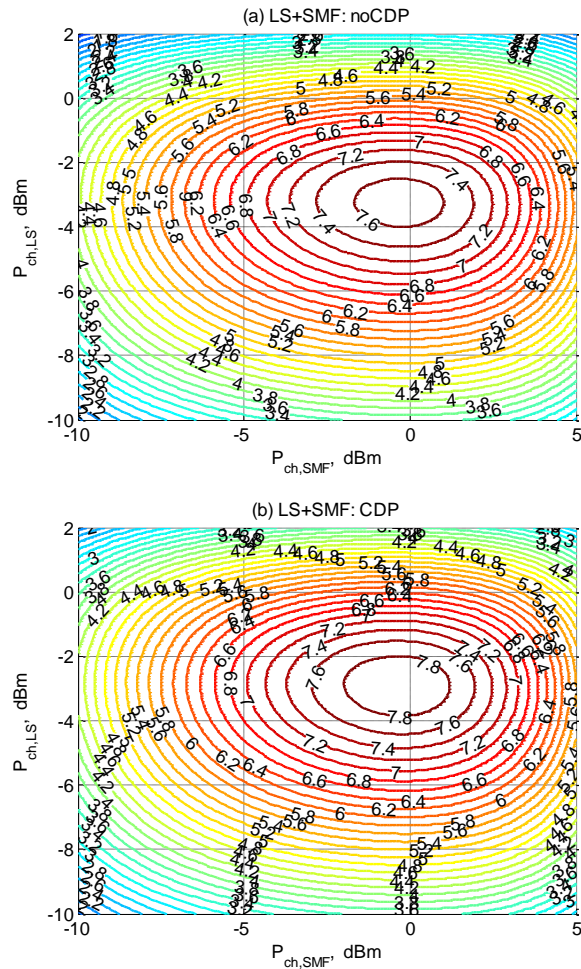
Fig. 5-6: System optimum OSNR vs. launch power per channel for SMF and LS, no CDP and with optimum CDP, for an inhomogeneous system with 20 spans of LS followed by 20 spans of SMF fiber, 9 PM-QPSK channels, span length 100 km, 32 GBaud and 33.6 GHz spacing.
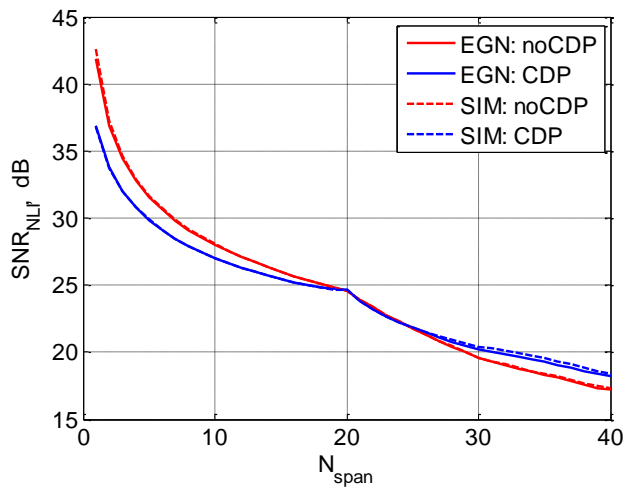

Fig. 5-7: SNR_{NLI} vs. number of spans, for the same inhomogeneous system in Fig. 5-5.

5.2 Determining the optimum system symbol rate

Recent experiments [49, 50], have shown a rather strong maximum reach gain (20%) in long-haul transmission when a single serial-channel (SC) was broken up into either OFDM subcarriers [49] or FDM quasi-Nyquist subcarriers [50]. Simulative evidence of a dependence of performance on the per-subcarrier symbol rate had also been found in [51-54].

Investigating the behavior of NLI when changing the symbol-rate of WDM channels appears to be an interest case-study. In this section, we study this topic with four nonlinearity models: the GN model [38], the XPM model [30], the EGN model in chapter 3 and the EGN model approximation in chapter 4.

5.2.1 Analytical modeling and simulations

This question can be simply formulated as follows: given pre-determined total WDM bandwidth, spectral efficiency, spectrum roll-off and modulation format, what is the symbol rate which minimizes NLI generation?

Note that the above constraints make the total raw bit rate, conveyed by the overall WDM signal, a constant, too.

We looked at several test system configurations, having the following fixed common transmission parameters: total WDM bandwidth 504 GHz, PM-QPSK modulation, roll-off 0.05, quasi-Nyquist channel spacing (1.05 times the symbol rate). These parameters imply a fixed total raw bit rate of 1.92 Tb/s, irrespective of the symbol rate per channel, with a raw spectral efficiency of 3.81 b/(s Hz).

We left as free parameter the number of channels N_{ch} that the overall WDM bandwidth is split into or, equivalently, the per-channel symbol rate $R_{\text{ch}} = 480/N_{\text{ch}}$ (GBaud). As for the fibers, we looked at all three fibers SMF, NZDSF and LS in Sect. 3.1.1 and PSCF in Sect. 3.2.

The NLI-related quantity chosen for the study is $\tilde{G}_{\text{NLI}}$, defined as the PSD of NLI falling over the center channel and averaged over it. It is then also normalized vs. the transmission signal PSD cube, G_{ch}^3. In math:

$$\tilde{G}_{\text{NLI}} = \frac{P_{\text{NLI}}}{R_{\text{ch}} \cdot G_{\text{ch}}^3} \tag{5-8}$$

where P_{NLI} is the overall NLI power affecting the center channel. The convenient features of $\tilde{G}_{\mathrm{NLI}}$, are: it is independent of the power per channel launched into the link; it is independent of the symbol rate per channel; the same value of $\tilde{G}_{\mathrm{NLI}}$ for different symbol rates means that the corresponding systems would achieve the same maximum reach.

Fig. 5-8 shows $\tilde{G}_{\mathrm{NLI}}$ at 50 spans for SMF and at 30 spans for NZDSF, with span length 100 km. These span numbers correspond approximately to maximum reach performance when assuming EDFA amplification with 5.5 dB noise figure. Note though that the plots at other span numbers are qualitatively similar. The GN model line is essentially flat, that is, it predicts no change of performance vs. the number of channels the total WDM bandwidth is split into.

The EGN model, on the contrary, shows a change, and in particular it shows a minimum, which for SMF and NZDSF is located at about 200 and 70 channels, i.e., at about 2.4 and 6.8 GBaud, respectively. The NLI mitigation vs. the current industry-standard 32 GBaud (15 channels) is 1.2 and 0.7 dB, respectively. These results agree very well with the computer simulations (markers). Interestingly, Fig. 5-8 also shows that the GN and EGN models tend to come together both at very large and very small symbol rates.

The EGN model approximation (App. EGN) in Chapter 4 does not correct SCI contribution, so we subtracted SCI correction (which accounts for the signal non-Gaussianity and is calculated through the EGN model) from the EGN model approximation, and generated the curve marked "App. EGN-SCI$_{\mathrm{corr}}$" in Fig. 5-8. The plot shows that, it is accurate at large symbol rates, but departs from the EGN model since the optimum symbol rate. According to this feature, other OptCom Group members derived a formula Eq. (5-9) to calculate the optimum symbol rate. I will provide its validation in next subsection.

The XPM model does not include SCI. If plotted by itself it generates the curve marked "XPM" in Fig. 5-8. We supplemented it with the SCI contribution calculated through the EGN model, so that a comparison could be carried out. The plot shows that, the XPM+SCI model is accurate at quite large symbol rates. However, it departs from the EGN model when moving towards low symbol rates. At the optimum N_{ch}, the

XPM+SCI model underestimates NLI by about 5 dB, both for SMF and NZDSF. Note also that its prediction appears to decrease steadily for $N_{ch} \to \infty$. The reason for this behavior is that all of FWM is neglected.

To understand everything well, we decomposed the EGN model into SCI, X1 (XPM) and all other FWM to evaluate their trend vs. the number of channels N_{ch}. In Fig. 5-9, we plot $\tilde{G}_{NLI}$ of these three components for SMF and NZDSF used in Fig. 5-8. For low N_{ch}, there is no doubt that SCI is the most important component. With increasing N_{ch}, X1 becomes stronger than others. After a big N_{ch}, FWM grows up to be the biggest one. This figure shows that FWM is important to identify the optimum symbol rate.

In Fig. 5-10, we do all calculations for 100 spans of PSCF, with span length 60 km. It shows that all models behave similarly as for SMF and NZDSF in Fig. 5-8. The EGN model finds out the optimum symbol rate that is about 2 GBaud. The NLI mitigation vs. 32 GBaud (15 channels) grows up to 2.2 dB. Compared with previous results, it appears that NLI mitigation increases substantially.

Regarding the possible practical impact of these results, we have to translate NLI mitigation into maximum reach gain. According to the "1/3 rule", NLI mitigation 1.2, 0.7 and 2.2 dB leads to about 0.4, 0.24 and 0.74 dB (or 10%, 6% and 19%) maximum reach increases for SMF, NZDSF and PSCF, respectively.

To double check this prediction, we ran detailed maximum reach simulations over NZDSF for the same system described above, at different symbol rates with BER 4·10[-3]. In Fig. 5-11 we show the EGN model reach predictions as lines and the simulation results as markers. The correspondence is good, confirming the expected 6% maximum reach increase at the optimum rate predicted through the EGN model, vs. the 32 GBaud scenario.

5.2.2 Closed-form optimum symbol rate formula

For quasi-Nyquist systems with all identical spans, a formula to calculate the optimum symbol rate is found by other OptCom Group members from [42]:

$$R_{opt} = \sqrt{2 \big/ \left(\pi \, |\beta_2| \, L_s N_s \right)} \qquad (5\text{-}9)$$

This formula indicates that the optimum rate is a function not only of the accumulated dispersion per span $|\beta_2| L_s$ but also of the link length through N_s. Owing to the square

root in Eq. (5-9), the range of optimum rates is relatively narrow.

In this subsection, I provided its validation. In Fig. 5-12, the solid lines show the predicted optimum symbol rate by Eq. (5-9) vs. the fiber dispersion and link length in number of spans with span length 100 km. The markers show the optimum symbol rate found by the EGN model over PSCF, SMF, NZDSF and LS. The figure shows an excellent match over a wide range of dispersion and number of spans. Most of R_{opt} belong to the interval 2-10 GBaud.
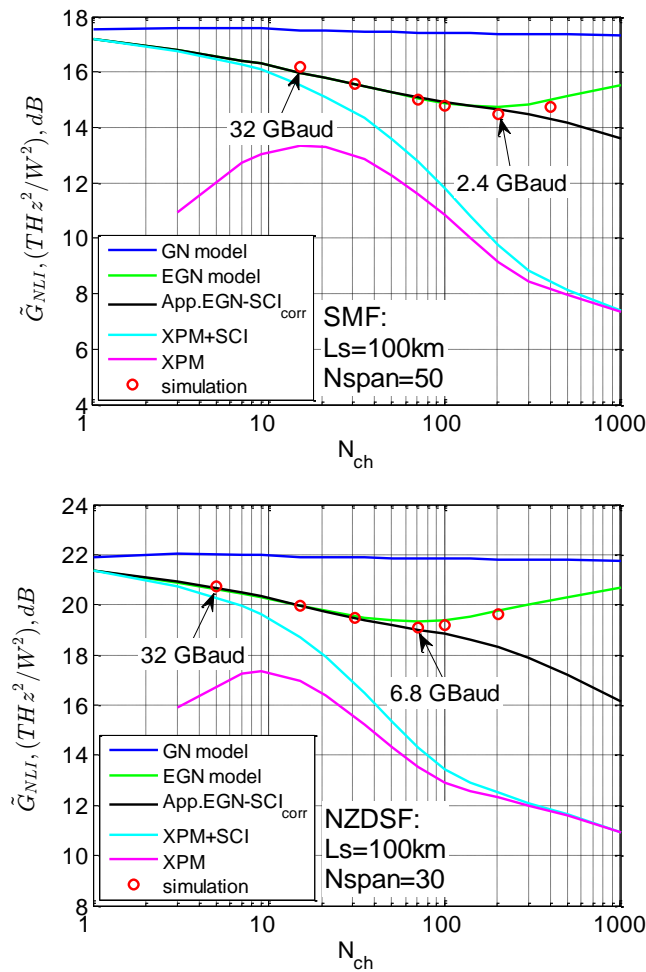

Fig. 5-8: $\tilde{G}_{NLI}$ over the center channel vs. the number of channels N_{ch}, measured at 50 spans of SMF or 30 spans of NZDSF. Span length is 100 km. The modulation format is PM-QPSK, with roll-off 0.05 and spacing 1.05 the symbol rate. The total WDM bandwidth is 504 GHz. Lumped amplification is assumed.
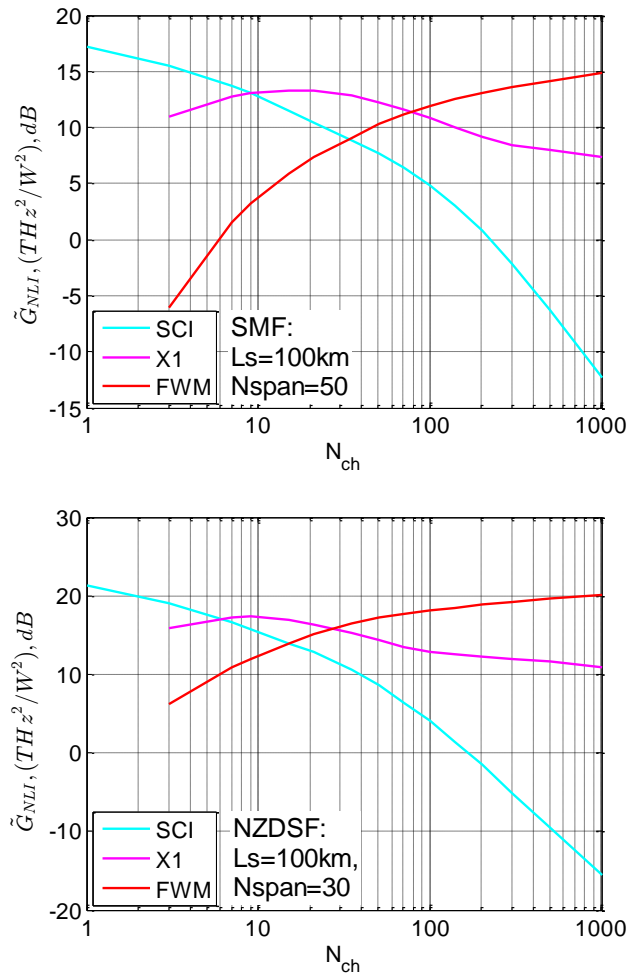
Fig. 5-9: SCI, X1 and FWM trend over the center channel vs. the number of channels N_{ch}, measured for the same fibers SMF and NZDSF in Fig. 5-8.
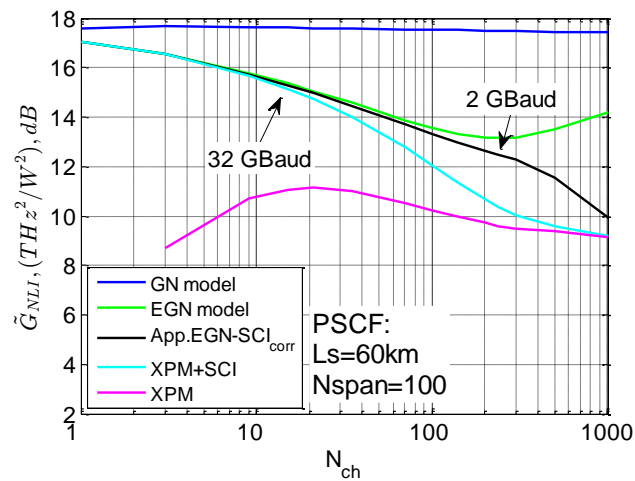

Fig. 5-10: $\tilde{G}_{NLI}$ over the center channel vs. the number of channels N_{ch}, measured at 100 spans of PSCF. Span length is 60 km. The modulation format is PM-QPSK, with roll-off 0.05 and spacing 1.05 the symbol rate. The total WDM bandwidth is 504 GHz. Lumped amplification is assumed.
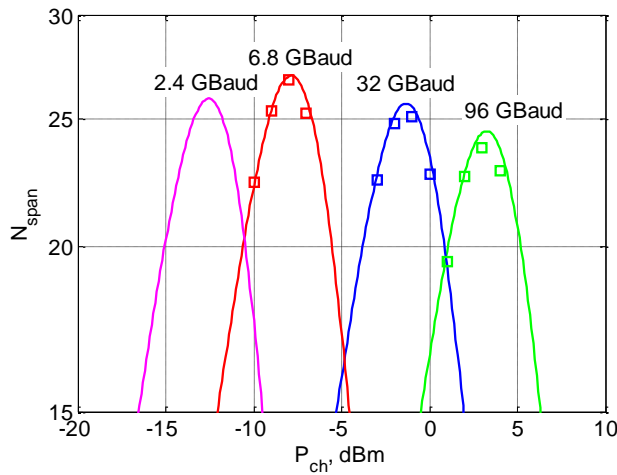
Fig. 5-11: System maximum reach in number of spans at different system symbol rate over NZDSF, span length is 100 km. The modulation format is PM-QPSK, with roll-off 0.05 and spacing 1.05 the symbol rate. The total WDM bandwidth is 504 GHz. Lumped amplification is assumed. Solid lines: the EGN model predictions. Markers: simulative results.
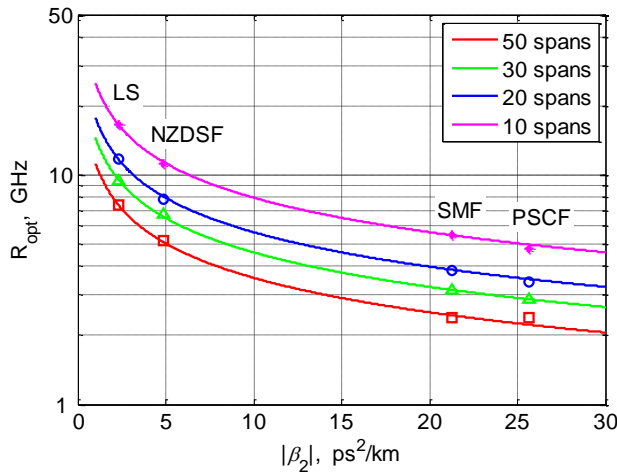

Fig. 5-12: The optimum symbol rate predicted by Eq. (5-9) (solid lines) or by the EGN model (markers) as a function of fiber dispersion and of link length in number of spans with span length 100 km.

5.3 NLI modeling for dynamically reconfigurable networks

In dynamically reconfigurable networks (DRNs), each optical transmission channel can be re-routed at each network node and hence, contrary to point-to-point (PTP) links, it can change its spectrally neighboring channels, possibly many times. Such neighboring channels can in principle have a different symbol rate, format, and

accumulated dispersion.

This complicates drastically the nonlinearity modeling problem, since the final amount of NLI impacting any given channel (assumed as the CUT) depends on the detailed overall "propagation history" of the CUT itself and all of its INTs, from source to destination. The EGN model can be extended to take such propagation history fully into account and deliver a very accurate end result. On the other hand, its complexity, already substantial for the PTP case, is further exacerbated.

In practice, in DRNs there is a need for fast assessment of physical layer impairments, so that the control plane can enact "physical-layer aware" routing and traffic allocation decisions, essentially "real-time". Given this requirement, it is hard to picture the EGN model, made more complex by the need to take into account the propagation history of each CUT and INT, as a practical real-time solution for DRNs.

We started out by looking at five different link scenarios, that have the following features in common:

- 50 spans of SMF and NZDSF (same as in Sect. 3.1.1)with 100 km each span;
- 15 channels are transmitted, with symbol rate 32 GBaud and 33.6 GHz spacing; all spectra are raised-cosine with roll-off 0.05, all channels are launched with the same power, the total WDM bandwidth is 504 GHz;
- The spectrum of the WDM signal launched is the same across the five scenarios at every point along the link;

Assuming that the CUT is the center channel in the WDM comb, the scenarios 1-5 have the specific features:

#1. The CUT and the INTs are all PM-QPSK, and they propagate together from source to destination;

#2. The CUT and the INTs are all PM-16QAM, and they propagate together from source to destination;

#3. The CUT is PM-QPSK and the INTs are all PM-16QAM, and they propagate together from source to destination;

#4. The CUT and INTs are all PM-QPSK. The INTs are completely replaced every 10 spans with others with identical features but independent data. This mimicks a situation where the CUT is re-routed every 10 spans, changing all of its INTs. The

new INTs are assumed not to originate at the CUT routing nodes. For simplicity, it is assumed that all of them have already travelled 10 spans before the CUT joins them;

#5.   Same as 4 but all channels (CUT and INTs) are PM-16QAM.

The first two PTP scenarios have been well investigated through the EGN model in Chapter 3. Now we concentrated on the other three scenarios. Scenario #3 is still PTP, with the change CUT and INTs having different modulation formats. As discussed in Chapter 3, the impact of modulation format is specified through the two values of Φ and Ψ. The formulas of SCI, XCI and MCI in Eq. (3-23), (3-40) and (3-60) show that the contributions from SCI, X2 and X3 are controlled by the CUT modulation format, while the other contributions from X1, X4 and MCI are controlled by the INTs modulation format. Therefore, we can still use all formulas in Chapter 3 with carefully chosen values of Φ and Ψ (in Table 3-1) for each contribution.

For scenarios #4 and #5, the CUT is propagating from source to destination without re-routing and no CDP, so that SCI can be easily calculated by Eq. (3-23). The whole link is cut up into five sections with 10 spans each section. All INTs in one section are independent on the ones in another section. Therefore, the final PSD of XMCI is the incoherent sum of the values from all sections. In each section, the INTs take 10-span CDP, which has been dealt with in Sect. 5.1.1. So we can calculate XMCI conveniently.

The NLI accumulation curves for the five scenarios are shown in Fig. 5-13. The GN model is shown as a gray solid line. There is only one such line because the GN model prediction is the same for all scenarios, since the GN model only looks at the PSD of the WDM signal, which is identical. Note also that the GN model curve is pessimistic, i.e., it predicts more NLI, in all cases.

Regarding the EGN results, the lowest curve is that of scenario #1, i.e., a PTP link with all PM-QPSK channels. The other curves are comprised between this curve and the GN model. In particular, scenario #4 shows that it is important to take the detailed INT history into account. A comparison of scenarios #1 and #2 shows the impact of changing the format of the INTs. A comparison of scenarios #2 and #3 shows that the format of the INTs is more important in the generation of NLI than that of the CUT itself. Overall, Fig. 5-13 shows that various scenarios whose spectrum is everywhere identical along the link

may produce rather different NLI curves.

We then wanted to check whether this behavior was maintained at a substantially higher channel count. In Fig. 5-14, we moved to 41 channels. The results show a similar performance to 15 channels in Fig. 5-13.

In an actual DRN, many more situations that are also spectrally identical to these could show up, where the INTs could change more or less frequently and could come into the link with any amount of accumulated dispersions. INTs and CUT could have any mix of different formats. Remarkably, all the corresponding NLI curves would essentially fall within the relatively narrow region, comprised between the curve of the PTP-like scenario using the lowest-cardinality format and the GN model curve. The GN model curve is an upper bound for all possible different situations that may present themselves.

Based on this circumstance, an approximate but conservative modeling approach could be that of adopting the GN model. This means that performance prediction would be pessimistic, to some variable degree. On the other hand, the added complexity required to obtain the accurate EGN model curves would be extremely large. Also, it would typically gain a relatively modest improvement in accuracy vs. the GN model, considering the "1/3 rule".

However, the GN model still requires to keep track of some of the propagation history of the CUT, namely the features of all the spans traversed by it, as well as the full WDM spectra present in such spans, though the format and propagation history of the INTs is no longer needed. In addition, it still requires numerical integration, which may be particularly hard to perform due to the presence of the ν factor in the link function. These requirements put the pure GN model approach still far away from handling real-time. Hence, further approximations are necessary.

An effective simplification strategy is the incoherent GN model [38], which does not remove the need for numerical integration, but it removes the problematic ν factor from the link function. Fig. 5-13 and Fig. 5-14 show the incoherent GN model curve as light green solid. For 41 channels, it gets closer to the GN model and detaches itself from the bundle of the scenarios 1-5 curves. It would then become an approximate upper bound, tighter than the GN model. Large channel count is synonym of high network loads,

which are arguably those of greatest interest in the management of DRNs, so this behavior of the incoherent GN model is in fact a desirable one.

Therefore, despite the rather coarse approximations involved in the derivation of the incoherent GN model, it may actually represent a viable, convenient and sufficiently reliable tool for real-time-compliant physical-layer-awareness in future DRNs.
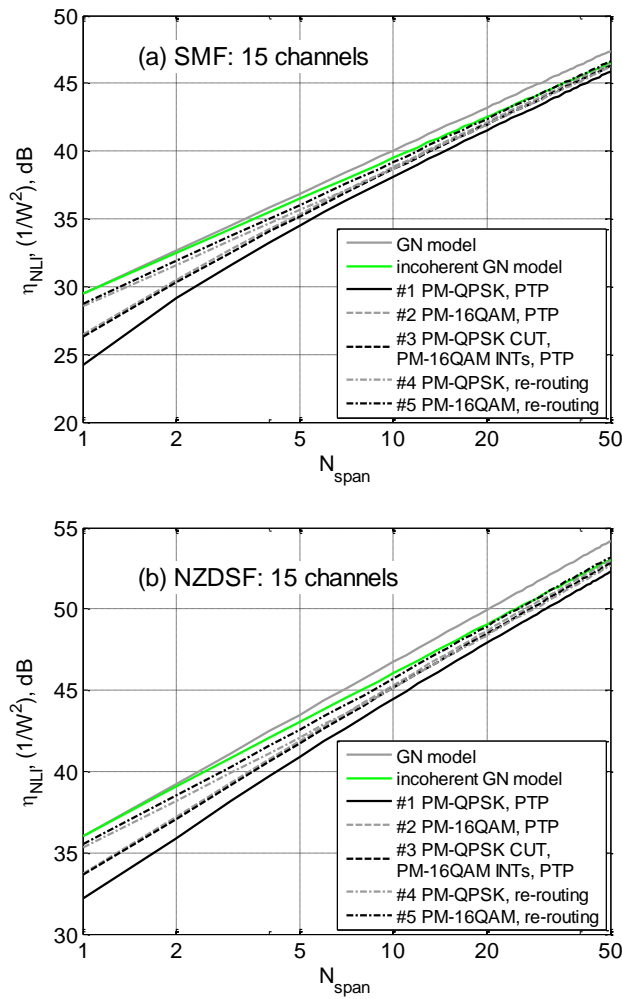

Fig. 5-13: Plot of normalized nonlinearity coefficient η vs. number of spans in the link, assuming 15 PM-QPSK channels over SMF and NZDSF, with span length 100 km. The CUT is the center channel. The spacing is 1.05 times the symbol rate.

Fig. 5-14: Plot of normalized nonlinearity coefficient η vs. number of spans in the link, assuming 41 PM-QPSK channels over SMF and NZDSF, with span length 100 km. The CUT is the center channel. The spacing is 1.05 times the symbol rate.
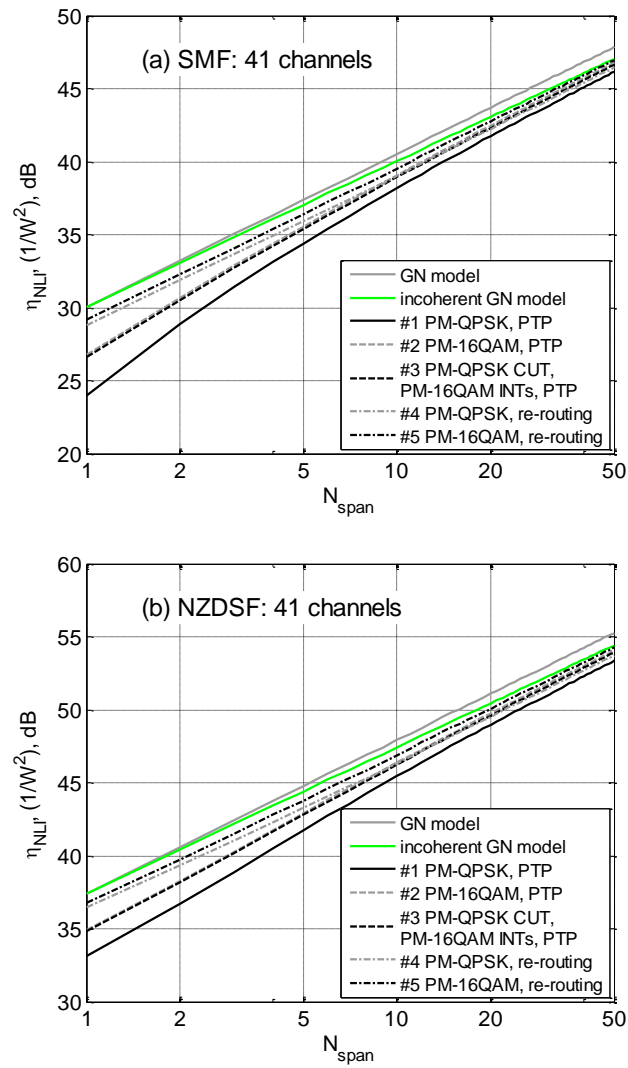
Chapter 6   Experimental validation of the EGN model

Up to now, the accuracy of the EGN model has been tested only by simulations. In this chapter, we show for the first time an experimental validation of the EGN model over a multi-span transmission link.

6.1 Experimental set-up

In realistic long-haul transmission scenarios, the difference between the GN and EGN models in predicting system maximum reach is small, as discussed in Sect. 3.2. In order to achieve a substantial prediction difference between these two models, even in the presence of the measurement uncertainties typical of experimental set-ups, the link had to be specially designed. In our experiment, a very short span length (25 km) was chosen.

The experimental setup is shown in Fig. 6-1. An array of 19 lasers positioned between 192.916 THz and 192.268 THz was finely tuned at 36 GHz frequency separation. The CUT, at the center of the comb, was generated using an external cavity laser (ECL) while for all INTs distributed-feedback (DFB) lasers were used. A couple of single nested Mach-Zehnder modulators (SN_MZM) modulated the odd and even interfering carriers. Polarization multiplexing of INTs was obtained through a PM emulator, while the CUT was modulated by a double nested Mach-Zehnder (DN_MZM) that directly generated a polarization multiplexed optical signal.

We first considered a standard scenario where PM-QPSK was chosen both for CUT and INTs. The symbol rate was 32 GBaud and the electrical signals driving the modulators were generated using fast digital to analog converters (DAC). Four de-correlated $2^{11}-1$ pseudo-random binary sequences (PRBS) were digitally filtered, in order to obtain a square root raised cosine spectral shape with roll-off 0.1 and electrical bandwidth equal to half the symbol rate. A digital pre-emphasis was also applied to partially compensate for in-band bandwidth limitations of the Tx components. The used DACs were CISCO prototypes running at 64 GSample/s (corresponding to 2 samples per

symbol) and characterized by four independent output ports; therefore, a single prototype was sufficient for generating the in-phase (IX, IY) and quadrature signals (QX, QY) for each polarization that drove the modulator of the CUT.

The INTs were modulated using only two driving signals since they were polarization-multiplexed using a PM-emulator. Therefore, a second DAC prototype was sufficient for the simultaneous generation of the in-phase and quadrature (IX1, QX1) signals for the even-channels and for the odd-channels (IX2, QX2).
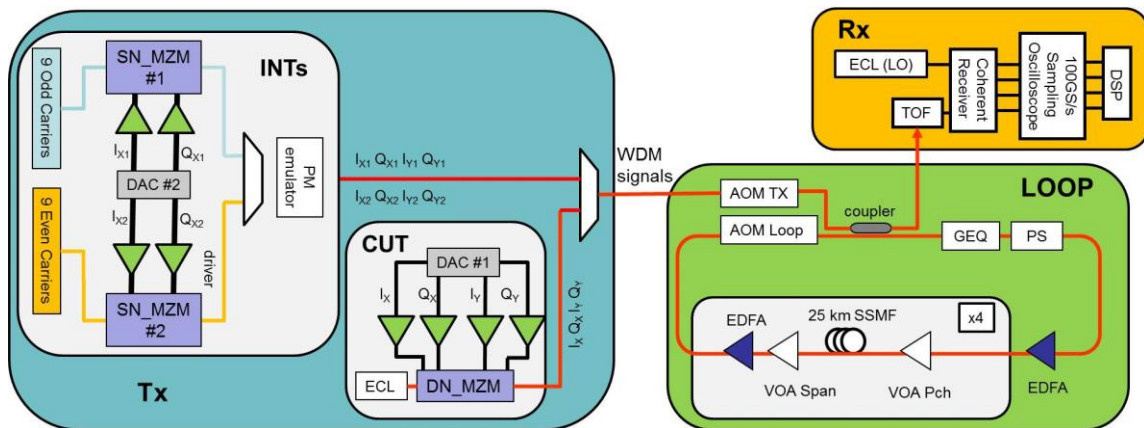

Fig. 6-1: Experimental setup.

A second scenario was selected in order to highlight the change in maximum reach related to the statistical properties of the adjacent channels. This aspect is properly taken into account by the EGN model while it does not affect the GN model, since the latter is intrinsically modulation-format independent. Specifically, the INTs were generated with a Gaussian-distributed constellation of symbols. The launched optical power of the Gaussian INTs was adjusted to be the same as that of the PM-QPSK INTs. The signal samples were clipped at a value equal to 3σ, in order to limit the penalty due to the finite resolution of the DACs, and digitally filtered to achieve exactly the same Nyquist shaping and pre-emphasis applied to the binary PRBS sequences.

The WDM comb was launched into a re-circulating fiber loop that made use of EDFA-only amplification and consisted of four spans of uncompensated SMF, with length approximately equal to 25 km (see Fig. 6-1). A first variable optical attenuator (VOA Pch), inserted at the beginning of each span, was used to adjust the total launched power, while a second one (VOA Span) was used to force the total span loss to 18 dB. The average fiber losses were directly measured on the spools while dispersion and non-

linearity coefficient were taken from manufacturer data-sheets. Extra-losses due to splices between patch-cords and fibers at each side of the spools have been carefully characterized and taken into account in model predictions. All fiber characteristics are summarized in Table 6-1.

Table 6-1: Parameters of the fiber types

	Ls [km]	α [dB/km]	γ [1/W/Km]	D [ps/nm/km]	Extra Loss Input [dB]	Extra Loss Output [dB]
Span 1	24.9	0.196	1.3	16.66	0.58	0.32
Span 2	25.7	0.192	1.3	16.66	0.60	0.37
Span 3	24.8	0.196	1.3	16.66	0.75	0.52
Span 4	25	0.189	1.3	16.66	0.56	0.59

The total launched power was controlled with a resolution of 0.2 dB exploiting the internal power monitor of the EDFAs and knowing the losses of VOAs and fibers. The loop also included a spectrally-resolved gain equalizer (GEQ) and a loop-synchronous polarization scrambler (PS) to compensate for the EDFA gain-tilt and to effectively average the impact of polarization effects, respectively. The GEQ was not able to correct gain tilt lower than 1 dB and gain ripples of any value. A fifth EDFA was used to compensate insertion losses due to GEQ, PS, coupler and acousto-optic modulators (AOM), that, as a whole, act as an extra artificial span with no dispersion.

At Rx, the WDM signal was first sent into a tunable optical filter with bandwidth 50 GHz and subsequently fed to a standard coherent Rx front-end, where the signal was mixed with the local oscillator, i.e., a tunable ECL different from the one used at the Tx. The four electrical outputs of the Rx front-end were digitized using a 100 GS/s real-time oscilloscope (composed of two synchronized Tektronix DPO73304DX). Offline DSP was used to down-sample, equalize and demodulate the acquired signals.

The span length was properly selected to only 25 km in order to emphasize the difference in max-reach prediction obtained by GN and EGN models, to be able to detect it reliably even in the presence of measurement uncertainties. At the same time we were forced to insert extra-loss in the spans in order to keep the maximum number of recirculations below 20 (i.e., 80 spans) and thus avoid excessive accumulation of residual gain tilt and other effects, such as PDL.

6.2 Experimental results

A first set of measurements was taken in back-to-back (btb) condition to determine the sensitivity of the CUT transceiver: results are reported in Fig. 6-2 for the 19-channel WDM configuration described in Sect. 6.1, together with the ideal curve. As target BER for the subsequent propagation tests we chose $1 \cdot 10^{-2}$, a value that can be handled by commercial hard-decision FECs with 20% overhead. At such target BER, the Tx/Rx pair was affected by a btb penalty of 2.1 dB with respect to the ideal curve.

We then moved to transmission measurements to determine the maximum number of spans N_s as a function of the launched channel power P_{ch}. Being BER measurements taken every four spans, the value of N_s at BER threshold was evaluated by interpolation. The value of the equivalent EDFA noise figure to be used in predictions was estimated by matching the system performance in the linear part of the reach curve for the scenario with PM-QPSK INTs. The obtained value was 5.4 dB: it was then used in all predictions.

The reach results are shown in Fig. 6-3 as markers together with model predictions. In the case of INTs with Gaussian constellation, we report the original data (white squares) and a horizontally shifted version of them by -0.35 dB (black squares) which appears to fit the model better. Being a purely horizontal shift, we attribute it to a drift in the power-measurement equipment when moving from first to second scenario. Note that this uncertainty does not affect the maximum reach difference between the two scenarios.

The correspondence between measurement and the EGN model predictions is good. In particular, we think it is very significant that the performance gap between the two types of INTs modulation is very precisely reproduced. This reach difference between PM-QPSK and Gaussian INTs obtained on the exactly same physical set-up, is a sort of differential measurement. As such, it is approximately insensitive to possible errors in the knowledge of system parameters and makes the overall experiment much more reliable.

In conclusion, this first attempt at a direct experimental confirmation of the EGN model appears to indicate that the EGN model predictions are indeed reliable, qualitatively and quantitatively. In particular, a reach prediction about 25% greater than the GN model one was indeed observed, in an experimental setup designed explicitly to make such difference large enough.
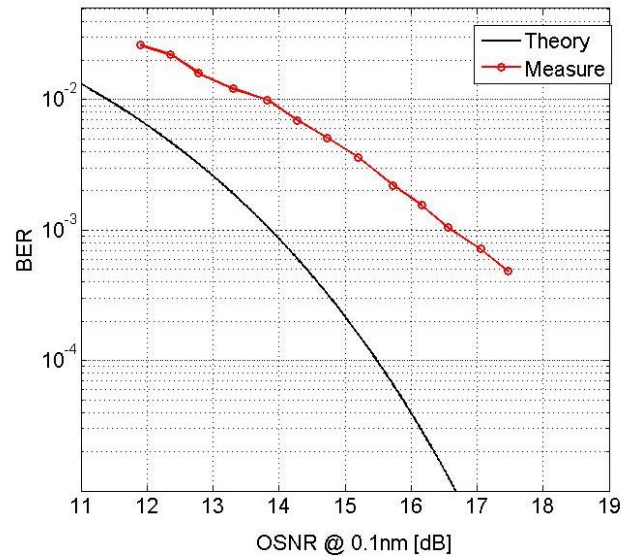
Fig. 6-2: Back-to-back BER vs. OSNR on channel under test, for the complete WDM system.
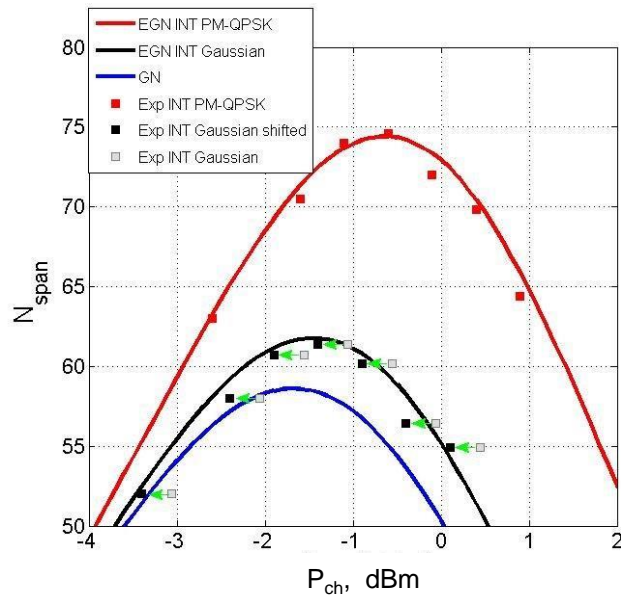

Fig. 6-3: System maximum reach in number of spans vs. P_{ch} for a 19-channel WDM experiment, at 32 GBaud, roll-off 0.1, channel spacing 36 GHz, over SMF. The center channel is PM-QPSK modulated. The other channels are either PM-QPSK or Gaussian-constellation. The span length is 25 km. All solid curves are from models, and all markers are from measurements.

Chapter 7   Summary and conclusion

In this thesis, I have extended the GN model to take the general dispersion profile into account. Through the comparison with the GNRF over a wide range of fibers, I have shown that third-order dispersion has a very substantial effect on nonlinearity, especially near a fiber dispersion-zero.

I have performed the analytical derivation of the EGN model to remove the signal Gaussianity assumption completely. I have provided a set of formulas describing all contributions from SCI, XCI and MCI, and provided the numerical results to be validated them vs. simulation. The EGN model presented here exhibits the best predictive power so far, among the various approximate GN-related models available. This is not only true at a span count nearing maximum reach, but throughout the link. It shows no evident bias versus nonlinearity over or underestimation.

I have reported on a closed-form correction to the GN model, based on an approximation of the EGN model. The formula improves the GN model accuracy by suppressing most of its tendency to overestimate nonlinearity, but neglects to correct SCI overestimation. However, this limitation has little impact in a WDM system with a significant number of channels. I have tested its accuracy vs. the EGN model and simulation. This approximation provides a very effective tool that significantly improves the overall accuracy of the GN model in predicting realistic WDM system performance without substantially increasing its computational complexity.

I have used the EGN model to investigate the NLI generation in some study-cases. It turns out that the EGN model is capable of dealing with the dependence of the system nonlinear behavior on dispersion conditions (such as pre-compensation and very low dispersion fibers), mixed-fiber links and system symbol rates. In complex DRNs, the EGN model can take the propagation history of all channels into account, and correctly assess different cases with variable link features. It provides a reliable reference for the development of real-time simpler approximate models.

Finally, an experiment was carried out for the first time by the OptCom group, aiming specifically at validating the EGN model. I collaborated in designing the experiment and

in assessing its results. It confirms the predictions of the EGN model, in a system setup where there is a significant difference between the GN and EGN model predictions. This provides a first experimental confirmation that the EGN model can reliably predict system performance, fully considering signal properties in the evaluation of the nonlinear interference.

In the future, I would like to work on several related topics:

- Explaining and correcting the residual inaccuracy of the EGN model SCI formulas in the first few spans;

- Finding out a closed-form formula for SCI correction to complete the EGN model asymptotic approximation;

- Deriving an analytical model for the phase noise, based on the EGN model, to investigate its impact on NLI in a wide range of system scenarios;

- Improving the numerical integration code for the full EGN model so that it can become an agile, fast and easy-to-use research tool;

- Investigating possible ways of optically or electronically mitigating NLI in future systems.

Appendix: List of acronyms

AGN	additive Gaussian noise
ASE	amplified spontaneous emission noise
BER	bit error-rate
CD	chromatic dispersion
CUT	channel-under-test
DAC	digital-to-analog converter
DM	dispersion management
DRN	Dynamically reconfigurable network
DSP	digital signal processing
EDFA	erbium-doped fiber amplifier
EGN model	enhanced Gaussian-noise model
XPM	the XPM model proposed in [30]
FDM	frequency division multiplexing
FEC	forward error-correcting code
FWM	four-wave mixing
GN model	Gaussian-noise model
GNRF	GN model reference formula
IMDD	intensity modulation direct detection
INT	interfering channel in a WDM comb (as opposed to the CUT)
ME	Manakov equation
MCI	multi-channel interference
NLC	non-linearity compensation
NLI	nonlinear interference
NLSE	nonlinear Schroedinger equation
NZDSF	non-zero dispersion-shifted fiber
OFDM	orthogonal frequency division multiplexing
OSNR	optical signal-to-noise ratio
PM	polarization-multiplexed

PSCF	pure-silica-core fiber
PSD	power spectral density
PTP	point-to-point links
QAM	quadrature amplitude modulation
QPSK	quadrature phase-shift keying
RV	random variable
Rx	receiver
SCI	self-channel interference
SMF	standard single-mode fiber
SNR	signal-to-noise ratio
SpS	spectral slicing
TD	time-domain
Tx	transmitter
UT	uncompensated transmission
VS	Volterra series
WDM	wavelength division multiplexing
XCI	cross-channel interference
XPM	cross phase modulation

References

1. M. Nakazawa, K. Kikuchi, and T. Miyazaki, "Coherent optical communications: historical perspectives and future directions", Chapter 2 in High Spectral Density Optical Communication Technologies, vol. 10, pp. 978-3, New York: Springer, 2010.

2. G. P. Agrawal, *Fiber-Optic Communications Systems*, 3rd ed. NewYork, NY, USA: Wiley, 2002.

3. C. R. Menyuk, "Nonlinear pulse propagation in birefringent optical fibers," *IEEE J. Quantum Electron.*, vol. 23, pp. 174-176, 1987.

4. D. Marcuse, C. R. Menyuk, and P. K. A. Wai, "Application of the Manakov-PMD equation to studies of signal propagation in optical fibers with randomly varying birefringence," *J. Lightw. Technol.,* vol. 15, no. 9, pp. 1735-1746,1997.

5. A. Splett, C. Kurzke, and K. Petermann, "Ultimate transmission capacity of amplified optical fiber communication systems taking into account fiber nonlinearities," in *Proc. of ECOC 1993*, vol. 2, pp. 41-44, 1993.

6. H. Louchet, A. Hodzic, and K. Petermann, "Analytical model for the performance evaluation of DWDM transmission systems," *IEEE Photon.Technol. Lett.,* vol. 15, no. 9, pp. 1219-1221, 2003.

7. E. E. Narimanov and P. P. Mitra, "The channel capacity of a fiber optics communication system: Perturbation theory," *J. Lightw. Technol.,* vol. 20, no. 3, pp. 530-537, 2002.

8. K. V. Peddanarappagari and M. Brandt-Pearce, "Volterra series transfer function of single-mode fibers," *J. Lightw. Technol.*, vol. 15, no. 12, pp. 2232-2241, 1997.

9. J. Tang, "The channel capacity of a multispan DWDM system employing dispersive nonlinear optical fibers and an ideal coherent optical receiver," *J. Lightw. Technol.*, vol. 20, no. 7, pp. 1095-1101, 2002.

10. J. Tang, "A comparison study of the shannon channel capacity of various nonlinear optical fibers," *J. Lightw. Technol.*, vol. 24, no. 5, pp. 2070-2075, 2006.

11. M. Nazarathy, J. Khurgin, R. Weidenfeld, Y. Meiman, P. Cho, R. Noe, I. Shpantzer,

and V. Karagodsky, "Phased-array cancellation of nonlinear FWM in coherent OFDM dispersive multi-span links," *Opt. Exp.*, vol. 16, pp. 15778-15810, 2008.

12. X. Chen and W. Shieh, "Closed-form expressions for nonlinear transmission performance of densely spaced coherent optical OFDM systems," *Opt. Exp.*, vol. 18, pp. 19039-19054, 2010.

13. W. Shieh and X. Chen, "Information spectral efficiency and launch power density limits due to fiber nonlinearity for coherent optical OFDM systems," *IEEE Photon. J.*, vol. 3, no. 2, pp. 158-173, Apr. 2011.

14. P. Poggiolini, A. Carena, V. Curri, G. Bosco, and F. Forghieri, "Analytical modeling of non-linear propagation in uncompensated optical transmission links," *IEEE Photon. Technol. Lett.*, vol. 23, no. 11, pp. 742-744, 2011.

15. A. Carena, V. Curri, G. Bosco, P. Poggiolini, and F. Forghieri, "Modeling of the impact of non-linear propagation effects in uncompensated optical coherent transmission links," *J. Lightw. Technol.*, vol. 30, no. 10, pp. 1524-1539, 2012.

16. P. Poggiolini, G. Bosco, A. Carena, V. Curri, Y. Jiang, and F. Forghieri, "A detailed analytical derivation of the GN model of non-linear interference in coherent optical transmission systems," posted on arXiv, www.arxiv.org, paper identifier 1209.0394. First posted 2012.

17. P. Poggiolini, "The GN model of non-linear propagation in uncompensated coherent optical systems," *J. Lightw. Technol.*, vol. 30, no. 24, pp. 3857-3879, 2012.

18. A. Bononi and P. Serena, "An alternative derivation of Johannisson's regular perturbation model," posted on arXiv, www.arxiv.org, paper identifier 1207.4729, 2012.

19. P. Johannisson and M. Karlsson, "Perturbation analysis of nonlinear propagation in a strongly dispersive optical communication system," *J. Lightw. Technol.,* vol. 31, no. 8, pp. 1273-1282, 2013.

20. A. Vannucci, P. Serena, and A. Bononi, "The RP method: A new tool for the iterative solution of the nonlinear Schrodinger equation," *J. Lightw. Technol.*, vol. 20, no. 7, pp. 1102-1112, 2002.

21. A. Mecozzi, C. B. Clausen, and M. Shtaif, "Analysis of intrachannel nonlinear

effects in highly dispersed optical pulse transmission," *IEEE Photon. Technol. Lett.*, vol. 12, no. 4, pp. 392-394, 2000.

22. A. Mecozzi, C. B. Clausen, andM. Shtaif, "System impact of intrachannel nonlinear effects in highly dispersed optical pulse transmission," *IEEE Photon. Technol. Lett.*, vol. 12, no. 12, pp. 1633-1635, 2000.

23. A. Mecozzi and R.-J. Essiambre, "Nonlinear Shannon limit in pseudolinear coherent systems," *J. Lightw. Technol.*, vol. 30, no. 12, pp. 2011-2024, 2012.

24. A. Bononi, P. Serena, N. Rossi, E. Grellier, and F. Vacondio, "Modeling nonlinearity in coherent transmissions with dominant intrachannel-four-wave-mixing," *Opt. Exp.*, vol. 20, pp. 7777-7791, 2012.

25. L. Beygi, E. Agrell, P. Johannisson, M. Karlsson, and H. Wymeersch, "A discrete-time model for uncompensated single-channel fiber-optical links," *IEEE Trans. Commun.*, vol. 60, no. 11, pp. 3440-3450, 2012.

26. M. Secondini and E. Forestieri, "Analytical fiber-optic channel model in the presence of cross-phase modulations," *IEEE Photon. Technol. Lett.*, vol. 24, no. 22, pp. 2016-2019, 2012.

27. M. Secondini and E. Forestieri, "On XPM mitigation in WDM fiber-optic systems," *IEEE Photon. Technol. Lett.*, vol. 26, no. 22, pp. 2252-2255, 2014.

28. A. Carena, G. Bosco, V. Curri, P. Poggiolini, and F. Forghieri, "Impact of the transmitted signal initial dispersion transient on the accuracy of the GN-model of non-linear propagation," in *Proc. of ECOC 2013*, London, 2013, paper Th.1.D.4.

29. P. Serena and A. Bononi, "On the accuracy of the Gaussian nonlinear model for dispersion-unmanaged coherent links," in *Proc. of ECOC 2013*, London, 2013, paper Th.1.D.3.

30. R. Dar, M. Feder, A. Mecozzi, and M. Shtaif, "Properties of nonlinear noise in long, dispersion-uncompensated fiber links," *Opt. Exp.*, vol. 21, pp. 25685-25699, 2013.

31. R. Dar, M. Feder, A. Mecozzi, and M. Shtaif, "Accumulation of nonlinear interference noise in multi-span fiber-optic systems," posted on arXiv, www.arxiv.org, paper identifier 1310.6137, 2013.

32. R. Dar, M. Feder, A. Mecozzi, and M. Shtaif, "Accumulation of nonlinear

interference noise in fiber-optic systems," *Opt. Exp.,* vol. 22, no. 12, pp. 14199-1421, 2014.

33. P. Serena, A. Bononi, and N. Rossi, "The impact of the modulation dependent nonlienar interference missed by the Gaussian noise model," in *Proc. of ECOC 2014*, Cannes, 2014, paper Mo.4.3.1.

34. A. Carena, G. Bosco, V. Curri, P. Poggiolini, M. T. Taiba, and F. Forghieri, "Statistical characterization of PM-QPSK signals after propagation in uncompensated fiber links," In *Proc. of ECOC 2010*, Torino, 2010, paper P4.07.

35. F. Vacondio, O. Rival, C. Simonneau, E. Grellier, A. Bononi, L. Lorcy, and S. Bigo, "On nonlinear distortions of highly dispersive optical coherent systems," *Opt. Exp.,* vol. 20, no. 2, pp. 1022-1032, 2012.

36. K. Inoue and H. Toba, "Fiber four-wave mixing in multi-amplifier systems with nonuniform chromatic dispersion," *J. Lightwave Technol.*, vol. 13, pp. 88-93, 1995.

37. W. Zeiler, F. Di Pasquale, P. Bayvel, and J.E. Midwinter, "Modeling of four-wave mixing and gain peaking in amplified WDM optical communication systems and networks," *J. Lightwave Technol.*, vol. 14, pp. 1933-1942, 1996.

38. P. Poggiolini, G. Bosco, A. Carena, V. Curri, Y. Jiang, and F. Forghieri, "The GN model of fiber non-linear propagation and its applications," *J. Lightw. Technol.,* vol. 32, pp. 694-721, 2014.

39. J. Pan, P. Isautier, M. Filer, S. Tibuleac and S. E. Ralph, "Gaussian noise model aided in-band crosstalk analysis in ROADM-enabled DWDM networks," in *Proc. of OFC 2014*, San Francisco, CA, 2014, paper Th1I.1.

40. S. J. Savory, "Approximations for the nonlinear self-channel interference of channels with rectangular spectra," *IEEE Photon. Technol. Lett.* vol. 25, pp. 961-964, 2013.

41. A. Bononi, O. Beucher, and P. Serena "Single- and cross-channel nonlinear interference in the Gaussian noise model with rectangular spectra," Opt. Exp., vol. 21, pp. 32254-32268, 2013.

42. P. Poggiolini, G. Bosco, A. Carena, V. Curri, Y. Jiang, and F. Forghieri, "A simple and effective closed-form GN-model correction formula accounting for signal non-Gaussian distribution," posted on arXiv, www.arxiv.org, paper identifier

1402.3528. First posted 2014.

43. S. J. Savory, "Optimum electronic dispersion compensation strategies for nonlinear transmission," *Elect. Lett.,* vol. 42, no. 7, pp. 407-408, 2006.

44. V. Curri, P. Poggiolini, A. Carena, and F. Forghieri, "Performance analysis of coherent 222-Gb/s NRZ PM-16QAM WDM systems over long-haul links," *IEEE Photon. Technol. Lett.*, vol. 22, no. 5, pp. 266-268, 2010.

45. M. S. Alfiad, D. van den Borne, S. L. Jansen, T. Wuth, M. Kuschnerov, G. Grosso, and H. de Waardt, "A comparison of electrical and optical dispersion compensation for 111-Gb/s POLMUX-RZ-DQPSK," *J. Lightw. Technol.*, vol. 27, no. 16, pp. 3590-3598, 2009.

46. X. Liu, S. Chandrasekhar, P. Winzer, R.W. Tkach, and A. R. Chraplyvy, "406.6-Gb/s PDM-BPSK superchannel transmission over 12,800-km TWRS fiber via nonlinear noise squeezing," in *Proc. of OFC 2013*, Anaheim, CA, 2013, paper PDP5B.10.

47. A. Ghazisaeidi, J. Renaudier, M. Salsi, P. Tran, G. Charlet, and S. Bigo, "System benefits of digital dispersion pre-compensation for non-dispersion-managed PDM-WDM transmission," in *Proc. of ECOC 2013*, London, 2013, paper We.4.D.4.

48. X. Liu and S. Chandrasekhar, "Experimental study of the impact of dispersion pre-compensation on PDM-QPSK and PDM-16QAM performance in inhomogeneous fiber transmission", in *Proc. of ECOC 2013*, London, 2013, paper P.4.17.

49. Q. Zhuge, B. Chatelain, and D. V. Plant, "Comparison of intra-channel nonlinearity tolerance between reduced-guard-interval CO-OFDM systems and nyquist single carrier systems,' in *Proc. of OFC 2012*, Los Angeles, CA, 2012, paper OTh1B.3.

50. M. Qiu, Q. Zhuge, X. Xu, M. Chagnon, M. Morsy-Osman, and David V. Plant, "Subcarrier multiplexing using DACs for fiber nonlinearity mitigation in coherent optical communication systems," in *Proc. of OFC 2014*, San Francisco, CA, 2014, paper Tu3J.2.

51. W. Shieh and Y. Tang, "Ultrahigh-speed signal transmission over nonlinear and dispersive fiber optic channel: the multicarrier advantage," *IEEE Photon. J.,* vol. 2, no. 3, pp. 276-283, 2010.

52. L. B. Du and A. J. Lowery, "Optimizing the subcarrier granularity of coherent

optical communications systems," *Opt. Exp.,* vol. 19, no. 9, pp. 8079, 2011.

53. P. Poggiolini, G. Bosco, A. Carena, V. Curri, V. Miot, and F. Forghieri, "Performance dependence on channel baud-rate of PM-QPSK systems over uncompensated links," *IEEE Photon. Technol. Lett.*, vol. 23, no. 1, pp. 15-17, 2011.

54. A. Bononi, N. Rossi and P. Serena, "Performance dependence on channel baud-rate of coherent single-carrierWDM systems," in *Proc. of ECOC 2013*, London, 2013, paper Th.1.D.5.